SIGNAL TRANSMISSION AND PROCESSING FOR MILLIMETER-WAVE AND TERAHERTZ COMMUNICATIONS

A Dissertation
Presented to
The Academic Faculty

By

Cen Lin

In Partial Fulfillment
of the Requirements for the Degree
Doctor of Philosophy
in
Electrical and Computer Engineering

School of Electrical and Computer Engineering
Georgia Institute of Technology
May 2017

SIGNAL TRANSMISSION AND PROCESSING FOR MILLIMETER-WAVE AND TERAHERTZ COMMUNICATIONS

Approved by:

Dr. Geoffrey Ye Li, Advisor
Professor, School of Electrical and Computer Engineering
Georgia Institute of Technology

Dr. Gee-Kung Chang
Professor, School of Electrical and Computer Engineering
Georgia Institute of Technology

Dr. Ian F. Akylidiz
Professor, School of Electrical and Computer Engineering
Georgia Institute of Technology

Dr. Yao Xie
Assistant Professor, School of Industrial and Systems Engineering
Georgia Institute of Technology

Dr. Mary Ann Weitnauer
Professor, School of Electrical and Computer Engineering
Georgia Institute of Technology

Date Approved: March 29, 2017

To my family, for their endless love, support and encouragement.

ACKNOWLEDGMENTS

There are a number of people I wish to thank for making my life at Georgia Institute of Technology rich and colorful. Without them, it would not be possible for me to accomplish this dissertation.

Foremost, I would like to express my deepest gratitude to my advisor, Dr. Geoffrey Ye Li, for his consistent guidance and support throughout my research and study. His knowledge, personality, and passion inspired and helped me overcome many difficulties. What I have learnt from him is a precious asset of my life.

I would like to thank Dr. Ian F. Akyildiz and Dr. Mary Ann Weitnauer for the constructive discussions and comments in the Terahertz project as well as my research. Also, I am honored to have Dr. Gee-Kung Chang and Dr. Yao Xie to serve in my dissertation committee. Their valuable suggestions benefited me a lot in refining this dissertation. Moreover, I am very grateful to Dr. Hua Wang for the insightful discussions on practical design of millimeter-wave and Terahertz circuits.

My thanks also goes to current and former lab members, Cong Xiong, Lu Lu, Daewon Lee, Le Liang, Guanding Yu, Rui Yin, Xu Bao, Yinshen Liu, Yunlong Cai, Daquan Feng, Chunlong He, Jian Yu, Wei Guo, Yinjun Liu, Xiaoyu Sun, and all others. Thank you for the help and discussions. I am also indebted to my friends, Kai Ying, Qianao Ju, Sen Yang, Longfeng Wang, and many others. Thank you for creating a beautiful and unforgettable memory for me in the past years.

I owe my deepest gratitude to my family, especially my parents. Their endless love, encouragement, and support are always the source of my courage and motivation. This dissertation is dedicated to them.

TABLE OF CONTENTS

LIST OF TABLES

LIST OF FIGURES

SUMMARY

The surging traffic and ever-growing services are defining a new generation of wireless communications, where the conflicts between the limited spectrum resources and the insatiable demands become more and more serious. To alleviate the spectrum scarcity, new higher frequency bands are explored, among which the millimeter-wave (mmWave) band, from 30 GHz to 300 GHz, and the Terahertz (THz) band, from 0.1 THz to 10 THz, stand out to be good candidates. These wide bands open a large frequency window to provide ultra-high data rates. In order to reap the mmWave and THz gain, novel systems with large-scale antennas should be designed to combat the severe path loss, which must respect the hardware challenges of mmWave and THz circuits.

The objective of the thesis is to provide a design guide on signal transmission and processing for mmWave and THz communications. Specifically, the higher-mmWave and THz bands, i.e., over 60 GHz, are investigated. First of all, a suitable system, from both communication and circuit levels, should be designed. Thus, we compare two system structures, the fully-connected structure and the array-of-subarrays structure, from system power consumption, spectral efficiency, and energy efficiency. The array-of-subarrays structure shows significant advantages over the fully-connected structure in both spectral and energy efficiency. Second, to accommodate the ultra-broad bandwidth in the mmWave and THz bands, we further study the beamforming training with time-delay components for the array-of-subarrays structure. In particular, two multi-resolution time-delay codebooks with subarray coordination and hybrid processing are proposed. Then, based on the codebooks, a hierarchical beamforming training strategy is developed to enable simultaneous training for multiple users. Third, we investigate the performance limits and optimized array design for single-user mmWave and THz communications with the array-of-subarrays structure. Based on the modified Saleh-Valenzuela (S-V) channel model, we analyze the ergodic capacity with hybrid beamforming for the system and obtain an upper bound. Last but not

least, we extend the study of the array-of-subarrays structure to wideband communications. To capture the distance-frequency dependent characteristics of the THz channels, we develop a hybrid beamforming scheme with distance-aware multi-carrier transmission, including analog beamforming for user grouping and interference cancellation and digital beamforming for antenna subarray selection and adaptive power allocation. Specifically, two greedy subarray selection algorithms are proposed. In summary, the proposed design in this thesis builds the physical-layer foundation for higher-mmWave and THz communications.

CHAPTER 1

INTRODUCTION

A new age of wireless communications is dawning, where data are consumed in a larger, faster, and denser way. It is predicted that data rates will reach Terabit-per-second (Tbps) within the next five years [1]. Unfortunately, current wireless systems fail to support these demands or to provide satisfactory quality-of-service (QoS) due to the scarcity of spectrum resources. As a result, new frequency bands and novel techniques are needed to deal with this spectrum gridlock. In view of the enormous bandwidth and availability with recent circuit development, communications over the millimeter-wave (mmWave) and Terahertz (THz) bands turn out to be a promising solution [2–12].

1.1 Background and Motivation

As shown in Fig. 1.1, the mmWave band, spanning from 30 GHz to 300 GHz, and the THz band, from 0.1 THz to 10 THz, offer bandwidth orders of magnitude greater than the lower-frequency bands. Specifically, the usable bandwidth of the mmWave and THz bands is at least several GHz while that of the sub-6 GHz bands is only on the order of MHz [11]. These large, safe, and unoccupied frequency resources will help to alleviate the capacity limitation of current wireless systems and provide rich soil to fertilize a plethora of ultra-broadband and ultra-high-speed applications, such as Terabit wireless personal/local area networks (WPANs/WLANs), mmWave or THz femtocells, and Terabit device-to-device (D2D) services.

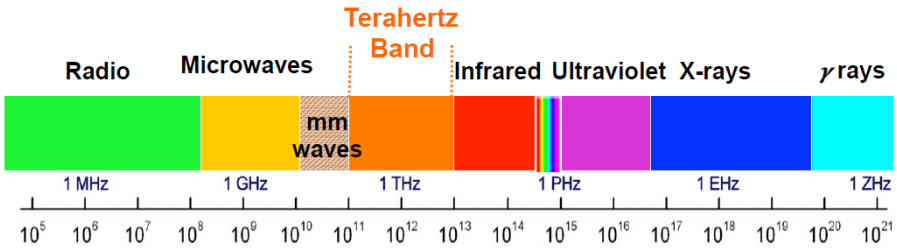

Fig. 1.1 The mmWave (30-300 GHz) and THz bands (0.1-10 THz).

Although mmWave and THz communications exhibit great potentials, many new challenges arise, such as link budget, energy efficiency, and adaptive transmission, requiring innovative solutions, where the well-established technologies may be ill-suited.

- *Link budget*: As the frequency increases, mmWave and THz signals experience much more severe path loss compared with their lower-frequency counterparts. Accordingly, mmWave and THz systems require judicious planning on wireless link budget. Thanks to the very short wavelength on a millimeter or sub-millimeter level, a large number of antennas can be tightly packed into a small form factor to combat the channel attenuation and reap the mmWave or THz gain. Therefore, appropriate design is expected for large-antenna systems to establish reliable mmWave or THz links while ensuring an optimum array performance.
- *Energy efficiency*: The complexity and cost of transceiver devices increase significantly with the frequency. Moreover, the generated signal power is indeed limited in the higher-mmWave and THz bands with regard to the large circuit power consumption. Thus, the circuit hardware puts a very stringent requirement on the energy efficiency of mmWave and THz systems, especially when a large number of antennas are used. Consequently, novel system architecture and communication strategies, which respect the nature of the mmWave and THz hardware, are imminently desired.
- *Adaptive transmission*: MmWave and THz systems are sensitive to the varying electromagnetic environments. For example, a blockage may greatly affect both the radio channel qualities and the antenna load impedances. Thus, all communication strategies should be adaptive to the changing environments. In particular, techniques, such as adaptive beamforming, channel tracking, and relay-assisted transmission, should be developed to ensure the connectivity and robustness of the system.

Given all these challenges, the major goal of this research is to offer an appropriate design guide on signal transmission and processing for mmWave and THz communications. Specifically, we focus on the higher-mmWave and THz bands, i.e., over 60 GHz. We aim

to provide a thorough analysis from system hardware to communications and establish a physical-layer foundation for mmWave and THz communications.

1.2 Literature Review

In this section, we will review current state-of-the-art study on mmWave and THz communications, including channel modeling, circuit design, and transmission strategies.

1.2.1 Millimeter-Wave and Terahertz Channels

The mmWave and THz channels have been studied in [4, 13, 14] and [15–19], respectively. There are some common and distinguished characteristics between the mmWave and THz channels, which will be briefly introduced in this subsection.

1.2.1.1 Basic Channel Property

The mmWave and THz channels generally consist of one line-of-sight (LOS) path and several non-LOS (NLOS) paths, resulting from reflection and scattering. Distinctively, extra atmospheric attenuation exists in addition to free-space attenuation, which mainly comes from the absorption by water vapor molecules for the THz band while the major absorption is from oxygen molecules for mmWave less than 100 GHz [4, 18]. In particular, the attenuation ranges from a few tens of dB/km to hundreds of dB/km and increases with the frequency [4, 7]. As a result, the path loss turns out to be much more severe. Moreover, due to the decrease of the wavelength, reflection and scattering losses through transmission path becomes much larger. Consequently, only up to second order reflections are considered in the higher-mmWave and THz bands [13, 15]. Therefore, the higher-mmWave and THz channels have fewer paths and are sparser in the angular domain. More pivotally, the gap between the LOS and NLOS path gain is more significant. In particular, compared with the LOS path, the power of the first-order reflected path is attenuated by 5-10 dB on average and the second-order reflection by more than 15 dB [13, 15, 19]. Accordingly, higher-mmWave and THz communications are LOS-dominant with NLOS-assisted, which means the transmit power should be mainly focused on the LOS path and a few strongest

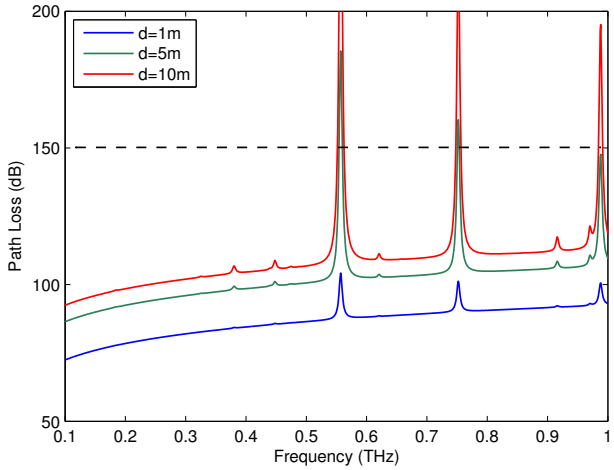

Fig. 1.2 LOS path loss in the mmWave and THz bands (0.1-1 THz) for different transmission distances.

NLOS paths. Since the reflection loss increases and the number of rays decreases, the delay spread drops to far less than 1 ns [16, 19], thus, the coherent bandwidth increases drastically, which can reach 1-5 GHz in the THz band [19]. Also, the overall angular spread becomes smaller. Specifically, up to 119° has been reported for indoor scenarios at 60 GHz (the mmWave band) [13] while only up to 40° angular spread has been observed for indoor environments in the THz band [20].

1.2.1.2 Distance-Frequency Dependent Characteristic

Different from mmWave, channels in the THz band highly depend on distance and frequency. More specifically, a change in the communication distance will not only result in a variation of the path loss but also of the available transmission bandwidth. Fig. 1.2 shows the LOS path loss between 0.1 THz and 1 THz for different distances [11]. In the figure, the path loss peaks, resulting from molecular absorption, create transmission windows. Each window has different bandwidth, which varies greatly with the communication distance. In particular, an increase in the communication distance leads to a shrink of the bandwidth. For example, considering 150 dB as a path loss threshold in Fig. 1.2, the available transmission window is the whole 0.1-1 THz for 1 m distance, whereas for 10 m distance the

usable bandwidth is fragmented into three pieces, namely, 0.1-0.54 THz, 0.56-0.74 THz, and 0.76-0.98 THz, and the total available bandwidth is also reduced.

1.2.2 Circuit and System Design

Recent advances in compact and efficient mmWave and THz devices are filling the so-called THz gap. Compact mmWave and THz transceivers have been developed for signal generation and detection based on electronics, e.g. Silicon-Germanium (SiGe) based heterojunction bipolar transistor (HBT), Gallium-Nitride (GaN) based monolithic millimeter-wave integrated circuit (MMIC), and Indium-Phosphide (InP) based high-electron-mobility transistors (HEMT) [11], or photonics, e.g. Quantum Cascade Laser (QCL) [8]. Both pulse-based and continuous-wave signals can be transmitted though the signal power is limited [9]. Also, mixed signal components, such as high-speed digital-to-analog converters (DAC) and analog-to-digital converters (ADC), have been designed [9,21,22]. Meanwhile, voltage- or magnet-controlled mmWave and THz phase shifters based on liquid crystal or graphene transmission lines have been developed at room temperature [23–25], which are crucial to beamforming and adaptive transmission. In addition, new graphene technology has been investigated to improve the antenna performance in the THz band [11,26].

Although these hardware components present good capabilities in circuit design, their high complexity and power cost impose more constraints on large-antenna systems, precluding the design used in lower frequencies. Thus, conventional systems with one dedicated radio frequency (RF) chain for one antenna are no longer feasible. Instead, systems with only a limited number of RF chains are preferred, and hybrid digital-analog architecture has been developed [12,27–29]. The hybrid structure split signal processing into digital and analog parts, thus, the overall circuit complexity and power consumption would be reduced. Apart from high-complexity hardware, the ultra-broad bandwidth of the mmWave and THz bands also has a great impact on both system design. In specific, conventional circuit components, such as pure phase shifters used for analog processing in RF domain, will face many new challenges. For one thing, the phase shifters will be not accurate enough

for signals with wide bandwidth since the shifted phase designed for one specific frequency may vary significantly for another frequency. For another, constant phase shifts across a wide range of frequencies will lead to beam squint [12, 30, 31], i.e., variable beam directions with frequencies, which will significantly degrade system performance. To overcome these deficiencies, controllable time-delay lines [23, 32], i.e., time-delay phase shifters, are adopted in circuit design [12, 33], for which the shifted phase will vary with frequencies based on the signal traveling time. In particular, true time delays (TTD) can be implemented by either electronics [32, 33] or photonics [34] in the mmWave and sub-THz bands, and the associated power consumption, 20-80 mW for different time-resolutions [35, 36], is comparable to pure phase shifters. More importantly, recent advances on TTD have greatly reduced the circuit size and improved the accuracy [35, 36], which facilitates the practical implementation. As a result, all these new circuit and system features distinguish the communications over the higher-mmWave and THz bands, requiring adjustment on the associated transmission design.

1.2.3 Transmission and Beamforming Strategies

As mentioned in Section 2.2, hybrid architecture is used in mmWave and THz communication systems. Extensive studied has been made in transmission and beamforming design for the hybrid architecture, which can be summarized into two categories, i.e., analog beamforming and hybrid beamforming.

1.2.3.1 Analog Beaforming

When only one RF chain is equipped, the hybrid architecture converges to a phased array. Then, signal processing is mainly accomplished in analog domain with phase shifters, which is called analog beamforming. Specifically, analog beamforming has been adopted in several commercial mmWave communication standards, e.g., IEEE 802.11ad [37] and IEEE 802.15.3c [38], and many beamforming algorithms have been proposed [39–42]. Different multi-resolution codebooks has been designed for mmWave beam scanning and

tracking in [39], [40], and [41]. In [42], directional learning and beamforming with broadened beams has been developed. Though analog beamforming could greatly reduce the circuit complexity, only one data stream can be supported due to the limitation of one RF chain. Thus, the multiplexing gain and multi-stream capability will be lost.

1.2.3.2 Hybrid Beamforming

As a performance-and-complexity tradeoff, hybrid digital-analog architecture with multiple RF chains is often considered. In particular, two different structures in RF domain, the fully-connected structure [43–47] and the array-of-subarrays structure [48–57], have been designed. Then, different beamforming strategies have been developed based on these two structures for lower-mmWave communications while the design for THz communications is absent.

For the fully-connected structure, a hybrid beamforming method with orthogonal matching pursuit (OMP) has been proposed in [43] for the single-user situation, and a two-stage hybrid beamforming scheme has been designed in [46] for multiuser situations. Also, an alternating optimization method has been developed in [45] for hybrid beamforming design. Although these hybrid beamforming strategies exhibit good performance, most of them require perfect channel state information (CSI) of the entire antenna array and have high complexity. Due to the severe path loss in the mmWave band, the explicit CSI of the large antenna array is hard to obtain and the overhead is extremely high. To deal with this issue, compressive-sensing based estimation has been introduced [58, 59]. A multi-resolution codebook and a channel estimation algorithm through sparse channel recovery have been proposed in [44], however, a prior knowledge of the number of the channel path is still needed. Moreover, sparse channel estimation has been investigated in [47] based on compressing sensing and subspace methods. However, the training signals for compressive sensing may be corrupted in noise due to significant power dissipation over mmWave channels, which may reduce the effectiveness of channel measurement. As a result, the number of measurements as well as the training overhead will be increased.

On the other hand, for the array-of-subarrays structure, LOS multiple-input-multiple-output (MIMO) communications with multiple subarrays have been investigated in [48] to exploit the spatial degrees of freedom. Different iterative beamforming algorithms have been developed in [49] and [50] for single-user and multiuser communications, respectively. Robust hybrid beamforming design has been investigated in [51]. For beamforming training and channel estimation, codebook-based beamforming searching and angle-of-arrival (AoA) estimation have been studied in [52]. Also, differential beam tracking (DBT) and differential beam search (DBS) have been proposed for angle-of-departure (AoD) and AoA estimation in both time and frequency domain by exploiting the phase difference between adjacent subarrays [53, 54]. A low-complexity subset RF beam searching method has been designed in [56]. Furthermore, system energy efficiency of the array-of-subarrays structure has been analyzed in [57] using a general power consumption model. In general, the array-of-subarrays structure have less complexity and fewer requirements on channel information, which would be easier for practical implementation [60]. However, there are still many open problems for the array-of-subarrays structure, such as subarray cooperation and joint beamforming design.

1.3 Research Objectives and Main Contributions

According to the literature survey, related research on higher-mmWave and THz communication design is still missing. Therefore, it is interesting to investigate the communications over the higher-mmWave and THz bands and design appropriate transmission strategies to capture the distinguished characteristics.

As the first step, a suitable system, well-developed from both communications and circuits, should be designed. Therefore, in Chapter 2, we investigate two different types of architecture, the fully-connected structure and the array-of-subarrays structure, for indoor multiuser mmWave and THz systems [61, 62]. By adopting the Doherty PA to improve

the PA efficiency of the system, we develop nonlinear system power consumption models for the two structures, which take into account the insertion loss brought by circuit components. In particular, the total power consumption of the array-of-subarrays structure is shown to be less than that of the fully-connected structure. Moreover, we propose different low-complexity hybrid beamforming schemes for the two structures. Specifically, beamsteering-codebook searching algorithms are developed in RF domain for analog beamforming and zero-forcing digital beamformers are designed at baseband for interference cancellation among different users. Then, we compare the achievable rates with the hybrid beamforming for the two structures and show that, with the insertion loss, the achievable rate of the array-of-subarrays structure is generally larger than that of the fully-connected structure. In addition, we investigate the energy efficiency of the system for both structures and propose the optimal power control strategies, which offer energy-efficient design to accommodate different channel conditions. As the array-of-subarrays structure has a larger sum-rate and less power consumption, the associated energy efficiency outperforms that of the fully-connected structure. Simulation results are provided to compare and validate the performance of the two structures, where the array-of-subarrays structure shows a great advantage over the fully-connected structure in both spectral efficiency and energy efficiency.

In Chapter 3, we study the beamforming training for the array-of-subarrays structure, where the impact of time-delay components are considered [63, 64]. By capturing the nature of the time-delay phase shifters, we define the time-delay codebook structure for the system. Then, we propose two multi-resolution time-delay codebooks with subarray coordination and hybrid processing. In particular, one codebook is obtained through physical beam adaptation among different subarrays, and the other is achieved by dynamic approximation of the expected beam pattern. Moreover, we present a low-complexity system implementation to simplify circuit design of large-dimension time-delay lines. Then,

the two time-delay codebooks are modified to accommodate the architecture of the low-complexity system. In addition, we develop a hierarchical beamforming training strategy with the multi-resolution time-delay codebooks, which enables simultaneous searching for multiple users to obtain the optimal individual beam pairs. Specifically, a threshold for received signal power is introduced to reduce the number of scanned codewords as well as the training overhead. Simulation results show that the proposed multi-resolution time-delay codebooks could provide sufficient beam gains and are robust over large bandwidth. And, the effectiveness of the hierarchical beamforming training is also verified.

In Chapter 4, we further investigate the performance limits and optimized array design for single-user indoor mmWave and THz communications with the array-of-subarrays structure [65, 66]. First, we modify the Saleh-Valenzuela (S-V) model to capture the characteristics of the mmWave and THz channels. Then, we analyze the ergodic capacity with hybrid beamforming for the system and obtain a capacity upper bound. Second, we investigate the effects of uncertainties in the phase shifters and analyze the corresponding capacity degradation. Taking the uncertainties into account, we provide a guideline on designing the antenna subarray size and number to ensure certain data rates at different communication distances. Finally, numerical results are provided to show that the mmWave and THz system can support Tbps communications at different distances. Moreover, the capacity degradation due to the phase uncertainties generally increases with the subarray size and finally approaches a limit. In particular, to make full use of the antenna gains and reduce the performance degradation due to phase uncertainties, the subarray size should not be too small.

We extend the study of the array-of-subarrays structure to wideband communications in Chapter 5 [67, 68]. By exploiting the distance-frequency dependent characteristics in the THz band, we develop a distance-aware multi-carrier transmission policy and design an associated hybrid beamforming scheme. Specifically, a two-step beamsteering searching and user grouping method is developed in analog domain, where users in different groups could

share the same THz frequency resources without interference while users in the same group are assigned orthogonal frequencies based on the distance-aware multi-carrier scheme. In digital domain, antenna subarrays are selected for each user group and data streams of a user group are routed to specific subarrays only rather than the entire antennas, which could reduce the cost of RF circuits. Furthermore, we develop an adaptive power allocation and antenna subarray selection policy to meet different needs of users at different distances. This adaptive beamforming problem is formulated as a QoS-aware active antenna subarray number minimization problem, which is solved as a mixed integer optimization problem. Specifically, a utility-based and a group-based greedy algorithms are proposed for the antenna subarray selection, which could be implemented in low complexity with guaranteed performance. Simulation results show the effectiveness of the proposed adaptive hybrid beamforming. In particular, the adaptive beamforming strategy outperforms non-adaptive and non-distance-aware schemes by providing antenna and beamforming gains. Moreover, the proposed antenna subarray selection algorithms can obtain near-optimal performance with significantly reduced complexity.

1.4 Organization of the Thesis

The rest of the thesis is organized as follows. In Chapter 2, spectral- and energy-efficient system design are provided. Then, subarray-based coordinated beamforming training is proposed in Chapter 3. Single-user transmission design and distance-aware multiuser wideband communications are developed in Chapter 4 and Chapter 5, respectively. Finally, conclusions of the thesis are given in Chapter 6.

CHAPTER 2

SPECTRAL- AND ENERGY-EFFICIENT SYSTEM DESIGN

To enable mmWave and THz communications, a suitable system, respecting the nature of mmWave and THz channels and circuit hardware, should be designed. In this chapter, we will compare two typical architecture for mmWave and THz systems in system power consumption, spectral efficiency, and energy efficiency. In particular, low-complexity hybrid beamforming schemes and optimal power control strategies will be proposed for both structures. Then, a preferred architecture will be determined for practical mmWave and THz system design.

The rest of this chapter is organized as follows. Section 2.1 presents a multiuser indoor mmWave and THz communication system with two different structures and introduces the associated channel and power consumption models for the system. Low-complexity hybrid beamforming schemes with interference cancellation are proposed for both structures in Section 2.2. In Section 2.3, we study and compare the energy-efficient design of different structures. Simulation results are provided in Section 2.4 to compare the spectral and energy efficiency of the two structures. Finally, we conclude the chapter in Section 2.5.

2.1 System Description

In this section, we will introduce the system model, the channel model, and the power consumption model for indoor mmWave and THz communications.

2.1.1 System Model

We consider an indoor communication system, where an access point (AP) serves J users at different distances, each transmitting an individual stream, using the mmWave or THz band. The AP is equipped with $K \times N$ tightly-packed antennas but with only K RF chains. As shown in Fig. 2.1, antennas can be connected to RF chains in two typical ways, namely, the fully-connected structure and the array-of-subarrays structure. For the fully-connected

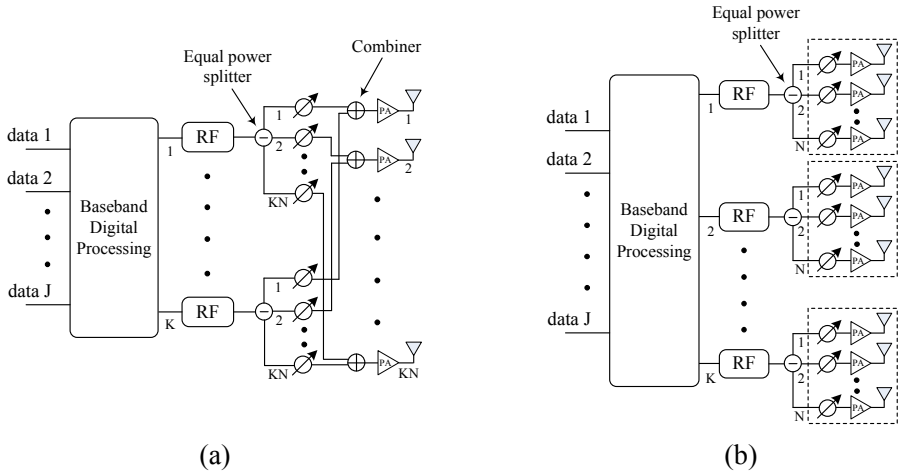

Fig. 2.1 Two hybrid structures for indoor mmWave and THz systems: (a) fully-connected structure; (b) array-of-subarrays structure.

structure in Fig. 2.1(a), an RF chain is connected to all antennas through an individual group of phase shifters. In contrast, for the array-of-subarrays structure in Fig. 2.1(b), an RF chain uniquely drives a disjoint subset of antennas, each of which is attached to an exclusive phase shifter. Accordingly, antennas are shared among different RF chains in transmission for the fully-connected structure while an antenna subarray is only accessed to one RF chain for the array-of-subarrays structure. At baseband, a digital processing module is adopted for both structures to control the data streams and manage interference among users. At the user side, due to the limitation of hardware and associated processing capability, only one RF chain is equipped with M tightly-packed antennas and phase shifters.

In particular, for the fully-connected structure, one RF chain should have the capability to single-handedly drive the entire large-scale antenna array, which is power-aggressive considering the limited power generated by higher-mmWave and THz sources and could also result in high loss. Besides, the use of a large number of phase shifters and combiners will in turn exacerbate the power cost of the circuits. However, for the array-of-subarrays structure, the basic component becomes a subarray rather than an antenna. All signal processing is carried out at a subarray level using an adequate number of antennas. With the disjoint structure and fewer phase shifters, the system complexity and power consumption

as well as the signal power loss will be greatly reduced. In addition, by cooperating with the digital baseband, signal energy can be effectively distributed among different subarrays and multiplexing capability can be provided. As a result, beamsteering gain, multiplexing gain, and spatial diversity gain can be jointly exploited.

To offer sufficient gains to all users for the system in Fig. 2.1, we assume that the number of RF chains is greater than or equal to the number of users, i.e. $K \geq J$, and the number of antennas at the user side is much smaller than that at the AP, i.e., $M \ll KN$. In order to keep consistency between the two structures, the subarray spacing is designed to be the same as the antenna spacing, r, here. In addition, we denote the user set as $\mathcal{J}$ and the set of RF chains as $\mathcal{K}$. And, the distance between user j and the AP is denoted as d_j, where $d_1 \geq d_2 \geq \cdots \geq d_J$. Therefore, the received signal of user j can be expressed as

$$y_j = \mathbf{v}_j^* \mathbf{H}_j \mathbf{W} \mathbf{F} \mathbf{s} + \mathbf{v}_j^* \mathbf{n}_j, \quad \forall j \in \mathcal{J}, \tag{2.1}$$

where $\mathbf{s} = [s_1, s_2, ..., s_J]^T$ is a $J \times 1$ vector containing the transmitted symbols of J users such that $\mathbb{E}[\mathbf{s}\mathbf{s}^*] = \frac{P_s}{J}\mathbf{I}_J$, in which P_s denotes the total initial transmit power. Note that equal power allocation is assumed here to ensure the fairness among the users. In (2.1), $\mathbf{H}_j$ is the $M \times KN$ mmWave or THz channel matrix between the AP and user j. $\mathbf{W}$ is the $KN \times K$ transmit analog beamforming matrix implemented by the equal power splitters and phase shifters. Accordingly, for the fully-connected structure,

$$\mathbf{W} = [\mathbf{w}_1, \mathbf{w}_2, \ldots, \mathbf{w}_K], \tag{2.2}$$

where $\mathbf{w}_k$ is a $KN \times 1$ vector with $\left|\mathbf{w}_k[i]\right| = \frac{1}{\sqrt{KN}}$, $i = 1, ..., KN$. For the array-of-subarrays structure, $\mathbf{W}$ is block diagonal and can be expressed as

$$\mathbf{W} = \begin{bmatrix} \mathbf{w}_1 & \mathbf{0} & \cdots & \mathbf{0} \\ \mathbf{0} & \mathbf{w}_2 & \cdots & \mathbf{0} \\ \vdots & \vdots & \vdots & \vdots \\ \mathbf{0} & \mathbf{0} & \cdots & \mathbf{w}_K \end{bmatrix}, \tag{2.3}$$

where $\mathbf{w}_k$ is an $N \times 1$ vector with $\left|\mathbf{w}_k[i]\right| = \frac{1}{\sqrt{N}},\ i = 1, ..., N$. $\mathbf{F}$ is the $K \times J$ baseband digital beamforming matrix for interference cancellation, where

$$\mathbf{F} = [\mathbf{f}_1, \mathbf{f}_2, ..., \mathbf{f}_J] = [\tilde{\mathbf{f}}_1, \tilde{\mathbf{f}}_2, ..., \tilde{\mathbf{f}}_K]^T, \tag{2.4}$$

with $\|\mathbf{W}\mathbf{f}_j\|^2 = 1,\ \forall j \in \mathcal{J}$. $\mathbf{v}_j$ is the $M \times 1$ receive analog beamforming vector performed at user j with $\left|\mathbf{v}_j[i]\right| = \frac{1}{\sqrt{M}},\ i = 1, ..., M$. And, $\mathbf{n}_j$ is the Gaussian noise presented at user j, i.e., $\mathbf{n}_j \sim \mathcal{N}(\mathbf{0}, \sigma_j^2\mathbf{I})$.

2.1.2 Channel Model

As mentioned in Chapter 1, for the mmWave and THz channels, the arrival paths generally consist of an LOS ray and several NLOS rays. Hence, the channel matrix for the system in Fig. 2.1 is given by [69]

$$\begin{aligned}\mathbf{H}(f,d) &= \mathbf{H}^{LOS}(f,d) + \mathbf{H}^{NLOS}(f,d) \\ &= \alpha_L(f,d)G_tG_r\mathbf{a}_r(M,\theta_L)\mathbf{a}_t^*(KN,\phi_L) \\ &\quad + \sum_{i=1}^{n_{NL}} \alpha_i(f,d)G_tG_r\mathbf{a}_r(M,\theta_i)\mathbf{a}_t^*(KN,\phi_i),\end{aligned} \tag{2.5}$$

where n_{NL} is the number of the NLOS rays. $\alpha(f,d)$ denotes the complex gain of the ray component, where f is the carrier frequency. And, ϕ and θ are the associated AoD and AoA for the rays, respectively. G_t and G_r are the transmit and receive antenna gains while vectors $\mathbf{a}_t(N,\phi)$ and $\mathbf{a}_r(N,\theta)$ represent the array steering vectors for an N-element array at the transmit and receive sides, respectively. It should be noted that the channel between the AP and user j, $\mathbf{H}_j$, has the same ray-tracing structure as $\mathbf{H}$ in (2.5) with different path gains and AoD/AoA for different users.

2.1.2.1 Path Gain

In the mmWave and THz bands, the atmospheric absorption loss is no longer negligible. Thus, the LOS path gain is composed of the spreading loss, L_{spread}, and the molecular absorption loss, L_{abs}, as [18]

$$|\alpha_L(f,d)|^2 = L_{spread}(f,d)L_{abs}(f,d) \triangleq L_{PL}(f,d), \tag{2.6}$$

where

$$L_{spread}(f,d) = \left(\frac{c}{4\pi f d}\right)^2, \tag{2.7}$$

and

$$L_{abs}(f,d) = e^{-k_{abs}(f)d}. \tag{2.8}$$

In (2.7) and (2.8), c stands for the speed of light in free space, and k_{abs} is the frequency-dependent medium absorption coefficient, which is determined by the composition of the transmission medium at a molecular level.

To account for the losses of the NLOS rays, the reflection coefficient, ϵ, should be considered, which is the product of the Fresnel reflection coefficient, υ, and Rayleigh roughness factor, ϱ, i.e., [19, 70]

$$\epsilon(f) = \upsilon(f)\varrho(f), \tag{2.9}$$

where

$$\upsilon(f) = \frac{\cos\varphi_{in} - \sqrt{n_r^2(f) - \sin^2\varphi_{in}}}{\cos\varphi_{in} + \sqrt{n_r^2(f) - \sin^2\varphi_{in}}}, \tag{2.10}$$

and

$$\varrho(f) = e^{-\frac{1}{2}\left(\frac{4\pi f \delta \cos\varphi_{in}}{c}\right)^2}, \tag{2.11}$$

in which δ is the standard deviation of the surface characterizing the material roughness, and φ_{in} is the angle of incidence and reflection. $n_r(f) = \frac{Z_0}{Z(f)}$ denotes the refractive index, where Z is the frequency-dependent wave impedance of the reflecting material and $Z_0 = 377\ \Omega$ is the free space wave impedance. Therefore, the NLOS path gain of the i-th ray with one reflection is given by

$$|\alpha_i(f,d)|^2 = \epsilon_i^2(f) L_{spread}(f,d) L_{abs}(f,d), \tag{2.12}$$

Due to the high reflection loss, only up to second order reflections are considered for higher-mmWave and THz frequencies [13, 15], where the associated path gain can be obtained similarly as in (2.12) with two reflection coefficients. Note that diffuse scattering and diffraction are neglected since they have insignificant contributions to the higher-mmWave and sub-THz channels [17].

As a result, the higher-mmWave and THz channels have limited paths. Moreover, the gap between the LOS and NLOS path gains is significant. Specifically, compared to the LOS path, the power of the first-order reflected path is attenuated by 5-10 dB on average and the second order reflection by at least 15 dB [4, 13, 15].

2.1.2.2 Angles of Departure and Arrival

The AoD and AoA for the mmWave and sub-THz channels, ϕ_i and θ_i, generally follow Laplacian distributions or modified Laplacian distributions [43, 71], where the angular ranges are limited to $[0, 2\pi)$. In addition, the angular spread at these frequency bands is smaller than that of microwave as a result of the increase in reflection and scattering loss [13, 15]. Specifically, up to 40° angular spread has been observed for indoor environments in [15, 20].

2.1.2.3 Array Steering Vector

For an N-element *uniform linear array* (ULA) in the y-axis, the array steering vector is [72, 73]

$$\mathbf{a}_{ULA}(N, \phi) = \left[1, ..., e^{j\frac{2\pi r}{\lambda_c} n \sin\phi}, ..., e^{j\frac{2\pi r}{\lambda_c}(N-1)\sin\phi}\right]^T, \tag{2.13}$$

where n is the antenna element index with $0 \leq n \leq N-1$, r is the antenna element spacing, and λ_c is the carrier wavelength. For an (M, N)-element *uniform planar array* (UPA) in the xy-plane, the array steering vector is [72–74]

$$\mathbf{a}_{UPA}(M, N, \phi, \vartheta) = \left[1, ..., e^{j\frac{2\pi r}{\lambda_c}[m\cos\phi\sin\vartheta + n\sin\phi\sin\vartheta]}, ..., e^{j\frac{2\pi r}{\lambda_c}[(M-1)\cos\phi\sin\vartheta + (N-1)\sin\phi\sin\vartheta]}\right]^T, \tag{2.14}$$

where m and n are the antenna element indexes with $0 \leq m \leq M-1, 0 \leq n \leq N-1$.

2.1.3 System Power Consumption Model

The power consumption of the system in Fig. 2.1 consists of the power costs of all the amplifiers and other circuit blocks. In this subsection, we will describe the power consumption models for the two different structures. It is worth mentioning that, regarding the large power cost required to establish reliable links under severe mmWave or THz channel conditions and the simpler circuit structure with only one RF chain at the user side, only the power consumption of the AP is considered in this paper.

2.1.3.1 Circuit Power

As shown in Fig. 2.1, the basic circuit is generally made up of the baseband, the RF chains, and the phase shifters. Specifically, an RF chain is composed of a DAC, a mixer, a local oscillator (LO), and an active filter. For the fully-connected structure, K RF chains and K^2N phase shifters are used with several KN-way splitters and K-way combiners. Since the splitter and the combiner are passive components with no power cost [75], the circuit power consumption can be expressed as

$$P_c^a = P_{BB} + KP_{RF} + K^2NP_{PS}, \tag{2.15}$$

where P_{BB}, P_{RF}, and P_{PS} are the power costs of the baseband, the RF chain, and the phase shifter, respectively. For the array-of-subarrays structure, only K RF chains and KN phase shifters are used with a few N-way splitters. Then, the circuit power consumption is given by

$$P_c^b = P_{BB} + KP_{RF} + KNP_{PS}. \tag{2.16}$$

2.1.3.2 Power Amplifier

As power amplifier is often the major power-consuming part of wireless systems, it plays an important role in circuit and system design. In the mmWave and THz bands, conventional complementary metal oxide semiconductor (CMOS) power amplifiers suffer from low PA efficiency, which can be as low as 10% [21]. To overcome this deficiency, new

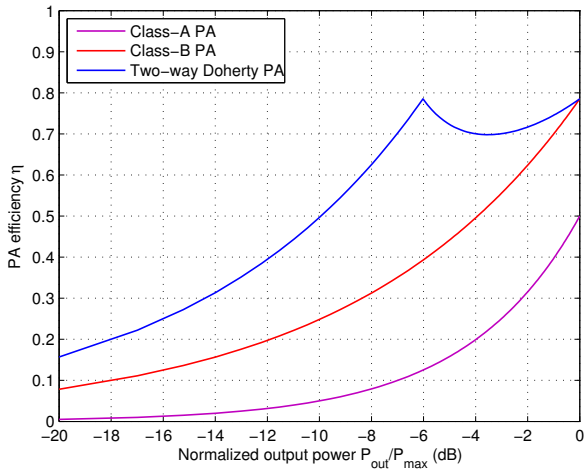

Fig. 2.2 The efficiency of different types of PA.

types of power amplifiers, e.g., Doherty power amplifier [76], are developed for these high-frequency bands. Different from conventional design of lower-frequency systems, where only fixed PA efficiency is accounted, the efficiency of these PAs, η, is generally a function of the output power as

$$\eta = \frac{P_{out}}{P_{PA}} = g\Big(\sqrt{\frac{P_{out}}{P_{max}}}\Big), \tag{2.17}$$

where P_{out} is the output power, P_{PA} is the PA power consumption, P_{max} denotes the maximum PA output power, and $g(\cdot)$ is the function indicating the relation between the output power and the PA efficiency. Notably, the nonlinear PA efficiency model is more accurate to capture the dynamics of PA in the mmWave and THz bands, especially when the output power is small and the PA efficiency is low. In particular, the efficiency of ideal Class-A, Class-B, and Doherty PA is plotted in Fig. 2.2, which can be analytically expressed as [76, 77]

$$\eta = \begin{cases} \ell\eta_{max}\sqrt{\frac{P_{out}}{P_{max}}}, & 0 < P_{out} \leq \frac{1}{\ell^2}P_{max}, \\ \ell\eta_{max}\frac{\frac{P_{out}}{P_{max}}}{(\ell+1)\sqrt{\frac{P_{out}}{P_{max}}}-1}, & \frac{1}{\ell^2}P_{max} < P_{out} \leq P_{max}. \end{cases} \tag{2.18}$$

where η_{max} is the peak PA efficiency and ℓ indicates the number of the combined amplifiers. Specifically, for Class-A PA, $\ell = 1$ and $\eta_{max} = \frac{1}{2}$. For Class-B PA, $\ell = 1$ and $\eta_{max} = \frac{\pi}{4}$. For ℓ-way symmetric Doherty PA with both amplifiers operating in Class-B mode, $\eta_{max} = \frac{\pi}{4}$.

As shown in Fig. 2.2, the peak efficiency of Class-A and Class-B PAs, 50% and 78%, is achieved at the peak output power while it drops rapidly as the output power decreases. However, the Doherty PA efficiency keeps above 70% when the normalized output power is larger than -6 dB and drops as Class-B PA when the power is less than -6 dB. Though Doherty PA has the same peak efficiency as Class-B PA, it has a deeper back-off region and better average efficiency than Class-A and Class-B PA. Moreover, the Doherty PA can provide about 40% efficiency on average, and current state-of-the-art design has demonstrated its effective operating frequency can reach 90-100 GHz [78]. In view of the advantages, we adopt the typical two-way Doherty PA for the mmWave and THz system. Thus, the PA power consumption is given by

$$P_{PA} = \begin{cases} \frac{2}{\pi}\sqrt{P_{out}P_{max}}, & 0 < P_{out} \leq 0.25P_{max}, \\ \frac{6}{\pi}\sqrt{P_{out}P_{max}} - \frac{2}{\pi}P_{max}, & 0.25P_{max} < P_{out} \leq P_{max}. \end{cases} \tag{2.19}$$

It is noteworthy that, although we consider the Doherty PA here, which is commonly used for current mmWave circuit design, our analysis can be easily applied to the systems using any PAs with the nonlinear-efficiency property as in (2.18).

Unlike digital processing in baseband, analog signal processing in the RF domain will introduce additional insertion power loss through the signal path due to the imperfectness of circuit components. For the system in Fig. 2.1, we focus on the specific power losses of the phase shifters, the splitters, and the combiners, whereas other power losses are assumed to be the same for the two structures and neglected in the analysis. Particularly, the insertion loss, resulting from the phase shifter in the mmWave and THz bands, is at least 3 dB and can be as large as 15 dB [75], while the insertion losses of the splitter and combiner are dependent on the types of the components. The more signals are divided or combined, the more severe the insertion loss is [75]. Specifically, if the Wilkinson power splitter/combiner is used, the insertion losses of the splitter for the fully-connected structure, L_{SP}^{a}, and for the

array-of-subarrays structure, L_{SP}^{b}, are given by [79, 80]

$$L_{SP}^{a} = 10\log_{10} KN, \tag{2.20}$$

$$L_{SP}^{b} = 10\log_{10} N, \tag{2.21}$$

whereas the additional insertion loss of the combiner, L_{CB}^{a}, for the fully-connected structure is

$$L_{CB}^{a} = 10\log_{10} K, \tag{2.22}$$

which results from the non-coherent combining of unbalanced signals. From (2.20), (2.22), and (2.21), we know that, compared with the array-of-subarrays structure, the fully-connected structure experiences more severe insertion loss, especially when large-scale antennas are deployed. That is the price for driving and combining analog signals throughout the entire array. Consequently, for the fully-connected structure, the effective transmit power, P_t^a, can be calculated as

$$P_t^a = P_s - L_{SP}^{a} - L_{PS} - L_{CB}^{a} + G_{PA}, \tag{2.23}$$

where L_{PS} is the associated insertion loss of the phase shifters. G_{PA} denotes the power gain of the PA. For the array-of-subarrays structure, no combiners are used. Thus, the effective transmit power, P_t^b, can be calculated as

$$P_t^b = P_s - L_{SP}^{b} - L_{PS} + G_{PA}. \tag{2.24}$$

For the fully-connected structure in Fig. 2.1, the output signal of each PA comes from all RF chains through equal power splitters. As a result of non-coherent power combining, all PAs have the same power consumption, which can be calculated by replacing the output power in (2.19) with the effective transmit power, P_t^a, in (2.23) as

$$P_{PA}^{a} = \begin{cases} \frac{2}{\pi}\sqrt{\frac{P_t^a}{KN}P_{max}}, & 0 < \frac{P_t^a}{KN} \le 0.25P_{max}, \\ \frac{6}{\pi}\sqrt{\frac{P_t^a}{KN}P_{max}} - \frac{2}{\pi}P_{max}, & 0.25P_{max} < \frac{P_t^a}{KN} \le P_{max}. \end{cases} \tag{2.25}$$

However, for the array-of-subarrays structure, the output signal of one PA is exclusively from its associated RF chain. That is to say, PAs connected to different RF chains have different power consumption. Thus, the power cost of the PA driven by the k-th RF chain is calculated as

$$P_{PA}^{b}(k) = \begin{cases} \frac{2}{\pi}\sqrt{\frac{P_t^b\|\tilde{\mathbf{f}}_k\|^2}{JN}P_{max}}, & 0 < \frac{P_t^b\|\tilde{\mathbf{f}}_k\|^2}{JN} \leq 0.25P_{max}, \\ \frac{6}{\pi}\sqrt{\frac{P_t^b\|\tilde{\mathbf{f}}_k\|^2}{JN}P_{max}} - \frac{2}{\pi}P_{max}, & 0.25P_{max} < \frac{P_t^b\|\tilde{\mathbf{f}}_k\|^2}{JN} \leq P_{max}, \end{cases} \tag{2.26}$$

where $\tilde{\mathbf{f}}_k$ is the k-th row of $\mathbf{F}$ defined in (2.4). Note that, the effective transmit power is divided by KN in (2.25) or by N in (2.26), which is the result of equal power split.

2.1.3.3 Total Power Consumption

The total power consumption of the mmWave and THz system is the overall power costs of the power amplifiers and other circuit components. Specifically, the total power consumption for the fully-connected structure is given by

$$\begin{aligned} P_{tot}^{a} &= P_c^a + KNP_{PA}^a \\ &= \begin{cases} \frac{2}{\pi}\sqrt{KNP_{max}}\sqrt{P_t^a} + P_c^a, \\ \qquad\qquad 0 < P_t^a \leq 0.25KNP_{max}, \\ \frac{6}{\pi}\sqrt{KNP_{max}}\sqrt{P_t^a} + P_c^a - \frac{2}{\pi}KNP_{max}, \\ \qquad\qquad 0.25KNP_{max} < P_t^a \leq KNP_{max}. \end{cases} \end{aligned} \tag{2.27}$$

For the array-of-subarrays structure, we denote $\mathcal{K}_1 = \{k \in \mathcal{K} | 0 < \frac{P_t^b\|\tilde{\mathbf{f}}_k\|^2}{JN} \leq 0.25P_{max}\}$ and $\mathcal{K}_2 = \{k \in \mathcal{K} | 0.25P_{max} < \frac{P_t^b\|\tilde{\mathbf{f}}_k\|^2}{JN} \leq P_{max}\}$, where $|\mathcal{K}_1| \triangleq K_1$ and $|\mathcal{K}_2| \triangleq K_2$. Accordingly, the

total power cost can be expressed as

$$
\begin{aligned}
P_{tot}^{b} &= P_{c}^{b} + \sum_{k=1}^{K} N P_{PA}^{b}(k) \\
&= \begin{cases}
\frac{2}{\pi}\sqrt{\frac{NP_{max}}{J}}\Big(\sum\limits_{k=1}^{K}\|\tilde{\mathbf{f}}_k\|\Big)\sqrt{P_t^b} + P_c^b, \\
\qquad\qquad 0 < P_t^b \le \min\limits_k\Big(\frac{0.25JNP_{max}}{\|\tilde{\mathbf{f}}_k\|^2}\Big), \\
\frac{2}{\pi}\sqrt{\frac{NP_{max}}{J}}\Big(\sum\limits_{k\in\mathcal{K}_1}\|\tilde{\mathbf{f}}_k\| + \sum\limits_{k\in\mathcal{K}_2} 3\|\tilde{\mathbf{f}}_k\|\Big)\sqrt{P_t^b} + P_c^b - \frac{2}{\pi}K_2 NP_{max}, \\
\qquad\qquad \min\limits_k\Big(\frac{0.25JNP_{max}}{\|\tilde{\mathbf{f}}_k\|^2}\Big) < P_t^b \le \max\limits_k\Big(\frac{0.25JNP_{max}}{\|\tilde{\mathbf{f}}_k\|^2}\Big), \\
\frac{6}{\pi}\sqrt{\frac{NP_{max}}{J}}\Big(\sum\limits_{k=1}^{K}\|\tilde{\mathbf{f}}_k\|\Big)\sqrt{P_t^b} + P_c^b - \frac{2}{\pi}KNP_{max}, \\
\qquad\qquad \max\limits_k\Big(\frac{0.25JNP_{max}}{\|\tilde{\mathbf{f}}_k\|^2}\Big) < P_t^b \le \min\limits_k\Big(\frac{JNP_{max}}{\|\tilde{\mathbf{f}}_k\|^2}\Big).
\end{cases}
\end{aligned} \tag{2.28}
$$

From (2.27) and (2.28), in general, the total power consumption can be expressed as

$$P_{tot} = c_1\sqrt{P_t} + c_2. \tag{2.29}$$

Specifically, for the fully-connected structure,

$$c_1 = \begin{cases} \frac{2}{\pi}\sqrt{KNP_{max}}, & 0 < P_t \le a_1, \\ \frac{6}{\pi}\sqrt{KNP_{max}}, & a_1 < P_t \le a_2, \end{cases} \tag{2.30}$$

and

$$c_2 = \begin{cases} P_c^a, & 0 < P_t \le a_1, \\ P_c^a - \frac{2}{\pi}KNP_{max}, & a_1 < P_t \le a_2, \end{cases} \tag{2.31}$$

where $a_1 \triangleq 0.25KNP_{max}$ and $a_2 \triangleq KNP_{max}$. For the array-of-subarrays structure,

$$c_1 = \begin{cases} \frac{2}{\pi}\sqrt{\frac{NP_{max}}{J}}\Big(\sum\limits_{k=1}^{K}\|\tilde{\mathbf{f}}_k\|\Big), & 0 < P_t \le b_1, \\ \frac{2}{\pi}\sqrt{\frac{NP_{max}}{J}}\Big(\sum\limits_{k\in\mathcal{K}_1}\|\tilde{\mathbf{f}}_k\| + \sum\limits_{k\in\mathcal{K}_2} 3\|\tilde{\mathbf{f}}_k\|\Big), & b_1 < P_t \le b_2, \\ \frac{6}{\pi}\sqrt{\frac{NP_{max}}{J}}\Big(\sum\limits_{k=1}^{K}\|\tilde{\mathbf{f}}_k\|\Big), & b_2 < P_t \le b_3, \end{cases} \tag{2.32}$$

and

$$c_2 = \begin{cases} P_c^b, & 0 < P_t \leq b_1, \\ P_c^b - \frac{2}{\pi} K_2 N P_{max}, & b_1 < P_t \leq b_2, \\ P_c^b - \frac{2}{\pi} K N P_{max}, & b_2 < P_t \leq b_3, \end{cases} \tag{2.33}$$

where $b_1 \triangleq \min_k \left(\frac{0.25JNP_{max}}{\|\tilde{\mathbf{f}}_k\|^2} \right)$, $b_2 \triangleq \max_k \left(\frac{0.25JNP_{max}}{\|\tilde{\mathbf{f}}_k\|^2} \right)$, and $b_3 \triangleq \min_k \left(\frac{JNP_{max}}{\|\tilde{\mathbf{f}}_k\|^2} \right)$.

We can see from (2.27) and (2.28) that, the total power consumption of the fully-connected structure is independent of the beamforming scheme while it is highly dependent on the digital beamforming, $\mathbf{F}$, for the array-of-subarrays structure. Furthermore, since $\sum_{k=1}^{K} \|\tilde{\mathbf{f}}_k\|^2 = J$ and much fewer phase shifters are used in the array-of-subarrays structure, the total power consumption of the array-of-subarrays structure in (2.28) is generally less than that of the fully-connected structure in (2.27).

2.1.4 Problem Formulation

Given the system model, the channel model and the power consumption model, the energy efficiency of the mmWave and THz system, which is defined as the ratio of system throughput to total power consumption, can be expressed as

$$\xi_{EE} \triangleq \frac{R}{P_{tot}} = \frac{\sum_{j \in \mathcal{J}} R_j}{c_1 \sqrt{P_t} + c_2}, \tag{2.34}$$

where the achievable rate of user j for the system with bandwidth B is given by

$$R_j = B \log_2 \left(1 + \frac{\frac{P_t}{J} \left| \mathbf{v}_j^* \mathbf{H}_j \mathbf{W} \mathbf{f}_j \right|^2}{\sum_{i \neq j} \frac{P_t}{J} \left| \mathbf{v}_j^* \mathbf{H}_j \mathbf{W} \mathbf{f}_i \right|^2 + \sigma_j^2} \right). \tag{2.35}$$

Thus, the energy efficiency of the system is jointly determined by the effective transmit power, P_t, and the beamforming scheme, $\mathbf{F}$, $\mathbf{W}$, and $\mathbf{V}$.

By capturing the characteristics of the mmWave and THz channels and exploiting different system structures, we aim to develop low-complexity hybrid beamforming and optimal power control strategies for spectral- and energy-efficient design of both structures and determine the more suitable architecture through comparison.

2.2 Hybrid Beamforming and Achievable Rate

Given the mmWave and THz system in the previous section, we will design low-complexity hybrid beamforming for the two different structures in this section, including the analog beamforming in RF domain and the digital beamforming at baseband for interference cancellation.

2.2.1 Analog Beamforming

First, we will focus on the analog beamforming design with phase shifters. Since the phase shifters are mostly digitally-controlled in the mmWave and THz bands, only quantized angles are available. Hence, the beamforming angles need to be selected from finite-size codebooks [39, 43, 46]. Specifically, we consider the beamsteering codebooks here, which have the same form as the array steering vectors in (2.13) and are parameterized with a series of simple angles. As a result, the analog beamforming design in the system can be regarded as beamsteering codebook searching, which is carried out on an RF-chain basis. We denote $\mathcal{W}$ and $\mathcal{V}$ as the beamsteering codebooks at the AP and the users, respectively. Moreover, the selected beamsteering vectors for the k-th RF chain and user j are denoted as $\mathbf{a}_t(KN, \hat{\phi}_k^t)/\mathbf{a}_t(N, \hat{\phi}_k^t)$ and $\mathbf{a}_r(M, \hat{\theta}_j^r)$, respectively, where $\hat{\phi}_k^t$ is the selected transmit beamforming angle for the k-th RF chain and $\hat{\theta}_j^r$ is the selected receive beamforming angle for user j. In the following, we will present the searching processes for the two structures.

2.2.1.1 Fully-Connected Structure

To obtain the transmit analog beamforming matrix in (2.2) for the fully-connected structure, the analog beamforming searching is developed as Algorithm 2.1 in Table 2.1, which is an extension of the scheme in [46]. The analog beamforming associated with one RF chain is designed for one user only as in [46], neglecting the interference to other users. Different from [46], where the beamforming design is only for the situation when the number of users is equal to the number of RF chains, i.e., $J = K$, the beamforming searching in

Table 2.1 Analog Beamforming for the Fully-Connected Structure

Algorithm 2.1 Analog Beamforming Searching for the Fully-Connected Structure

1: **Initialize** the transmit beamsteering codebook for user j, $\mathcal{W}_j = \mathcal{W}$, and the receive beamsteering codebook, $\mathcal{V}$.
2: **for** $k = 1 : K$ **do**
3: **Initialize** $j = (k-1) \bmod J + 1$.
4: **if** $k \leq J$ **then**
5: Search $\mathcal{W}_j$ and $\mathcal{V}$ to find the beamsteering vectors, $\mathbf{a}_t(KN, \hat{\phi}_k^t)$ and $\mathbf{a}_r(M, \hat{\theta}_j^r)$, such that[1]
$$\{\mathbf{a}_t(KN, \hat{\phi}_k^t), \mathbf{a}_r(M, \hat{\theta}_j^r)\} = \underset{\substack{\phi_k^t \in \mathcal{W}_j, \\ \theta_j^r \in \mathcal{V}}}{\arg\max} \left|\mathbf{a}_r^*(M, \theta_j^r)\mathbf{H}_j\mathbf{a}_t(KN, \phi_k^t)\right|^2.$$
6: **else**
7: Search $\mathcal{W}_j$ to find the $KN \times 1$ beamsteering vector, $\mathbf{a}_t(KN, \hat{\phi}_k^t)$, such that
$$\mathbf{a}_t(KN, \hat{\phi}_k^t) = \underset{\phi_k^t \in \mathcal{W}_j}{\arg\max} \left|\mathbf{a}_r^*(M, \hat{\theta}_j^r)\mathbf{H}_j\mathbf{a}_t(KN, \phi_k^t)\right|^2.$$
8: **end if**
9: **Update** $\mathcal{W}_j = \mathcal{W}_j - \{\hat{\phi}_k^t\}$.
10: **end for**
11: **Obtain** $\mathbf{w}_k = \frac{1}{\sqrt{KN}}\mathbf{a}_t(KN, \hat{\phi}_k^t)$ and $\mathbf{v}_j = \frac{1}{\sqrt{M}}\mathbf{a}_r(M, \hat{\theta}_j^r)$.

Algorithm 2.1 can be applied for any cases when $K \geq J$. Particularly, to ensure the overall system performance and the fairness among users, each user is assigned one RF chain for analog beamforming in each searching cycle, where the user at a longer distance with more severe path loss will be assigned first. Accordingly, the codebook searching in Algorithm 2.1 is divided into two parts. For the first J RF chains, the searching is performed at both the AP and users to find the optimal transmit and receive beamsteering directions for each user. Then, with the selected receive beamforming vectors at the user side, the searching is conducted successively at the AP only for the remaining RF chains, choosing unselected angles from each user's transmit codebook so that the received signal power is as large as possible, until all the RF chains are assigned. Note that selecting unchosen angles from user's transmit codebook is to avoid duplicated phase shifting for different RF chains. Since $M \ll KN$, the beam generated by the user is wide enough to receive multiple

[1]The multiuser RF beamforming training strategies will be provided in Chapter 3.

Table 2.2 Analog Beamforming for the Array-of-Subarrays Structure

Algorithm 2.2 Analog Beamforming Searching for the Array-of-Subarrays Structure

1: **Initialize** the transmit beamsteering codebook, $\mathcal{W}$, and the receive beamsteering codebook, $\mathcal{V}$.
2: **for** $k = 1 : K$ **do**
3: **Initialize** $j = (k-1) \bmod J + 1$.
4: **if** $k \leq J$ **then**
5: Search $\mathcal{W}$ and $\mathcal{V}$ to find the $N \times 1$ beamsteering vector, $\mathbf{a}_t(N, \hat{\phi}_k^t)$, and $\mathbf{a}_r(M, \hat{\theta}_j^r)$, such that
$$\{\mathbf{a}_t(N, \hat{\phi}_k^t), \mathbf{a}_r(M, \hat{\theta}_j^r)\} = \arg\max_{\substack{\phi_k^t \in \mathcal{W}, \\ \theta_j^r \in \mathcal{V}}} \left|\mathbf{a}_r^*(M, \theta_j^r)\mathbf{H}_{j,k}\mathbf{a}_t(N, \phi_k^t)\right|^2.$$
6: **else**
7: $\mathbf{a}_t(N, \hat{\phi}_k^t) = \mathbf{a}_t(N, \hat{\phi}_j^t)$.
8: **end if**
9: **end for**
10: **Obtain** $\mathbf{w}_k = \frac{1}{\sqrt{N}}\mathbf{a}_t(N, \hat{\phi}_k^t)$ and $\mathbf{v}_j = \frac{1}{\sqrt{M}}\mathbf{a}_r(M, \hat{\theta}_j^r)$.

narrow beams from the AP and harvest part of the multiplexing gain from the NLOS paths. The complexity of the algorithm is $O(K|\mathcal{W}||\mathcal{V}|)$.

2.2.1.2 Array-of-Subarrays Structure

Different from the fully-connected structure, RF chains in the array-of-subarrays structure are connected to different subsets of antennas, each of which has only one beamsteering direction. Thus, the RF-chain-based codebook searching can also be viewed as subarray-based beamforming. Here, the transmit analog beamforming matrix, $\mathbf{W}$, is denoted as in (2.3), and the channel matrix of user j is denoted as

$$\mathbf{H}_j = [\mathbf{H}_{j,1}, \mathbf{H}_{j,2}, ..., \mathbf{H}_{j,K}], \tag{2.36}$$

where $\mathbf{H}_{j,k}$ is the channel from the k-th subarray to user j. It should be noted that, for the channel in (2.5), there are merely phase differences between $\mathbf{H}_{j,k}$ and $\mathbf{H}_{j,k'}$, where $k, k' \in \mathcal{K}$ and $k \neq k'$. The analog beamforming design for the array-of-subarrays structure is described as Algorithm 2.2 in Table 2.2. Similarly, the analog beamforming of one subarray is designed for one user only as the fully-connected structure and the searching process is

also in order of user's distance. Therefore, the codebook searching algorithm consists of two parts as well. At first, the first J subarrays and all the users search the codebooks to find the best transmit and receive beamsteering vectors. Then, for the remaining subarrays, the beamforming angles of the subarrays assigned to user j are set to be that of the j-th subarray. Since the channels between one user and different subarrays have the same path gain and AoD/AoA, steering to the same transmit beamforming direction for different subarrays will only result in phase differences for the received signals, which can be inverted by digital beamforming at baseband. Note that, in this structure, users can receive multiple beams from different subarrays while only the gain of the strongest path is harvested by the beamsteering. The complexity of the algorithm is $O(J|\mathcal{W}||\mathcal{V}|)$.

As proved in [42, 43], the optimal singular-value-decomposition (SVD) beamforming vectors for the channel in (2.5) converge to $\mathbf{a}_t(KN, \phi_k^t)$ and $\mathbf{a}_r(M, \theta_j^r)$ at large antenna regime. Thus, the searching procedure in Algorithm 2.1 and Algorithm 2.2 can be viewed as a near-optimal singular vector seeking process, both having linear complexity. Since the LOS path is much stronger than the NLOS path in higher-mmWave and THz bands, the beamforming searching in this process is to find the angles in the codebooks, which are close to the LOS direction or the directions jointly determined by the first-order reflections. With the analog beamforming, the equivalent channel, $\hat{\mathbf{H}}$, at baseband can be denoted as

$$\hat{\mathbf{H}} = [\hat{\mathbf{h}}_1, \hat{\mathbf{h}}_2, ..., \hat{\mathbf{h}}_J]^T, \tag{2.37}$$

where

$$\hat{\mathbf{h}}_j^T = \mathbf{v}_j^* \mathbf{H}_j \mathbf{W}. \tag{2.38}$$

As a result, the information needed to be fed back is simply this $K \times 1$ effective channel vector while the explicit channel information of each antenna elements, $\mathbf{H}_j$, is no longer needed. Since the number of RF chains, K, is much smaller than the number of antenna elements, KN, the overhead will be significantly reduced.

2.2.2 Digital Beamforming with Interference Cancellation

Given the analog beamforming, we will design the digital beamforming for interference cancellation among different users in this subsection. Note that the effective channel, $\hat{\mathbf{H}}$, is assumed to be known at the AP through feedback.

Therefore, the digital beamforming for the two structures can be designed in the same manner. Specifically, the zero-forcing digital beamformer is adopted, which can be implemented by pseudo-inverse as

$$\mathbf{F} = [\mathbf{f}_1, \mathbf{f}_2, ..., \mathbf{f}_J] = \hat{\mathbf{H}}^*(\hat{\mathbf{H}}\hat{\mathbf{H}}^*)^{-1}\mathbf{\Delta} = \hat{\mathbf{F}}\mathbf{\Delta}, \tag{2.39}$$

where $\hat{\mathbf{F}} = [\hat{\mathbf{f}}_1, \hat{\mathbf{f}}_2, ..., \hat{\mathbf{f}}_J] \triangleq \hat{\mathbf{H}}^*(\hat{\mathbf{H}}\hat{\mathbf{H}}^*)^{-1}$, and $\mathbf{\Delta}$ is a diagonal matrix regulating the digital beamforming power such that $\|\mathbf{W}\mathbf{f}_j\|^2 = 1,\ j \in \mathcal{J}$. Particularly, the j-th diagonal element of $\mathbf{\Delta}$ is given by $\mathbf{\Delta}_{j,j} = \frac{1}{\|\mathbf{W}\hat{\mathbf{f}}_j\|}$.

Consequently, the hybrid beamforming proposed in this paper avoids processing the large channel matrix directly as in [43] and has much lower complexity, which is more practical for implementation.

2.2.3 Achievable Rate

For a flat-fading narrowband channel with bandwidth B, centered around the frequency f, the achievable rate of user j with the hybrid beamforming is given by

$$\begin{aligned} R_j &= B\log_2\left(1 + \frac{P_t}{J\sigma_j^2}|\hat{\mathbf{h}}_j^T\mathbf{f}_j|^2\right) \\ &= B\log_2\left(1 + \frac{P_t}{J\sigma_j^2}|\mathbf{\Delta}_{j,j}|^2\right) \\ &= B\log_2\left(1 + \frac{P_t}{J\sigma_j^2\|\mathbf{W}\hat{\mathbf{f}}_j\|^2}\right) \\ &\triangleq B\log_2(1+\beta_j P_t), \qquad\qquad j \in \mathcal{J}, \end{aligned} \tag{2.40}$$

where σ_j^2 is the noise power at user j and $\beta_j \triangleq \frac{1}{J\sigma_j^2\|\mathbf{W}\hat{\mathbf{f}}_j\|^2}$. Then, the relation between the achievable rates of the two different structures is given in the following proposition, which is proved in Appendix A.1.

Proposition 2.1 *When $K = J$, by considering the insertion loss in the RF domain, the achievable rate of user j with the proposed hybrid beamforming, R_j^a, for the fully-connected structure and the achievable rate for the array-of-subarrays structure, R_j^b, generally satisfy*

$$R_j^b \geq R_j^a, \qquad j \in \mathcal{J}. \tag{2.41}$$

Specifically, when $\frac{P_s}{J\sigma_j^2} \gg 1$,

$$R_j^b - R_j^a \geq B \log_2 J, \qquad j \in \mathcal{J}. \tag{2.42}$$

From Proposition 2.1, we know that, the gain obtained by sharper beams is hard to compensate for the insertion loss introduced by sharing antennas. Furthermore, the gap between the two rates mainly results from the direct combining of analog signals on each antenna.

Given Proposition 2.1, we can easily compare the achievable rates of the two different structures when $K \geq J$. For the array-of-subarrays structure, additional RF chains are used to form beams to the strongest directions of different subarrays while they are used to beam to the remaining directions for the fully-connected structure to avoid duplicated operation on the shared antennas. As a result, the corresponding beamforming gain of the array-of-subarrays structure is larger than that of the fully-connected structure. Therefore, the achievable rate of the array-of-subarrays structure would be still greater than that of the fully-connected structure.

2.3 Energy-Efficient Design

With the hybrid beamforming and system's sum-rate, we will focus on the energy-efficient design of the mmWave and THz system in this section.

For the mmWave and THz system in Fig. 2.1, the energy efficiency with the hybrid beamforming is given by [81, 82]

$$\xi_{EE} = \frac{\sum_{j=1}^{J} B \log_2 (1 + \beta_j P_t)}{c_1 \sqrt{P_t} + c_2}, \tag{2.43}$$

where c_1, c_2, and related constraints on P_t are defined in (2.29) for different structures. Our objective is to find the optimal transmit power so that the energy efficiency of the system is maximized. It should be noted that the transmit power here, P_t, is the effective power considering the insertion loss of the circuit components and is equal for all users.

The following lemma, proved in Appendix A.2, reveals the property of the energy efficiency function and facilitates the system design.

Lemma 2.1 *The energy efficiency, ξ_{EE}, is a piecewise quasi-concave function of P_t for $P_t > 0$.*

According to Lemma 2.1, there exists a unique global maximum of energy efficiency, which is achieved at $\frac{\partial \xi_{EE}}{\partial P_t} = 0$. Therefore, with the PA output power constraints, the optimal transmit power to maximize the energy efficiency of the system can be obtained as Theorem 2.1, which is proved in Appendix A.3.

Theorem 2.1 *For the fully-connected structure, the maximal energy efficiency is achieved at*

$$P_t^\star = \begin{cases} [\hat{P}_t]_0^{a_1}, & 0 < P_t \le a_1, \\ [\hat{P}_t]_{a_1}^{a_2}, & a_1 < P_t \le a_2, \end{cases} \tag{2.44}$$

while for the array-of-subarrays structure, the maximal energy efficiency is achieved at

$$P_t^\star = \begin{cases} [\hat{P}_t]_0^{b_1}, & 0 < P_t \le b_1, \\ [\hat{P}_t]_{b_1}^{b_2}, & b_1 < P_t \le b_2, \\ [\hat{P}_t]_{b_2}^{b_3}, & b_2 < P_t \le b_3, \end{cases} \tag{2.45}$$

where $[x]_a^b = a$ if $x < a$, $[x]_a^b = b$ if $x > b$, and $[x]_a^b = x$ otherwise. Specifically, $\hat{P}_t$ is the solution of[2]

$$\frac{2}{\ln 2}(c_1 P_t + c_2\sqrt{P_t}) \sum_{j=1}^{J} \frac{\beta_j}{1+\beta_j P_t} - c_1 \sum_{j=1}^{J} \log_2(1+\beta_j P_t) = 0, \tag{2.46}$$

and $a_1, a_2, b_1, b_2, b_3, c_1, c_2$ are defined in (2.29).

[2]Note that the bisection method can be used to obtain $\hat{P}_t$.

Theorem 2.1 demonstrates that there are at most two candidates of $P_t^\star$ for the fully-connected structure and at most three candidates for the array-of-subarrays structure. Therefore, the overall optimal transmit power can be obtained by simply checking which one maximizes the system's energy efficiency.

In summary, the energy efficiency of the mmWave and THz system is jointly determined by the hybrid beamforming scheme and the system power consumption, with different optimal transmit power for different conditions. Since the array-of-subarrays structure has advantages over the fully-connected structure in both sum-rate and total power consumption, it generally has a better performance in energy efficiency for the mmWave and THz system.

2.4 Simulation Results

In this section, simulation results are provided to illustrate the energy efficiency of the mmWave and THz system with the proposed hybrid beamforming and power control and validate the performance of the two different structures.

An indoor mmWave and THz system with three users is considered, where the distances between the users and the AP are $d_1 = 10\ m$, $d_2 = 5\ m$, and $d_3 = 1\ m$, respectively. The operating frequency is set as 0.1 THz, i.e, 100 GHz, and the bandwidth is set as $B = 5$ GHz. For simplicity, we assume that there exist three first-order reflected clusters and four second-order reflection components in our simulation as [48]. For the system, the number of the RF chains is $K = 9$, the antennas at the AP are set as $KN = 72$ with $N = 8$, and the number of user's antennas is $M = 8$. Meanwhile, the antenna gains are set as $G_t = G_r = 20$ dBi, and the noise power, σ_j^2, is set as -75 dBm for all $j \in \mathcal{J}$. Specifically, the maximum output power of the PA is $P_{max} = 20$ dBm [83] and the PA power gain is $G_{PA} = 20$ dB. Moreover, the power costs of other circuit components are provided in Table 2.3. Note that, the overall power consumption of the RF chain is around 120 mW, which is the sum of the power costs of the DAC, the mixers, the LO, and the filters as in Table 2.3.

Table 2.3 Power Costs of the Circuit Components

Component	Power cost (mW)	Reference
Baseband	200	[75]
DAC	75	[84]
Mixer	23	[83]
LO	5	[83]
Filter	15	[75]
Phase shifter	20	[85]

As a benchmark, the digital-only beamforming with block diagonalization (BD) is considered [86], where each antenna is connected to one dedicated RF chain without phase shifters and no power losses are introduced by splitters or combiners.

In Fig. 2.3, we plot the system spectral efficiency versus the total initial transmit power. As shown in Fig. 2.3, the spectral efficiency generally increases with the transmit power. Specifically, the digital-only beamforming provides the best performance as expected, by using a larger number of RF chains with higher circuit complexity and no additional insertion loss. Moreover, the spectral efficiency of the array-of-subarrays structure outperforms that of the fully-connected structure due to less insertion loss, which validates our analysis. In addition, we can see from Fig. 2.3 that, in high signal-to-noise-ratio (SNR) conditions, the gap of the spectral efficiency for the two structures gradually exceeds $\log_2 J$ with $J = 3$ as indicated in Proposition 2.1.

We compare the energy efficiency of different structures in Fig. 2.4. From Fig. 2.4, the energy efficiency increases with the transmit power first, then decreases rapidly as the power becomes large. By using fewer RF chains, the systems with the fully-connected structure or the array-of-subarrays structure are much more energy-efficient than the systems without hybrid structure. Furthermore, compared with the fully-connected structure, the array-of-subarrays structure shows about 30% gain in energy efficiency, which results from the simpler circuit design with fewer components and less insertion loss. In addition, we plot the optimal transmit power to maximize the system's energy efficiency for the two structures in Fig. 2.4, which is obtained according to Theorem 2.1. These optimal points

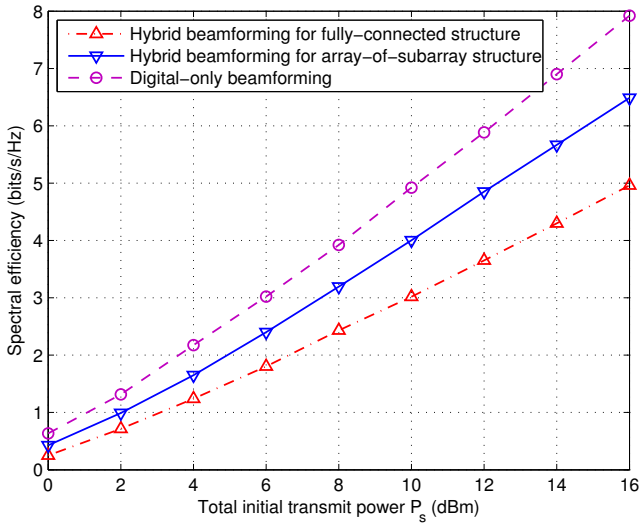

Fig. 2.3 System spectral efficiency versus total initial transmit power.

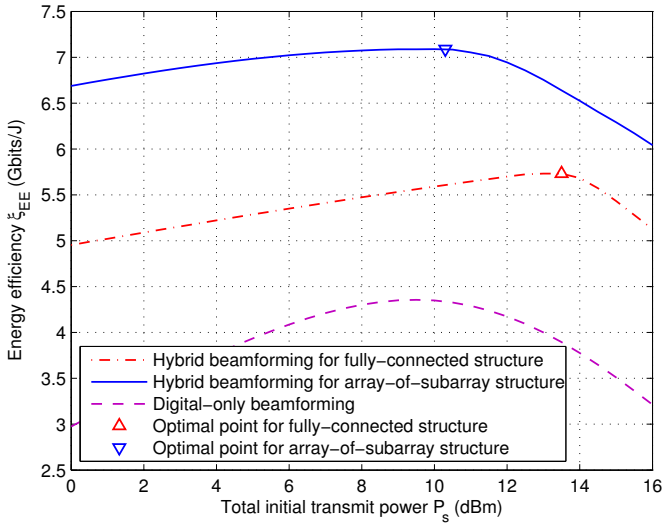

Fig. 2.4 System energy efficiency versus total initial transmit power.

match the energy efficiency curves, which validates the effectiveness of the proposed optimal power control strategies. In particular, because more power is needed to cover the insertion loss in the fully-connected structure, the optimal transmit power of this structure is larger than that of the array-of-subarrays structure.

Fig. 2.5 demonstrates the system energy efficiency versus spectrum efficiency. We can observe from Fig. 2.5 that, there exists a tradeoff between the spectrum efficiency and energy efficiency. Again, the array-of-subarrays structure has a better performance on energy

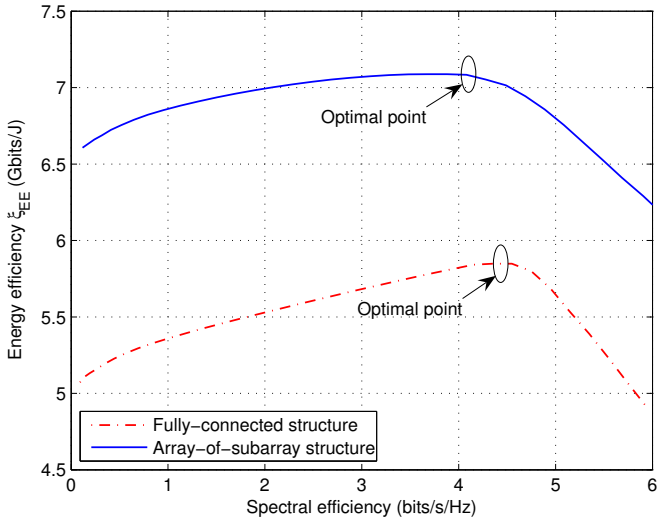

Fig. 2.5 System energy efficiency versus spectral efficiency.

efficiency than the fully-connected structure.

We plot the energy efficiency of the system as a function of the number of RF chains in Fig. 2.6. Here, the total initial transmit power is set as $P_s = 10$ dBm, and $N = 8$. From Fig. 2.6, the energy efficiency of the system generally decreases with the number of RF chains. The reason is that, as the total number of the splitters, combiners, and phase shifters scales with the number of RF chains, both structures would suffer more from the system power consumption. In particular, the energy efficiency of the array-of-subarrays structure shows advantages over that of the fully-connected structure since it consumes less power and is with constant insertion loss regardless of the number of RF chains.

2.5 Conclusions

This chapter has investigated a multiuser indoor mmWave and THz communication system with two different structures. Specifically, a Doherty-PA-based nonlinear system power consumption model with insertion power loss has been developed. By exploiting the mmWave and THz channels, we have designed different hybrid beamforming schemes with low complexity for the two structures. Moreover, the energy efficiency of the system has been studied for each structure, and the optimal power control strategies have

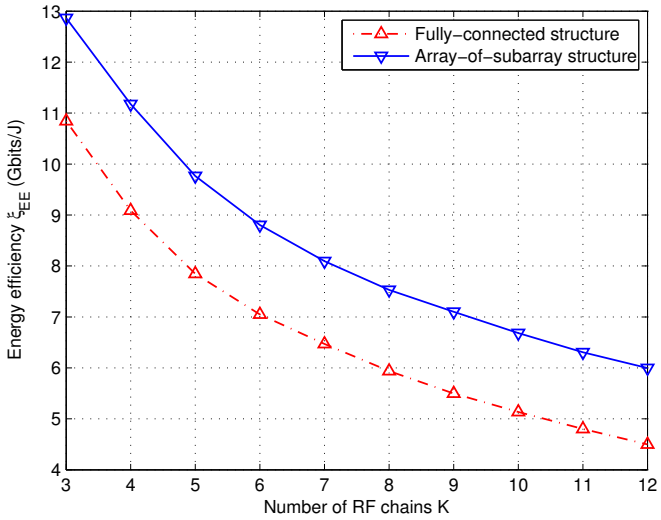

Fig. 2.6 System energy efficiency versus the number of RF chains.

been proposed. Several important results have been obtained. First, the total power consumption of the array-of-subarrays structure is less than that of the fully-connected structure. Second, considering the insertion loss, the achievable rate with the proposed hybrid beamforming for the array-of-subarrays structure is generally larger than that of the fully-connected structure. Last but not least, given the achievable sum-rate and the total power consumption, the energy efficiency of the array-of-subarrays structure outperforms that of the fully-connected structure. Therefore, the array-of-subarrays structure is more suitable and practical for mmWave and THz system design.

CHAPTER 3

SUBARRAY-BASED COORDINATED BEAMFORMING TRAINING

Given the advantages of the array-of-subarrays structure for mmWave and THz communications, we will design the associated beamforming training strategies in this chapter. Our goal is to investigate beamforming training with hybrid processing to extract the dominant channel information. Specifically, the impact of time-delay phase shifters will be captured. Then, multi-resolution time-delay codebooks with subarray coordination will be developed.

The rest of this chapter is organized as follows. Section 3.1 overview the associated mmWave and THz communication systems. In Section 3.2, we propose two multi-resolution time-delay codebooks with beam adaptation and dynamic approximation. A low-complexity system implementation is designed in Section 3.3. Then, a hierarchical beamforming training strategy is developed in Section 3.4. Simulation results are provided in Section 3.5 to evaluate the effectiveness of the proposed codebooks and beamforming training strategy. Finally, we conclude the chapter in Section 3.6.

3.1 System Overview

In this section, we will provide an overview of the mmWave and THz system with the time-delay components.

3.1.1 System Model

Fig. 3.1 demonstrates a multiuser indoor mmWave and THz system similar to Fig. 2.1, consisting of an access point (AP) with KN tightly-packed antennas but only K RF chains. Specifically, an RF chain exclusively drives a disjoint subset of antennas via a group of time-delay phase shifters, constituting an N-element subarray. At the user side, only one RF chain and an M-element array are equipped. For the mmWave and THz system, antennas

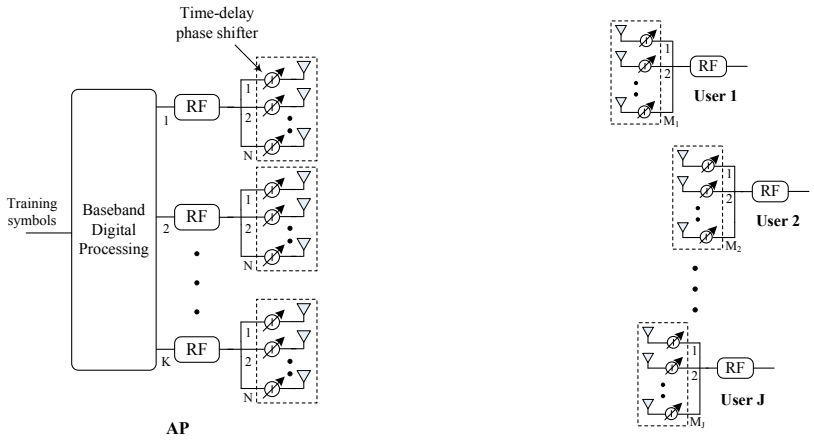

Fig. 3.1 The mmWave and THz communication system.

are equally spaced and the subarray spacing is the same as the antenna spacing, which is denoted as r.

We will first focus on the design for one user. Similar to Fig. 2.1, the received signal at the user side is given by

$$y = \mathbf{v}^* \mathbf{H} \mathbf{W} \mathbf{f} s + \mathbf{v}^* \mathbf{n}, \tag{3.1}$$

where s is the transmitted training symbol such that $\mathbb{E}[|s|^2] = P_s$ with P_s being the transmit power. $\mathbf{H}$ is the $M \times KN$ mmWave or THz channel matrix between the AP and the user. $\mathbf{W}$ is the $KN \times K$ transmit analog beamforming matrix implemented by the phase shifters, which is expressed as

$$\mathbf{W} = \begin{bmatrix} \mathbf{w}_1 & \mathbf{0} & \cdots & \mathbf{0} \\ \mathbf{0} & \mathbf{w}_2 & \cdots & \mathbf{0} \\ \vdots & \vdots & \vdots & \vdots \\ \mathbf{0} & \mathbf{0} & \cdots & \mathbf{w}_K \end{bmatrix} \tag{3.2}$$

with $\mathbf{w}_k = [w_{k,1}, w_{k,2}, ..., w_{k,N}]^T$ being an $N \times 1$ vector such that $|w_{k,n}|^2 = \frac{1}{N},\ n = 1, 2, ..., N$. $\mathbf{f} = [f_1, f_2, ..., f_K]^T$ is the $K \times 1$ vector for baseband digital processing satisfying $\|\mathbf{W}\mathbf{f}\|^2 = 1$.[3] $\mathbf{v} = [v_1, v_2, ..., v_M]^T$ is the $M \times 1$ receive analog beamforming vector performed at the user side such that $|v_m|^2 = \frac{1}{M},\ m = 1, 2, ..., M$. And, $\mathbf{n}$ is the $M \times 1$ Gaussian noise vector at the

[3] Since $\|\mathbf{w}_k\|^2 = 1$ for $k = 1, 2, ..., K$, this power constraint is equivalent to $\|\mathbf{f}\|^2 = 1$.

user, i.e., $\mathbf{n} \sim \mathcal{CN}(\mathbf{0}, \sigma^2\mathbf{I})$.

3.1.2 Problem Description

For the mmWave and THz system in Fig. 3.1, signal processing is conducted on a subarray basis. With the digital baseband, subarrays can cooperate to further harvest the beamforming gain as well as the spatial diversity gain. Thanks to the subarray-based hybrid structure and the LOS-dominant channels, only the dominant channel information is required for transmission design, which can be obtained through beamforming training and scanning. Therefore, in this chapter, we aim to design effective beamforming training strategies with the array-of-subarrays structure, which should not only exploit the gain provided by the subarrays but also capture the nature of circuit hardware.

3.2 Time-Delay Codebook Design with Subarray Coordination

For mmWave and THz communications, beamforming training is usually accomplished through signal switching using beamforming codebooks [39, 41, 44, 87]. Accordingly, by considering the nature of time-delay phase shifters and the subarray-based hybrid structure, we will design a time-delay codebook with subarray coordination in this section.

3.2.1 Time-Delay Codebook Structure

We will first introduce the basic structure of the time-delay codebook based on the time-delay phase shifters. For a time delay t, the shifted phase, φ, is given by

$$\varphi = 2\pi f t = \frac{2\pi}{\lambda} ct \triangleq \frac{2\pi r}{\lambda} \sin\hat{\phi}, \tag{3.3}$$

where $\hat{\phi} \in [-\frac{\pi}{2}, \frac{\pi}{2}]$ is the corresponding physical angle. According to (3.3), the shifted phase with respect to the true time delay varies over frequencies but associates with a common physical angle [12]. As a result, the time delay has a one-to-one matching with the physical angle regardless of the bandwidth,[4] which means the time-delay codebook can

[4]Note that, for the physical angle in $[-\pi, -\frac{\pi}{2})$ and $(\frac{\pi}{2}, \pi)$, equivalent codewords can be found in the time-delay codebook.

also be defined by the physical angle. Therefore, the codebook can be constructed based on the time-related physical angle, which is given by $t(\hat{\phi}) = \frac{r}{c}\sin\hat{\phi}$. As time-delay lines are usually implemented by digitally-controlled integrated gates [23, 32, 33], only a limited number of time delays and corresponding angles are available, which can be denoted by a time-delay set Φ_t. It should be noted that, different from the quantized phase set defined by conventional finite-bit phase shifters, the time-delay set has more freedom in designing time delays. Consequently, it can have either regular or irregular time-related phases with any form. In this paper, we assume the time-delay set, Φ_t, has n replica of the time for a specific time-related angle, where $1 \leq n \leq N-1$. That is to say, $nt(\hat{\phi}) \in \Phi_t$, for any $t(\hat{\phi}) \in \Phi_t$ and $1 \leq n \leq N-1$. It is worth mentioning that, the time delays associated with the same time-related angle match the structure of the subarray steering vector in (2.13).

For the mmWave and THz system, a multi-resolution codebook will be developed to reduce the training overhead as in [41, 44, 87]. In particular, for a U-level time-delay codebook, we denote $\mathbf{q}_{u,i} = \mathbf{W}_{u,i}\mathbf{f}_{u,i}$ as the i-th codeword in the u-th level, $\Psi_{u,i}$ as the angular coverage of codeword $\mathbf{q}_{u,i}$, and I_u as the number of the codewords in the u-th level. In general, the codewords in each level are uniformly designed to cover the whole angular space, i.e.,

$$\Psi_{u,i} = [-\frac{\pi}{2} + \frac{i-1}{I_u}\pi, -\frac{\pi}{2} + \frac{i}{I_u}\pi],\ 1 \leq i \leq I_u,\ 1 \leq u \leq U, \tag{3.4}$$

and

$$\bigcup_{i=1}^{I_u} \Psi_{u,i} = [-\frac{\pi}{2}, \frac{\pi}{2}], \quad 1 \leq u \leq U. \tag{3.5}$$

Ideally, each codeword should provide a constant beamforming gain over its angular coverage, which can be expressed as

$$\begin{aligned} \left|\mathbf{a}^*(KN,\phi)\mathbf{q}_{u,i}\right|^2 &= \left|\mathbf{a}^*(KN,\phi)\mathbf{W}_{u,i}\mathbf{f}_{u,i}\right|^2 \\ &= \begin{cases} C_u, & \phi \in \Psi_{u,i}, \\ 0, & \text{otherwise}, \end{cases} \end{aligned} \tag{3.6}$$

where C_u is expected beam gain. In addition, the angular coverage of an arbitrary codeword

in a level should cover the spatial ranges of several codewords in the next level, namely,

$$\Psi_{u,i} = \bigcup_{i'=ai-1}^{ai} \Psi_{u+1,i'},\ 1 \le i \le I_u,\ 1 \le u \le U-1, \tag{3.7}$$

where a is the number of corresponding codewords in the subsequent level and satisfies $I_{u+1} = aI_u, 1 \le u \le U-1$. Compared with the conventional codebooks in [41, 44, 87], which are based on equally-spaced spatial frequency φ in $[-\pi, \pi)$, the proposed time-delay codebook is directly built on physical angles, for which the associated spatial frequencies are not evenly divided and have different ranges for different frequencies within the bandwidth.

3.2.2 Multi-Resolution Codebook Design

Given the time-delay codebook structure, in this subsection, we will focus on the multi-resolution codeboook design based on the time delay set. Specifically, for any codeword $\mathbf{q}$, we denote $\mathbf{q} = [\mathbf{q}_1^T, \mathbf{q}_2^T, ..., \mathbf{q}_K^T]^T$ with $q_{k,n}$ being the n-th element of $\mathbf{q}_k$ such that $q_{k,n} = w_{k,n} f_k, 1 \le k \le K, 1 \le n \le N$.

3.2.2.1 Codebook with Beam Adaptation

We will first design the codebook based on physical beam directions of subarrays. For the array-of-subarrays structure, the beam generated by the AP with hybrid beamforming is given by

$$\begin{aligned} \mathbf{a}^*(KN, \phi)\mathbf{q} &= \sum_{k=1}^{K}\sum_{n=1}^{N} q_{k,n} e^{-j[(k-1)N+n-1]\frac{2\pi r}{\lambda}\sin\phi} \\ &= \sum_{k=1}^{K} f_k e^{-j(k-1)N\frac{2\pi r}{\lambda}\sin\phi} A_k(\phi), \end{aligned} \tag{3.8}$$

where $A_k(\phi) = \sum_{n=1}^{N} w_{k,n} e^{-j(n-1)\frac{2\pi r}{\lambda}\sin\phi}$ is the array factor of subarray k. From (3.8), the effective beam pattern of the entire antenna array is a combination of the beams generated by subarrays. As the digital baseband offers extra degree of freedom along with the analog beamforming gain, subarrays can be leveraged for joint design. For example, if $w_{k,n} = \frac{1}{\sqrt{N}}$ and $f_k = \frac{1}{\sqrt{K}}$, the whole antenna array will form a beam at broadside, offering K times

beam gain with narrow beamwidth compared to the beam generated by one subarray only. If $w_{k,n} = \frac{1}{\sqrt{N}}$ and $\mathbf{f}$ has the form of the matched filter, i.e., $f_k = \frac{1}{\sqrt{K}} e^{j(k-1)N\frac{2\pi r}{\lambda}\sin\phi_0}$, the resulting beam will achieve K times beam gain at physical direction ϕ_0 and the beamwidth will be broadened compared to the original beam generated by one subarray. Therefore, with proper design of $\mathbf{W}$ and $\mathbf{f}$, beams can be adjusted and refined through subarray coordination.

Since the time-delay codebook has unequally-spaced spatial frequency, dynamic subarray coordination and hybrid processing will be exploited for beam adaptation. For an N-element subarray with half-wavelength antenna spacing, the half-power beamwidth, $\frac{1.772\pi}{N}$, corresponds to $\frac{1.772}{N\cos\phi}$ at direction ϕ in the angular space [88]. To cover the desired angular range of $\Psi_{u,i}$, the required number of subarrays is roughly given by

$$Z_{u,i} = \left\lceil \frac{\frac{\pi}{I_u}}{\frac{1.772}{N\cos\phi^c_{u,i}}} \right\rceil = \left\lceil \frac{\pi N\cos\phi^c_{u,i}}{1.772 I_u} \right\rceil, \quad 1 \le i \le I_u,\ 1 \le u \le U, \tag{3.9}$$

where $\phi^c_{u,i}$ is the central angle of $\Psi_{u,i}$ with $\phi^c_{u,i} = -\frac{\pi}{2} + \frac{2i-1}{2I_u}\pi$ and $\lceil\cdot\rceil$ denotes the ceiling function. Hence, a group of $Z_{u,i}$ subarrays can cooperate to produce the desired beam pattern of the i-th codeword in the u-th level. Denote $\tilde{\phi}^z_{u,i}$ as the expected beam direction for the z-th subarray with

$$\tilde{\phi}^z_{u,i} = -\frac{\pi}{2} + \frac{i-1}{I_u}\pi + \frac{2z-1}{2Z_{u,i}I_u}\pi, \quad 1 \le z \le Z_{u,i}, 1 \le i \le I_u, 1 \le u \le U, \tag{3.10}$$

then, the associated physical beamforming direction for the z-th subarray can be obtained from the time-delay set, where the time-related angle satisfies

$$\hat{\phi}^z_{u,i} = \underset{t(\hat{\phi})\in\Phi_t}{\arg\min} \left|\hat{\phi} - \tilde{\phi}^z_{u,i}\right|^2, \quad 1 \le z \le Z_{u,i}, 1 \le i \le I_u,\ 1 \le u \le U. \tag{3.11}$$

Accordingly, an $NZ_{u,i}\times 1$ analog beamforming vector for the $Z_{u,i}$ subarrays can be designed

with the form of array steering vector as[5]

$$\hat{\mathbf{w}}_{u,i} = \frac{1}{\sqrt{N}}\Big[\mathbf{a}^T(N, \hat{\phi}^1_{u,i}), \mathbf{a}^T(N, \hat{\phi}^2_{u,i}), ..., \mathbf{a}^T(N, \hat{\phi}^{Z_{u,i}}_{u,i})\Big]^T. \tag{3.12}$$

Furthermore, every $Z_{u,i}$ consecutive subarrays are combined to virtually generate $\lceil \frac{K}{Z_{u,i}} \rceil$ same basic beam patterns for beam enhancement [64], which can be expressed as

$$\tilde{\mathbf{w}}_{u,i} = \Big[\underbrace{\hat{\mathbf{w}}^T_{u,i}, ..., \hat{\mathbf{w}}^T_{u,i}}_{\lceil \frac{K}{Z_{u,i}} \rceil}\Big]^T. \tag{3.13}$$

Then, the associated analog beamforming of the i-th codeword in the u-th level, $\mathbf{W}_{u,i}$, can be obtained through the diagonalization of the first KN elements of $\tilde{\mathbf{w}}_{u,i}$ as

$$\begin{aligned}\mathbf{W}_{u,i}[(k-1)N+n, k] &= \tilde{\mathbf{w}}_{u,i}[(k-1)N+n], \\ &1 \le n \le N,\ 1 \le k \le K.\end{aligned} \tag{3.14}$$

To design the digital beamforming, $\mathbf{f}_{u,i}$, we consider the quantized method as in [44] to evaluate the whole angular space. Hence, according to (3.6), $\mathbf{f}_{u,i}$ should satisfy

$$\mathbf{A}^*_D \mathbf{W}_{u,i} \mathbf{f}_{u,i} = \sqrt{C_u}\mathbf{g}_{u,i}, \tag{3.15}$$

where $\mathbf{A}_D = [\mathbf{a}(KN, \phi^D_1), \mathbf{a}(KN, \phi^D_2), ..., \mathbf{a}(KN, \phi^D_L)]$ is a $KN \times L$ matrix representing an over-complete dictionary with ϕ^D_l being the sampling angle and $L > KN$ being the resolution. And, $\mathbf{g}_{u,i}$ is an $L \times 1$ vector with

$$\mathbf{g}_{u,i}[l] = \begin{cases} 1, & \phi^D_l \in \Psi_{u,i}, \\ 0, & \text{otherwise.} \end{cases} \tag{3.16}$$

In particular, we denote $\tilde{\mathbf{A}}_{u,i} \triangleq \mathbf{A}^*_D \mathbf{W}_{u,i}$. Thus, the approximate solution of $\mathbf{f}_{u,i}$ in (3.15) can be obtained by pseudo-inverse as

$$\mathbf{f}_{u,i} = \frac{\tilde{\mathbf{f}}_{u,i}}{||\tilde{\mathbf{f}}_{u,i}||} \tag{3.17}$$

[5]Note that all the corresponding time delays of the array steering vectors are in the time-delay set, Φ_t, as mentioned in the previous subsection.

Table 3.1 Time-Delay Codebook with Beam Adaptation

Algorithm 3.1 Codebook Generation with Beam Adaptation

Initialize the number of codebook levels, U, and the number of the codewords in the u-th level, I_u.
Initialize the time-delay set, Φ_t, and the over-complete dictionary, $\mathbf{A}_D$.
for $u = 1 : U$ **do**
  for $i = 1 : I_u$ **do**
    Obtain the required number of subarrays, $Z_{u,i}$, as in (3.9) for establishing the basic beam pattern.
    Search the time-delay set, Φ_t, to find the best corresponding beamforming directions for the $Z_{u,i}$ subarrays as in (3.11).
    Obtain the analog beamforming matrix, $\mathbf{W}_{u,i}$, through beam enhancement as in (3.14).
    Obtain the digital beamforming vector, $\mathbf{f}_{u,i}$, as in (3.17).
    Obtain the time-delay codebook as $\mathbf{q}_{u,i} = \mathbf{W}_{u,i}\mathbf{f}_{u,i}$.
  end for
end for

with

$$\tilde{\mathbf{f}}_{u,i} = (\tilde{\mathbf{A}}_{u,i}^{*}\tilde{\mathbf{A}}_{u,i})^{-1}\tilde{\mathbf{A}}_{u,i}^{*}\mathbf{g}_{u,i}. \tag{3.18}$$

Then, the codebook can be obtained as $\mathbf{q}_{u,i} = \mathbf{W}_{u,i}\mathbf{f}_{u,i}$.

In brief, the time-delay codebook generation with beam adaptation is outlined in Algorithm 3.1. It should be noted that the approximate solution of $\mathbf{W}_{u,i}$ in (3.14) and $\mathbf{f}_{u,i}$ in (3.17) does not provide the exact codebook given in (3.6). Thus, the resulting beam gains of different codewords may be different, which can be denoted by $C_{u,i} = \frac{1}{\|\mathbf{f}_{u,i}\|^2}$. Also, the beam gain of a codeword may not be uniform over the desired angular range.

3.2.2.2 Codebook with Dynamic Approximation

For the time-delay codebook with beam adaptation, codewords are built on adaptively-combined physical beam directions of subarrays. To further exploit the cooperation among subarrays, we will seek the codebook design with dynamic approximation. In particular,

from (3.15), the expected i-th codeword in the u-th level can be expressed as

$$\tilde{\mathbf{q}}_{u,i} = \frac{(\mathbf{A}_D\mathbf{A}_D^*)^{-1}\mathbf{A}_D\mathbf{g}_{u,i}}{\left\|(\mathbf{A}_D\mathbf{A}_D^*)^{-1}\mathbf{A}_D\mathbf{g}_{u,i}\right\|}. \tag{3.19}$$

Accordingly, we aim to find the codeword, $\mathbf{q}^\star_{u,i} = \mathbf{W}^\star_{u,i}\mathbf{f}^\star_{u,i}$, so that

$$\mathbf{q}^\star_{u,i} = \arg\min \|\tilde{\mathbf{q}}_{u,i} - \mathbf{q}_{u,i}\|^2. \tag{3.20}$$

Specifically, for any codeword $\mathbf{q}$,

$$\begin{aligned}
\|\tilde{\mathbf{q}} - \mathbf{q}\|^2 &= \sum_{k=1}^{K} \|\tilde{\mathbf{q}}_k - \mathbf{q}_k\|^2 \\
&= \sum_{k=1}^{K} (\tilde{\mathbf{q}}_k - \mathbf{w}_k f_k)^*(\tilde{\mathbf{q}}_k - \mathbf{w}_k f_k) \\
&= \sum_{k=1}^{K} \|\tilde{\mathbf{q}}_k\|^2 + \|\mathbf{w}_k f_k\|^2 - 2\,\mathrm{Re}(\tilde{\mathbf{q}}_k^*\mathbf{w}_k f_k) \\
&= 2 - 2\sum_{k=1}^{K} \mathrm{Re}(\tilde{\mathbf{q}}_k^*\mathbf{w}_k f_k).
\end{aligned} \tag{3.21}$$

Thus, the optimization problem (3.20) is equivalent to

$$\max_{\mathbf{W},\mathbf{f}} \sum_{k=1}^{K} \mathrm{Re}(\tilde{\mathbf{q}}_k^*\mathbf{w}_k f_k), \tag{3.22}$$

namely,

$$\max_{\mathbf{w}_k, f_k} \mathrm{Re}(\tilde{\mathbf{q}}_k^*\mathbf{w}_k f_k), \qquad \forall 1 \le k \le K. \tag{3.23}$$

With regard to (3.23), the optimal digital beamforming should satisfy

$$\mathbf{f}^\star = \frac{\mathbf{f}}{\|\mathbf{f}\|} \tag{3.24}$$

with

$$f_k = \mathbf{w}_k^*\tilde{\mathbf{q}}_k. \tag{3.25}$$

To obtain the analog beamforming matrix, $\mathbf{W}^\star$, the associated true time delays should be selected from the time-delay set, Φ_t, such that

$$w^\star_{k,n} = \frac{1}{\sqrt{N}} e^{j\frac{2\pi c}{\lambda} t^\star_{k,n}(\hat{\phi})}, \qquad 1 \le n \le N,\ 1 \le k \le K, \tag{3.26}$$

Table 3.2 Time-Delay Codebook with Dynamic Approximation

Algorithm 3.2 Codebook Generation with Dynamic Approximation

1: **Initialize** the number of codebook levels, U, and the number of the codewords in the u-th level, I_u.
2: **Initialize** the time-delay set, Φ_t, and the over-complete dictionary, $\mathbf{A}_D$.
3: **for** $u = 1 : U$ **do**
4: **for** $i = 1 : I_u$ **do**
5: Obtain the expected codeword, $\tilde{\mathbf{q}}_{u,i}$, as in (3.26).
6: Search the time-delay set, Φ_t, to find the best time delays for the entire antenna array and obtain the analog beamforming matrix, $\mathbf{W}_{u,i}$ as in (3.26).
7: Obtain the digital beamforming, $\mathbf{f}_{u,i}$, as in (3.24).
8: Obtain the time-delay codebook as $\mathbf{q}_{u,i} = \mathbf{W}_{u,i}\mathbf{f}_{u,i}$.
9: **end for**
10: **end for**

where

$$t^{\star}_{k,n}(\hat{\phi}) = \underset{t(\hat{\phi})\in\Phi_t}{\arg\min} \left| t(\hat{\phi}) - \tau(\tilde{q}_{k,n}) \right|^2 \tag{3.27}$$

with $\tau(x)$ being the associated time delay of x that can be calculated from the time-related angle in (3.3) as

$$\tau(x) = \frac{\lambda}{2\pi c} \angle(x). \tag{3.28}$$

In (3.28), $\angle(\cdot)$ denotes the associated phase. It is noteworthy that, for dynamic approximation, the selected time delays from the time-delay set may not have same time-related angles. In specific, the codebook generation with dynamic approximation is summarized in Algorithm 3.2.

In summary, the proposed time-delay codebooks with subarray coordination take full advantage of the antennas in the mmWave and THz system so that no subarray is idle. Thus, the whole antenna gain is exploited and the beam gain could be effectively increased. Compared with random spatial sampling based on compressive sensing, where training signals may be corrupted in noise due to significant power dissipation over mmWave or THz channels, more energy can be focused on specific directions using the proposed codebooks for beamforming training. Then, the effectiveness of channel measurements will be improved,

especially in low SNR conditions.

3.3 Low-Complexity Implementation

For the mmWave and THz system in Fig. 3.1, the time-delay phase shifters scale with the antennas. As performing large-dimension true time delays may pose an extra burden on circuit circuit size and the associated design [32, 33], we consider a low-complexity implementation in this section.

3.3.1 Low-Complexity System Implementation

To reduce the number of time-delay phase shifters used in the mmWave and THz system, a low-complexity system implementation is given in Fig. 3.2. In particular, for each subarray, a group of conventional pure phase shifters are equipped, which are assumed to have a constant phase shift across the large bandwidth.[6] Distinctively, a time-delay phase shifter is inserted in the signal path between the RF chain and the subarray. Thus, the shared time-delay phase shifter of a subarray can partially compensate for the frequency-dependent phase deviation over the large bandwidth. Since the time-delay components are greatly reduced, the system in Fig. 3.2 could help to effectively reduce the circuit size and provide a performance-and-complexity tradeoff. Similar structures can also be implemented at the user side by deploying one shared time-delay phase shifter. Specifically, the pure phase shifters are assumed to have B-bit quantized phases, i.e., $\Theta = \{\psi | \psi = \frac{2\pi b}{2^B},\ b = 0, 1, ..., 2^B - 1\}$.

3.3.2 Modification on Time-Delay Codebooks

Given the low-complexity system implementation in Fig. 3.2, modifications on the time-delay codebooks are needed for beamforming training. Specifically, for any codeword $\mathbf{q}$ in the low-complexity system, we denote $t_k(\hat{\phi})$ as the true time delay and

$$\bar{\mathbf{w}}_k = \frac{1}{\sqrt{N}}[e^{j\psi_{k,1}}, e^{j\psi_{k,2}}, ..., e^{j\psi_{k,N}}]^T \tag{3.29}$$

[6]Note that the phase shifters are designed at the central frequency and random phase deviations across the large bandwidth are neglected here.

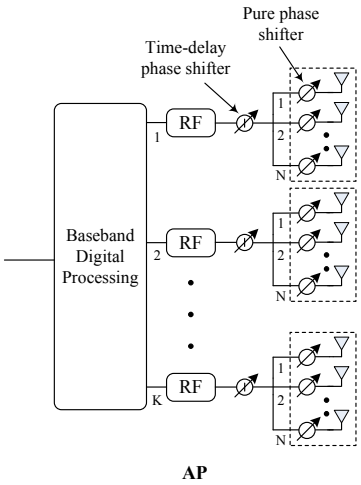

Fig. 3.2 A low-complexity implementation of the mmWave and THz system.

as the shifted phases of the pure phase shifters for the k-th subarray.

3.3.2.1 Modification for Codebook with Beam Adaptation

To minimize the shifted phases of the pure phase shifters and ensure sufficient time delays, the true time delays of the time-delay phase shifters should be designed first. In regard to the analog beamforming of the codebook with beam adaptation, the true time delay of the k-th subarray in the low-complexity system, $t_k^\star(\hat{\phi})$, can be obtained by averaging the associated time delays given in (3.14) over the entire subarray, i.e.,

$$t_k^\star(\hat{\phi}) = \underset{t(\hat{\phi})\in\Phi_t}{\arg\min} \left| t(\hat{\phi}) - \frac{1}{N}\sum_{n=1}^{N} \tau(w_{k,n}) \right|^2. \tag{3.30}$$

Then, $\bar{\mathbf{w}}_k$ can be selected from the quantized phase set, Θ, so that

$$\bar{\mathbf{w}}_k^\star = \arg\min \left\| \mathbf{w}_k - \bar{\mathbf{w}}_k e^{j\frac{2\pi c}{\lambda} t_k^\star(\hat{\phi})} \right\|^2, \qquad 1 \le k \le K, \tag{3.31}$$

namely,

$$\psi_{k,n}^\star = \underset{\theta\in\Theta}{\arg\min} \left| \psi + \frac{2\pi c}{\lambda} t_k^\star(\hat{\phi}) - \angle(w_{k,n}) \right|^2, \quad 1 \le n \le N,\ 1 \le k \le K, \tag{3.32}$$

Accordingly, with $\mathbf{w}_k^\star = \bar{\mathbf{w}}_k^\star e^{j\frac{2\pi c}{\lambda} t_k^\star(\hat{\phi})}$, the digital beamforming, $\mathbf{f}^\star$, can be constructed as (3.17).

3.3.2.2 *Modification for Codebook with Dynamic Approximation*

Similarly, for the time-delay codebook with dynamic approximation in the low-complexity system, the true time delay of the k-th subarray for any codeword $\mathbf{q}$ can be estimated by

$$t_k^\star(\hat{\phi}) = \arg\min_{t(\hat{\phi})\in\Phi_t} \left| t(\hat{\phi}) - \frac{1}{N}\sum_{n=1}^{N} \tau(\tilde{q}_{k,n}) \right|^2, \tag{3.33}$$

where $\tilde{\mathbf{q}}_k$ is defined in (3.26). Consequently, $\bar{\mathbf{w}}_k$ can be designed as

$$\bar{\mathbf{w}}_k^\star = \arg\min \left\| e^{j\angle(\tilde{\mathbf{q}}_k)} - \bar{\mathbf{w}}_k e^{j\frac{2\pi c}{\lambda} t_k^\star(\hat{\phi})} \right\|^2, \qquad 1 \le k \le K, \tag{3.34}$$

i.e.,

$$\theta_{k,n}^\star = \arg\min_{\theta\in\Theta} \left| \theta + \frac{2\pi c}{\lambda} t_k^\star(\hat{\phi}) - \angle(\tilde{q}_{k,n}) \right|^2, \quad 1 \le n \le N,\ 1 \le k \le K. \tag{3.35}$$

Then, given $\mathbf{w}_k^\star = \bar{\mathbf{w}}_k^\star e^{j\frac{2\pi c}{\lambda} t_k^\star(\hat{\phi})}$, the digital beamforming, $\mathbf{f}^\star$, can be obtained as (3.24).

In summary, for the low-complexity system implementation in Fig. 3.2, part of the time-delay phase shifters are replaced by pure phase shifters. As a result, the number of time-delay phase shifters is greatly reduced, which would simplify circuit design. However, as the pure phase shifters cannot effectively support beamforming over large bandwidth, the robustness of the modified time-delay codebooks will be degraded.

3.4 Hierarchical Beamforming Training

Given the multi-resolution time-delay codebooks, in this section, we will develop a hierarchical beamforming training strategy to extract the dominant information of mmWave and THz channels for multiple users. In order to reduce the overhead of one-by-one training, which grows with the number of users, simultaneous training will be designed. Without loss of generality, we assume J users are scheduled for concurrent beamforming training. Since the antenna number of any user j is much smaller than that of the AP, a general beamsteering codebook with only one level is assumed to be used, where the number of the codewords is equivalent to the number of antennas, M_j.

For beamforming training using the i-th codeword in the u-th level at the AP, the received signal at user j with the m_j-th codeword can be expressed as

$$y^j_{u,i,m_j} = \sqrt{P_s}\mathbf{v}^{j*}_{m_j}\mathbf{H}_j\mathbf{q}_{u,i} + \mathbf{v}^{j*}_{m_j}\mathbf{n}_j, \quad 1 \le u \le U,\ 1 \le i \le I_u,\ 1 \le m_j \le M_j. \tag{3.36}$$

Then, the multiuser hierarchical beamforming training strategy can be developed based on the normalized received signal power, i.e., $\frac{|y^j_{u,i,m_j}|^2}{C_{u,i}M_j}$.[7] In particular, the beamforming training is divided into two stages, an initial setup stage and a hierarchial searching stage.

1) Initial Setup Stage: The initial setup stage is analogous to the sector level sweeping (SLS) procedure in IEEE 802.11ad [37]. However, different from the SLS in IEEE 802.11ad, omni-directional beam cannot be used at initial setup since it hardly provides sufficient gain to compensate for the severe path loss in the higher-mmWave and THz bands. Consequently, the first level of the codebook should have several codewords associated with different spatial sectors and scanning for initial setup should be carried out at both the AP and the users. As defined in IEEE 802.11ad, the AP has fixed sweeping time for each sector, within which all users should concurrently perform individual codebook scanning based on the broadcasted signal. Normally, the training is accomplished by exhaustive search and each codeword is assigned equal scanning time by the user. As a result, to finish one round of searching, each codeword has limited scanning time, which may influence the accuracy of the received signal. Considering the sparse nature and the LOS-dominant characteristics of the mmWave and THz channels, the training strategy at the user side can be improved by reducing the number of scanned codewords for a transmit sector. Specifically, we define a threshold for the received signal measurement at user j as

$$\Upsilon_j = \rho P_s L_{PL}, \tag{3.37}$$

where L_{PL} is the LOS path loss defined in (2.6) and ρ is a scale factor.[8] For a transmit sector

[7] Note that the received signal power is normalized to reduce the influence of the beam gains of different codewords.

[8] Considering the over 5 dB gap between the LOS and the NLOS path gains, ρ can be designed as $0.3 < \rho \le 1$.

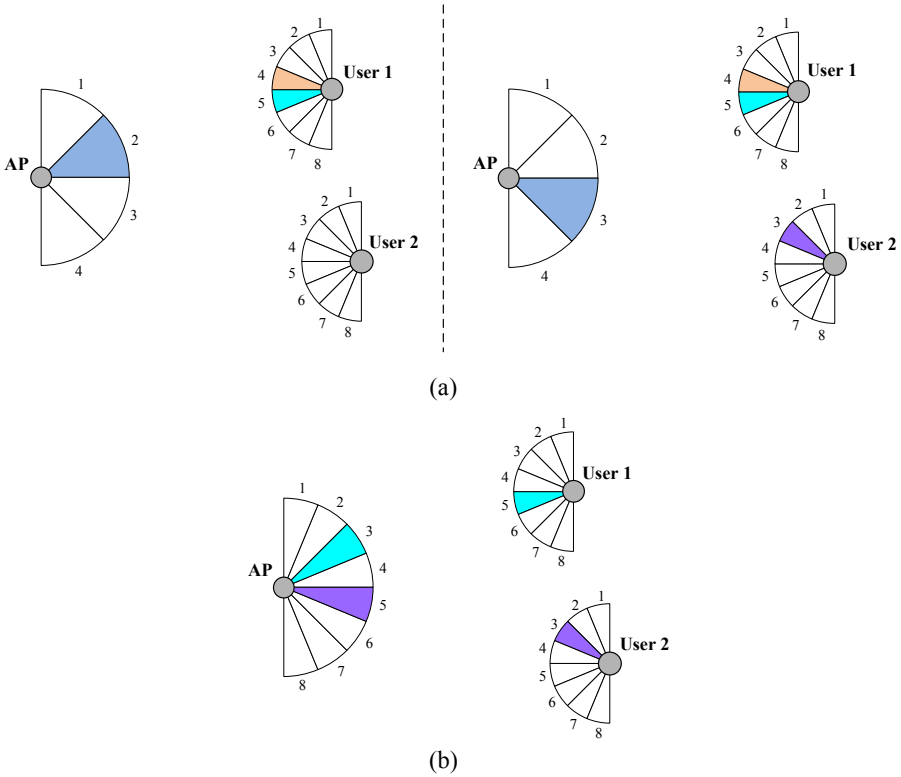

Fig. 3.3 An example of two-user hierarchical beamforming training: (a) initial setup stage; (b) hierarchical searching stage.

sweeping at the AP, if the normalized received signal power of some codewords at user j exceeds the threshold, Υ_j, only these codewords will be scanned for the next transmit sector. Otherwise, if no normalized received signal power exceeds the threshold, all the scanned codewords for current sector will be tested for the next transmit sector. After one round of transmit sector sweeping, the beam pair with the maximal normalized received signal power will be selected.

2) Hierarchical Searching Stage: Given the candidate beam information from all users, the AP selects the corresponding codewords in the subsequent level of the codebook for hierarchical searching, which is similar to the beam refinement procedure (BRP) in IEEE 802.11ad [37]. In this stage, by fixing the best received beamforming codewords at the users, the chosen transmit codewords obtained from the previous training are tested for all users step by step. Finally, the best transmit and receive codewords associated with the the dominant path will be achieved for all users.

The overall multiuser hierarchical beamforming training is summarized in Algorithm 3.3. Specifically, an example of two-user hierarchical beamforming training is shown in Fig. 3.3. As shown in Fig. 3.3(a), in the initial setup stage, user 1 and user 2 simultaneously scan their individual codebooks during the sector-2 sweeping of the AP. The normalized received signal power of codewords 4 and 5 for user 1 exceeds the threshold while no codeword satisfies the criterion for user 2. Then, during the sector-3 sweeping of the AP, user 1 only scans codewords 4 and 5 while user 2 keeps scanning all the codewords. The training continues until all the sectors of the AP are scanned and codewords 5 and 3 are selected for users 1 and 2, respectively, where the corresponding sectors of the AP are sectors 2 and 3. In the hierarchical searching stage shown in Fig. 3.3(b), users 1 and 2 adopt the codewords obtained from the initial setup stage and the AP searches the subsequent level of the codebook, i.e., sectors 3-6 in Fig. 3.3(b). Finally, the training process ends with the best transmit sectors 3 and 5 are found for users 1 and 2, respectively.

In general, the total number of the scanned codewords for any user j in the initial set-up stage is $\sum_{i=1}^{I_1} |\mathcal{M}_{i,j}|$, which is smaller than that of the exhaustive search, $I_1 M_j$. Thus, the effective scanning time of each codeword will be increased, which will help improve the scanning accuracy. Furthermore, compared with the conventional one-by-one independent training, whose time requirement is $JI_1T_{SLS} + aJ(U-1)T_{BRP}$ with T_{SLS} being the corresponding SLS frame time for one transmit sector and T_{BRP} being the BRP frame time,[9] the multiuser simultaneous beamforming training, with at most $I_1T_{SLS} + aJ(U-1)T_{BRP}$ time complexity, could efficiently reduce the measurement overhead.

3.5 Simulation Results

In this section, simulation results are provided to evaluate the performance of the hierarchical beamforming training with the multi-resolution time-delay codebooks for the mmWave and THz system.

[9] In IEEE 802.11ad, T_{SLS} is generally larger than T_{BRP} [37].

Table 3.3 Multiuser Hierarchical Beamforming Training for mmWave and THz Communications

Algorithm 3.3 Multiuser Hierarchical Beamforming Training

Initialize the multi-resolution time-delay codebook for the AP, $\mathcal{Q}$, the number of the codebook levels, U, and the number of first-level codewords, I_1.
Initialize the codebook for user j, $\mathcal{V}_j$.
Initialize $u = 1$ and $\mathcal{M}_{1,j} = \{1, 2, ..., M_j\}$.
while $u \leq U$ **do**
  if $u = 1$ **then**
    (Initial setup stage)
    for $i = 1 : I_1$ **do**
      All users simultaneously scan individual codebook, $\mathcal{V}_j$, to obtain $y^j_{1,i,m_j},\ m_j \in \mathcal{M}_{i,j}$.
      if $i < I_1$ **then**
        Update $\mathcal{M}_{i+1,j} = \{m_j \Big| \frac{\left|y^j_{1,i,m_j}\right|^2}{C_{1,i}M_j} > \Upsilon_j,\ m_j \in \mathcal{M}_{i,j}\}$.
        if $\mathcal{M}_{i+1,j} = \varnothing$ **then**
          Update $\mathcal{M}_{i+1,j} = \mathcal{M}_{i,j}$.
        end if
      end if
    end for
    Obtain the candidate beam pair for user j as $(i^\star_j, m^\star_j) = \underset{1\leq i\leq I_1, m_j\in\mathcal{M}_j}{\arg\max} \frac{\left|y^j_{1,i,m_j}\right|^2}{C_{1,i}M_j}$.
  else
    (Hierarchical searching stage)
    Search $\mathcal{I}_u$ to obtain $i^\star_j = \underset{i\in\mathcal{I}_u}{\arg\max} \frac{\left|y^j_{u,i,m^\star_j}\right|^2}{C_{u,i}M_j}$.
  end if
  Update $u = u + 1$.
  Obtain $\mathcal{I}_u = \{ai^\star_1 - a + 1, ..., ai^\star_1, ai^\star_2 - a + 1, ..., ai^\star_2, ..., ai^\star_J - a + 1, ..., ai^\star_J\}$.
end while
Obtain the approximate AoD and AoA of the dominant path for user j, $-\frac{\pi}{2} + \frac{2i^\star_j - 1}{2I_U}\pi$ and $-\frac{\pi}{2} + \frac{2m^\star_j - 1}{2M_j}\pi$.

An indoor mmWave and THz system with three users is considered, where the operating frequency is 0.1 THz, i.e, 100 GHz. For simplicity, we assume there exist three first-order reflected rays and four second-order reflection components in our simulation as [48]. Specifically, for the mmWave and THz system, the number of RF chains is set as $K = 8$, the antenna elements in each subarray are $N = 8$, and the number of antennas for different

users is set as the same with $M = 8$. And, the codebook levels are set as $U = 4$, the number of the first-level codewords is set to be $I_1 = 8$ as restricted by the subarray structure, and the number of the corresponding codewords in the subsequent level is set as $a = 2$. The time-delay set, Φ_t, is set to have uniform $\frac{\pi}{64}$-spacing in time-related phases, and the pure phase shifters in the low-complexity implementation are set with $B = 6$. Moreover, the resolution of the over-complete dictionary is set as $L = 256$. The noise power, σ_j^2, is set as -75 dBm for all users.

As a benchmark, the codebook based on orthogonal matching pursuit (OMP) for the fully-connected structure in [44] is considered, where the pure phase shifters are used.

3.5.1 Beam Patterns of Time-Delay Codebooks

We will first study the beam patterns of the proposed time-delay codebooks.

Fig. 3.4 demonstrates the beam patterns of the second-level codewords for different multi-resolution codebooks. We can observe from Fig. 3.4 that, the proposed time-delay codebooks can effectively cover the angular space and satisfy the criteria in (3.4) and (3.6). However, there exist fluctuations for the codewords, and the beam gain becomes higher on endfire because the time-delay codebooks have unequally divided spatial frequencies and a smaller spatial frequency will lead to higher beam gain. Also, we can see that the codebook with dynamic approximation has more similar beam gain across the beam coverage of a codeword while the codebook with beam adaptation has a relatively higher peak beam gain of a codeword. More specifically, the codebook with OMP has the largest fluctuations in the beam gain of a codeword. In addition, the codebooks with low-complexity implementation only have minor variations compared with the original time-delay codebooks.

We compare the beam patterns of the codebooks at different frequencies in Fig. 3.5. Specifically, the deviation frequency, 102 GHz, is considered, and the last-level codeword of the codebook with beam direction around $\frac{3\pi}{16}$ is investigated. From Fig. 3.5, the codebook with beam adaptation has a limited effect of beam squint and is more robust over the large bandwidth compared to the codebook with dynamic approximation. On the other hand,

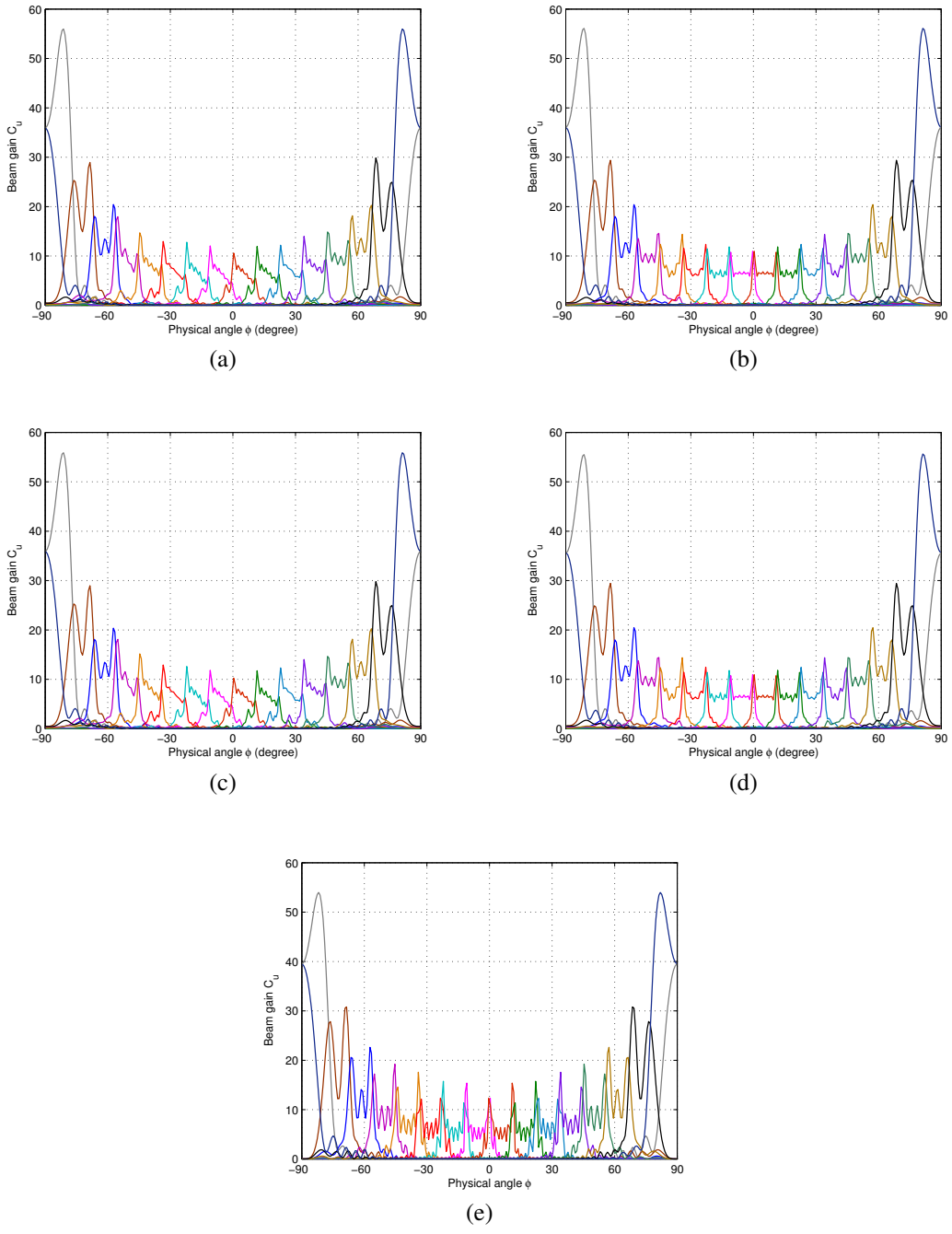

Fig. 3.4 Beam patterns of the second-level codewords for different multi-resolution codebooks: (a) codebook with beam adaptation; (b) codebook with dynamic approximation; (c) codebook with beam adaptation using low-complexity implementation; (d) codebook with dynamic approximation using low-complexity implementation; (e) codebook with OMP.

the codebook with OMP using pure phase shifters experiences the most severe effect of beam squint, where the beam gain at the expected beamforming direction significantly

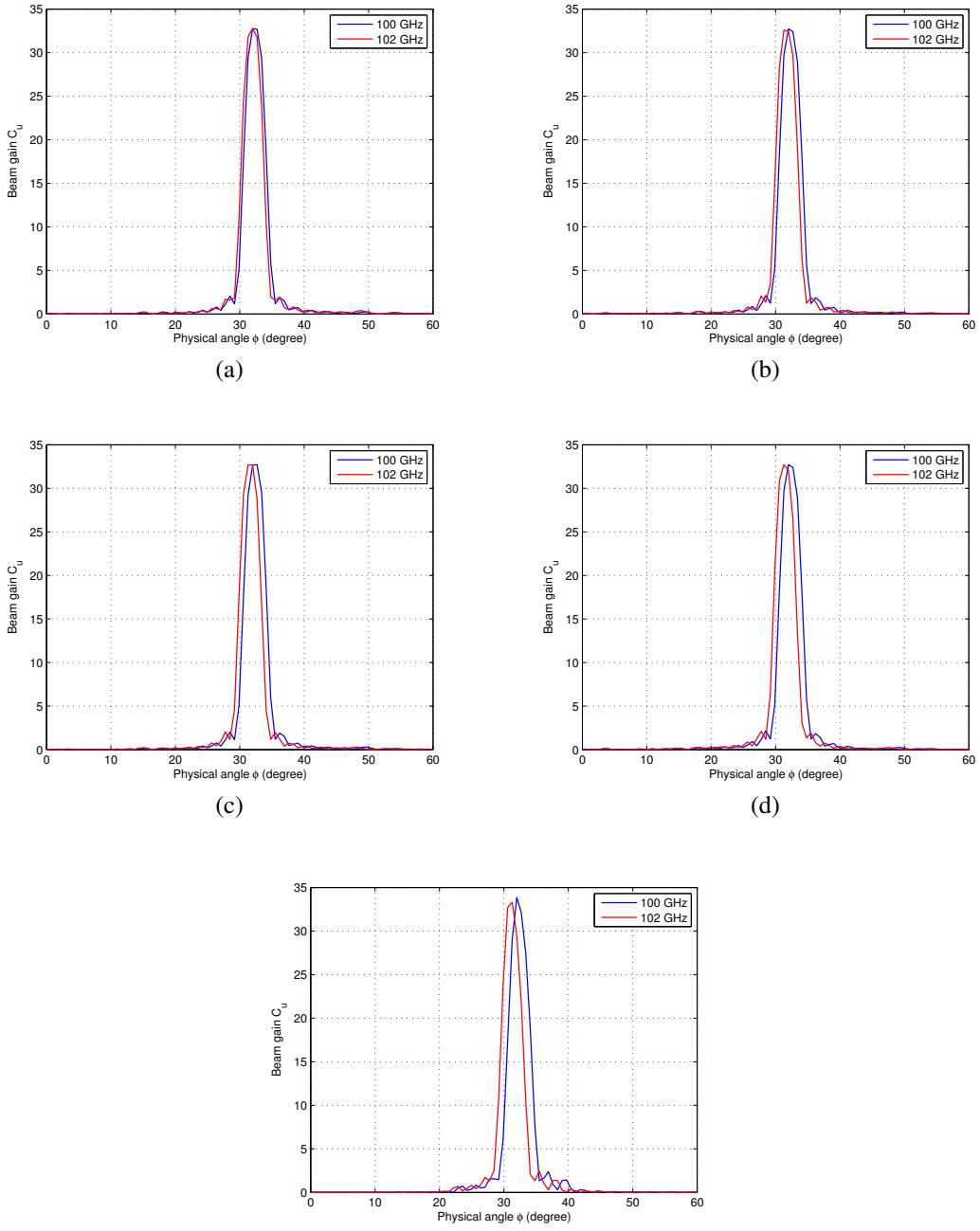

Fig. 3.5 Comparison of beam patterns for different codebooks at different frequencies: (a) codebook with beam adaptation; (b) codebook with dynamic approximation; (c) codebook with beam adaptation using low-complexity implementation; (d) codebook with dynamic approximation using low-complexity implementation; (e) codebook with OMP.

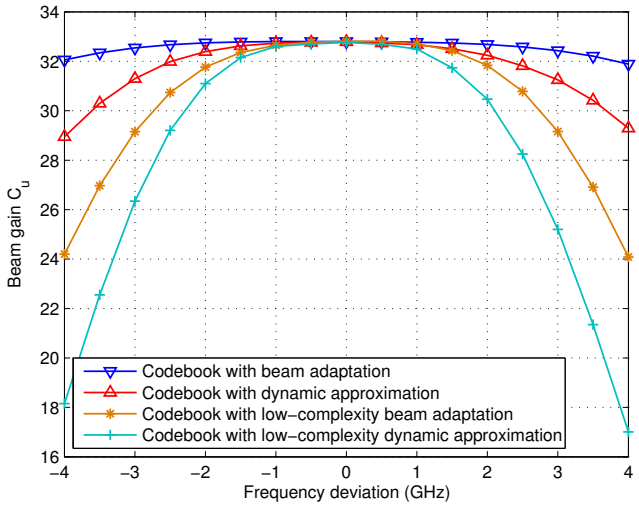

Fig. 3.6 The degradation of the beam gain versus the frequency deviation.

decreases as a result of frequency mismatch. Therefore, the use of time-delay phase shifters is necessary for mmWave and THz systems with large bandwidth to prevent performance degradation and improve system robustness. Furthermore, the degradation of the beam gain at $\frac{3\pi}{16}$ for the low-complexity implementation as a function of the frequency deviation is plotted in Fig. 3.6. We can see from Fig. 3.6 that, the performance degradation of the low-complexity implementation increases with the frequency deviation while it could provide a performance-and-complexity tradeoff within certain frequency range.

3.5.2 Beamforming Training Performance

In this subsection, we will evaluate the beamforming training performance using the multi-resolution time-delay codebooks. Specifically, the results are averaged over 10, 000 channel realizations.

We plot the the success rate and the overhead of the proposed multiuser hierarchical beamforming training with different codebooks as a function of the threshold ρ in Fig. 3.7. Here, the success rate is the ratio of the number of successful detection of the dominant AoD/AoA and the total number of training, and the overhead is defined as the averaged number of scanned codewords for one user. The training power is set as $P_s = 10$ dBm. In specific, the overhead of the exhaustive search based on the multi-resolution codebook

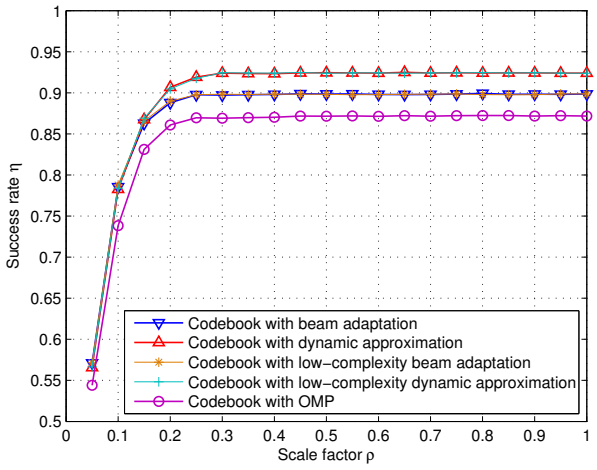

(a)

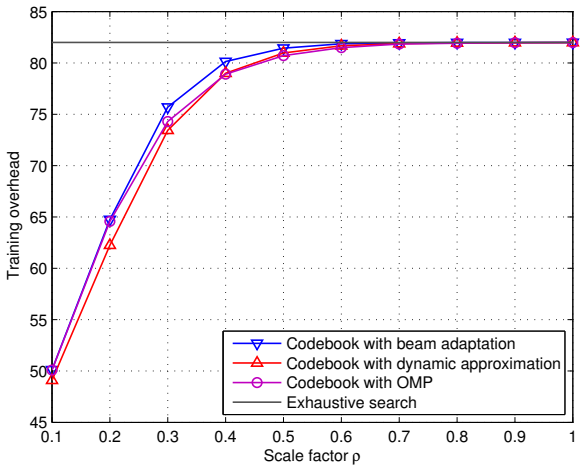

(b)

Fig. 3.7 Performance of the multiuser hierarchical beamforming training versus the scale factor ρ: (a) success rate; (b) training overhead.

is considered for comparison. As shown in Fig. 3.7(a), the success rates increase with ρ first and then approach the limit when $\rho > 0.3$, which verifies the analysis in Section V. On the other hand, from Fig. 3.7(b), the training overhead increases with ρ first and then becomes the same as that of the exhaustive search when $\rho \geq 0.7$. Therefore, for $0.3 < \rho < 0.7$, the proposed hierarchical beamforming training could effectively reduce the training overhead while providing guaranteed performance. Moreover, according to Fig. 3.7, both the proposed time-delay codebooks outperform the codebook with OMP as a

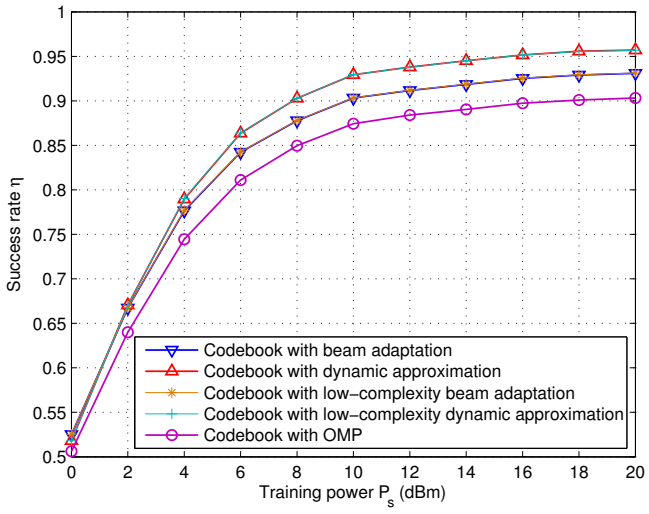

Fig. 3.8 Success rate of the multiuser hierarchical beamforming training with different codebooks under different training power.

result of smaller fluctuations in beam gain. And, the codebook with dynamic approximation has slightly better performance than the codebook with beam adaptation since it has more balanced beam gain. Also, the overhead of the beamforming training using the codebook with dynamic approximation is relatively smaller than those of other two codebooks. In addition, the low-complexity codebooks have almost the same performance as the original time-delay codebooks.

In Fig. 3.8, we plot the success rate of the multiuser hierarchical beamforming training with different codebooks under different training power. In particular, ρ is set as 0.4. As shown in Fig. 3.8, the success rates increase with the training power as expected and finally saturate. Similar to Fig. 3.7, both the proposed time-delay codebooks show advantages over the codebook with OMP, and the codebook with dynamic approximation performs slightly better than the codebook with beam adaptation.

In summary, according to the simulation results, the codebook with beam adaptation is more robust over the large bandwidth while the codebook with dynamic approximation achieve a higher success rate of beamforming training. The reason is that the codebook with beam adaptation is directly built on physical-angle-defined time delay. Thus, it could

capture the frequency-dependent phase shifts across the large bandwidth and ensure robustness. However, the codebook with dynamic approximation relies on the time-delay estimation at the central frequency. As a result, it will have better performance at the central frequency and less stability over the bandwidth.

3.6 Conclusions

This chapter has investigated mmWave and THz communication systems with multiple antenna subarrays. To support effective communications over large bandwidth, time-delay phase shifters have been adopted in system design. By capturing channel characteristics as well as circuit hardware, we have developed a hierarchical beamforming training strategy with reduced overhead to extract the dominant channel information for multiple users simultaneously. Specifically, two multi-resolution time-delay codebooks with beam adaptation and dynamic approximation have been designed through subarray coordination to enhance beamforming training. Also, a low-complexity system implementation is studied. A few important results have been obtained through simulation. First, the codebook with beam adaptation is more robust to beam squint over large bandwidth while the codebook with dynamic approximation offers more balanced beam gain across the beam coverage. Second, the low-complexity implementation could effectively provide a moderate solution for a performance-complexity tradeoff. Last but not least, the proposed multiuser hierarchical beamforming training strategy can efficiently reduce the training overhead with guaranteed performance.

CHAPTER 4

SINGLE-USER TRANSMISSION DESIGN AND ANALYSIS

With the hybrid beamforming strategies of the array-of-subarrays systems, we will further study the performance limits and optimized array design for single-user mmWave and THz communications in this chapter. First, a modified S-V model [89, 90] is proposed to capture the characteristics of the mmWave and THz channels. Second, by adopting hybrid beamforming, we analyze the ergodic capacity of the mmWave and THz system and obtain a capacity upper bound. Third, we investigate the effects of uncertainties in the phase shifters and analyze the resulting capacity degradation. Taking the uncertainty into account, we provide a guideline on designing antenna subarray size to ensure certain data rates at different communication distances.

The rest of this chapter is organized as follows. In Section 4.1, we briefly introduce the system model and present a modified statistical mmWave and THz channel model. Section 4.2 investigates the system performance limits with hybrid beamforming based on the statistical characteristics of mmWave and THz channels. In Section 4.3, we analyze the impact of uncertainty in the phase shifters and then provide a guideline on the subarray structure design accordingly. Numerical results are provided in Section 4.4 to evaluate the effectiveness of the system. Finally, we conclude this chapter in Section 4.5.

4.1 System Overview

In this section, we will present the single-user system model and statistical mmWave and THz channels.

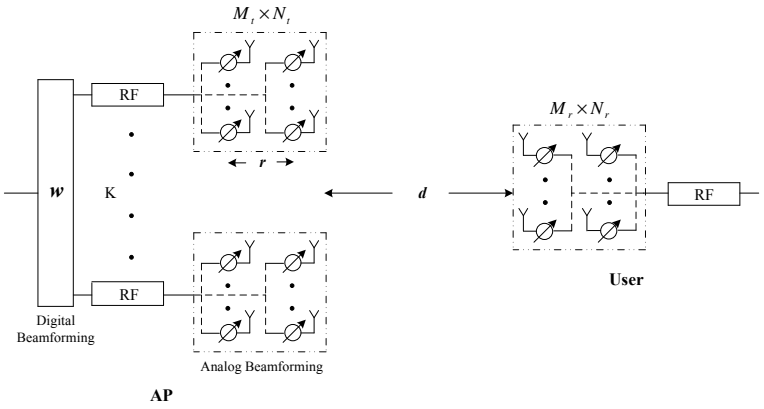

Fig. 4.1 The indoor single-user mmWave and THz system.

4.1.1 System Model

Similar to Fig. 3.1, an indoor single-user mmWave and THz system with the array-of-subarrays structure is shown in Fig. 4.1. Different from Chapter 2 and Chapter 3, (M,N)-element UPAs are adopted. Moreover, the distance between adjacent subarrays, e, is designed to be much larger than the antenna-element spacing, r, here. Thus, the NLOS paths of different subarrays experience independent scatterers, then, the spatial diversity can be further exploited. We further assume the distance between the AP and the user, d, is much larger than the adjacent subarray spacing so that the distance between the user and each subarray of the AP is approximately the same.

4.1.2 Statistical Millimeter-Wave and Terahertz Channel

To better capture the mmWave and THz channels in (2.5), the statistical characteristics will be explored in this subsection. In the higher-mmWave and THz bands, the S-V channel model [89, 90], which associates clustering phenomenon and stochastic AoD/AoA to each ray, exhibits a good match with the indoor measurement results [15, 16]. Therefore, we will modify the conventional S-V model for the mmWave and THz channels.

For the S-V model, the arrival paths are composed of many clusters, each of which consists of several rays. Without loss of generality, the arrival time of the first cluster is set as the reference time, i.e., $T_0 = 0$. The arrival time of the i-th cluster and the arrival time of the l-th ray in the i-th cluster are denoted as T_i and τ_{il}, respectively. Then, the arrival time

of each ray will be

$$t_{il} = T_i + \tau_{il}. \tag{4.1}$$

Therefore, the channel response for one antenna subarray within the time margin, T_s, can be written as [69]

$$\mathbf{H}_s(f,d) = \sum_{i=0}^{N_{clu}-1} \sum_{l=0}^{N^i_{ray}-1} \alpha_{il}(f,d) G_t(\phi^t_{il}, \theta^t_{il}) G_r(\phi^r_{il}, \theta^r_{il}) \mathbf{a}_r(M_r, N_r, \phi^r_{il}, \theta^r_{il}) \mathbf{a}^*_t(M_t, N_t, \phi^t_{il}, \theta^t_{il}), \tag{4.2}$$

where N_{clu} and N^i_{ray} are the numbers of clusters and rays in the i-th cluster, respectively. $\alpha_{il}(f,d) = |\alpha_{il}(f,d)|e^{j\psi_{il}}$ denotes the path gain of the arrival ray, where ψ_{il} is the associated independent phase. $\phi^t_{il}/\theta^t_{il}$ and $\phi^r_{il}/\theta^r_{il}$ refer to the azimuth/elevation angles of departure and arrival, respectively. $G_t(\phi^t_{il}, \theta^t_{il})$ and $G_r(\phi^r_{il}, \theta^r_{il})$ represent the transmit and receive antenna gains while vectors $\mathbf{a}_t(\phi^t_{il}, \theta^t_{il})$ and $\mathbf{a}_r(\phi^r_{il}, \theta^r_{il})$ are the associated array steering vectors at the transmit and receive sides, respectively.

4.1.2.1 Time of Arrival

For the S-V channel model, the time of arrival for each cluster is random and exponentially distributed conditioned on the time of arrival of the previous cluster. So is the ray arrival time within each cluster. As a result,

$$p(T_i|T_{i-1}) = \Lambda e^{-\Lambda(T_i - T_{i-1})}, \qquad T_i > T_{i-1}, \tag{4.3}$$

and

$$p(\tau_{il}|\tau_{i(l-1)}) = \lambda e^{-\lambda(\tau_{il} - \tau_{i(l-1)})}, \qquad \tau_{il} > \tau_{i(l-1)}, \tag{4.4}$$

where Λ denotes the cluster arrival rate accounting for the inter-cluster arrival time, and λ denotes the ray arrival rate within cluster accounting for the intra-cluster arrival time. Note that Λ and λ are frequency-dependent and sensitive to the indoor building materials. Generally, the rougher the wall surface is, the smaller the inter- and intra-cluster arrival rates are [15, 71]. For example, the arrival rates of the glass, a better reflecting material, are relatively larger, whereas that of the rough plaster, which is less reflective, are smaller [91]. Accordingly, the number of cluster arrivals and that of ray arrivals in each cluster form two

independent counting processes, which follow the Poisson processes with rates Λ and λ, respectively.

4.1.2.2 Path Gain

In the S-V channel model, the mean-square path gain of each ray follows a double exponential decay profile as [89]

$$\mathbb{E}[|\alpha_{il}(f,d)|^2] = \Psi_0(f,d)e^{-\frac{T_i}{\Gamma}}e^{-\frac{\tau_{il}}{\gamma}}, \tag{4.5}$$

where Γ and γ are the exponential decay factors of the cluster arrivals and ray arrivals, respectively. Note that Γ and γ are also frequency and wall-material dependent. Generally, Γ and γ increase with the roughness of the wall surface [15,71]. And, $\Psi_0(f,d)$ is the average power gain of the first component of the first cluster, thus,

$$\Psi_0(f,d) = L_{PL}(f,d) = \left(\frac{c}{4\pi f d}\right)^2 e^{-k_{abs}(f)d}. \tag{4.6}$$

4.1.2.3 AoD and AoA

We assume the departure/arrival time and angle are independent as in [90]. The total azimuth AoD/AoA of each ray, ϕ^t_{il}/ϕ^r_{il}, consists of the mean azimuth AoD/AoA for the clusters, Φ^t_i/Φ^r_i, and the azimuth AoD/AoA for the rays within clusters, $\varphi^t_{il}/\varphi^r_{il}$. Similarly, the total elevation angle of departure/arrival of each ray, $\theta^t_{il}/\theta^r_{il}$, consists of the mean elevation AoD/AoA for the clusters, Θ^t_i/Θ^r_i, and the elevation AoD/AoA for the rays within clusters, $\vartheta^t_{il}/\vartheta^r_{il}$. Thus,

$$\phi^t_{il} = \Phi^t_i + \varphi^t_{il}, \qquad \phi^r_{il} = \Phi^r_i + \varphi^r_{il}, \tag{4.7}$$

$$\theta^t_{il} = \Theta^t_i + \vartheta^t_{il}, \qquad \theta^r_{il} = \Theta^r_i + \vartheta^r_{il}, \tag{4.8}$$

where Φ^t_i/Φ^r_i and Θ^t_i/Θ^r_i follow uniform distributions on $(-\pi,\pi]$ and $[-\frac{\pi}{2},\frac{\pi}{2}]$, respectively. And, $\varphi^t_{il}/\varphi^r_{il}$ and $\vartheta^t_{il}/\vartheta^r_{il}$ follow a zero-mean second order Gaussian mixture model (GMM) [71]

$$GMM(x) = \frac{w_1}{\sqrt{2\pi}\sigma_1}e^{-\frac{x^2}{2\sigma_1^2}} + \frac{w_2}{\sqrt{2\pi}\sigma_2}e^{-\frac{x^2}{2\sigma_2^2}}, \tag{4.9}$$

where w_1 and w_2 are the associated second order GMM coefficients. It is worth mentioning that the GMM distributions are truncated and limited to the azimuth angular range $(-\pi, \pi]$ and the elevation angular range $[-\frac{\pi}{2}, \frac{\pi}{2}]$. Compared with the conventional S-V channel model, where AoD/AoA follow Laplacian distributions, the GMM model renders a more accurate approximation and higher angular resolution, especially when the angle is close to zero.

4.1.2.4 Antenna Gain

Different from Chapter 2 and Chapter 3, to achieve more directional antenna gains, ideal sector antennas are used. Accordingly, the antenna gain of the transmit antenna element can be given by [43]

$$G_t(\phi_{il}^t, \theta_{il}^t) = \begin{cases} \sqrt{G_t^0}, & \forall \phi_{il}^t \in [\phi_{min}^t, \phi_{max}^t], \forall \theta_{il}^t \in [\theta_{min}^t, \theta_{max}^t], \\ 0, & \text{otherwise}, \end{cases} \tag{4.10}$$

which means that the antenna gain is achieved when $\phi_{il}^t \in [\phi_{min}^t, \phi_{max}^t]$ and $\theta_{il}^t \in [\theta_{min}^t, \theta_{max}^t]$. The receive antenna gain $G_r(\phi_{il}^r, \theta_{il}^r)$ is defined similarly over azimuth sector $\phi_{il}^r \in [\phi_{min}^r, \phi_{max}^r]$ and elevation sector $\theta_{il}^r \in [\theta_{min}^r, \theta_{max}^r]$. Note that these sectors are usually small to ensure the antenna directivity.

4.2 System Performance with Hybrid Beamforming

Based on the modified S-V mmWave and THz channel model discussed in the previous section, we will study the hybrid beamforming and associated ergodic capacity for the single-user system.

4.2.1 Hybrid Beamforming and Ergodic Capacity

Similar to Chapter 2 and Chapter 3, in the RF domain, for a given target direction, (ϕ_0^t, θ_0^t) and (ϕ_0^r, θ_0^r), the analog beamforming is designed to have the same structure as the array steering vector. It should be noted that this direction is set as the same for different subarrays and it is within the antenna sector range, which may not be the LOS direction. Then,

we can describe the equivalent channel of one subarray from the baseband as

$$h_s(f,d) = \sum_{i=0}^{N_{clu}-1} \sum_{l=0}^{N_{ray}^i-1} \alpha_{il}(f,d) G_t(\phi_{il}^t, \theta_{il}^t) G_r(\phi_{il}^r, \theta_{il}^r) A_r^{eq}(\phi_{il}^r, \theta_{il}^r) A_t^{eq}(\phi_{il}^t, \theta_{il}^t), \tag{4.11}$$

where

$$A_t^{eq}(\phi,\theta) = \frac{1}{\sqrt{M_t N_t}} \frac{\sin[\frac{\pi r}{\lambda_c} M_t(\cos\phi\sin\theta - \cos\phi_0^t \sin\theta_0^t)]}{\sin[\frac{\pi r}{\lambda_c}(\cos\phi\sin\theta - \cos\phi_0^t\sin\theta_0^t)]} \frac{\sin[\frac{\pi r}{\lambda_c} N_t(\sin\phi\sin\theta - \sin\phi_0^t \sin\theta_0^t)]}{\sin[\frac{\pi r}{\lambda_c}(\sin\phi\sin\theta - \sin\phi_0^t\sin\theta_0^t)]} \tag{4.12}$$

and

$$A_r^{eq}(\phi,\theta) = \frac{1}{\sqrt{M_r N_r}} \frac{\sin[\frac{\pi r}{\lambda_c} M_r(\cos\phi\sin\theta - \cos\phi_0^r \sin\theta_0^r)]}{\sin[\frac{\pi r}{\lambda_c}(\cos\phi\sin\theta - \cos\phi_0^r\sin\theta_0^r)]} \frac{\sin[\frac{\pi r}{\lambda_c} N_r(\sin\phi\sin\theta - \sin\phi_0^r \sin\theta_0^r)]}{\sin[\frac{\pi r}{\lambda_c}(\sin\phi\sin\theta - \sin\phi_0^r\sin\theta_0^r)]} \tag{4.13}$$

are the array factors at the transmitter and receiver, respectively.

Based on the equivalent baseband channel, the channel between the user and the AP can be viewed as a multiple-input-single-output (MISO) channel, $\boldsymbol{h}^{eq}(f,d)$, with $h_k^{eq}(f,d) = h_s^{(k)}(f,d)$, where $1 \le k \le K$ is the antenna subarray index. Then, the maximal ratio transmission (MRT) can be adopted, thus, the optimal subarray-based digital beamformer is given by [92]

$$\mathbf{f}^{\dagger}(f,d) = \frac{\mathbf{h}^{eq}(f,d)}{\|\mathbf{h}^{eq}(f,d)\|}, \tag{4.14}$$

where $(\cdot)^{\dagger}$ denotes the conjugate.

If the channel is assumed to be flat-fading within a small bandwidth, B, centered around the frequency f, the ergodic capacity of the narrowband mmWave and THz system with

the hybrid beamforming can be written as

$$
\begin{aligned}
&\bar{C}(f,d) \\
&= \mathbb{E}[B\log_2(1+\frac{P}{N_0}\|\mathbf{h}^{eq}(f,d)\|^2)] = \mathbb{E}[B\log_2(1+\frac{P}{N_0}\sum_{k=1}^{K}|h_k^{eq}(f,d)|^2)] \\
&\leq B\log_2\left(1+\frac{P}{N_0}\sum_{k=1}^{K}\mathbb{E}[|h_k^{eq}(f,d)|^2]\right) \qquad (4.15) \\
&= B\log_2\left(1+\frac{KP}{N_0}\mathbb{E}\Big[\Big|\sum_{i=0}^{N_{clu}-1}\sum_{l=0}^{N_{ray}^i-1}\alpha_{il}(f,d)G_t(\phi_{il}^t,\theta_{il}^t)G_r(\phi_{il}^r,\theta_{il}^r)A_r^{eq}(\phi_{il}^r,\theta_{il}^r)A_t^{eq}(\phi_{il}^t,\theta_{il}^t)\Big|^2\Big]\right) \\
&\leq B\log_2\left(1+\frac{KP}{N_0}\mathbb{E}\Big[\sum_{i=0}^{N_{clu}-1}\sum_{l=0}^{N_{ray}^i-1}|\alpha_{il}(f,d)|^2\Big]\right. \\
&\quad \left.\times\mathbb{E}\Big[\sum_{i=0}^{N_{clu}-1}\sum_{l=0}^{N_{ray}^i-1}|G_t(\phi_{il}^t,\theta_{il}^t)G_r(\phi_{il}^r,\theta_{il}^r)A_r^{eq}(\phi_{il}^r,\theta_{il}^r)A_t^{eq}(\phi_{il}^t,\theta_{il}^t)|^2\Big]\right), \qquad (4.16)
\end{aligned}
$$

where P is the transmit power and N_0 is the noise power at the receiver. The inequality (4.15) is due to the *Jensen* inequality and the inequality (4.16) is due to the *Cauchy-Schwarz* inequality. Thus, the ergodic capacity of the indoor mmWave and THz system is upper bounded by (4.16). In what follows, we will study this upper bound and establish a statistical relationship with the mmWave and THz channel.

4.2.2 Statistical Analysis

In this subsection, we will further analyze the ergodic capacity of the indoor mmWave and THz system based on the statistical characteristics of the S-V channel model. Hereafter, we omit the frequency and distance parameter in (4.16) for brevity.

The multi-path arrivals can be split into three parts, i.e., the first ray of the first cluster at T_0, the cluster arrivals at $T_i,\ i \neq 0$, and all the ray arrivals of the whole clusters. Thus, from Appendix B.1 and B.2, we can obtain the expectation of the total multi-path power

gain in time duration T_s as

$$\begin{aligned}
&\mathbb{E}[\sum_{i=0}^{N_{clu}-1}\sum_{l=0}^{N_{ray}^{i}-1}|\alpha_{il}|^2] \\
=\ &\mathbb{E}[|\alpha_{00}|^2]+\mathbb{E}[\sum_{i=1}^{N_{clu}-1}|\alpha_{i0}|^2]+\mathbb{E}[\sum_{i=0}^{N_{clu}-1}\sum_{l=1}^{N_{ray}^{i}-1}|\alpha_{il}|^2] \\
=\ &\Psi_0+\Psi_0\Lambda\Gamma(1-e^{-\frac{T_s}{\Gamma}})+\Psi_0\lambda\gamma(1-e^{-\frac{T_s}{\gamma}})+\Psi_0\Lambda\lambda\Gamma\gamma+\frac{\Psi_0\Lambda\lambda\Gamma\gamma}{\Gamma-\gamma}(\gamma e^{-\frac{T_s}{\gamma}}-\Gamma e^{-\frac{T_s}{\Gamma}}).
\end{aligned} \tag{4.17}$$

Moreover, we denote Q_r as the total number of arriving rays in T_s. Since each ray follows the same AoD/AoA distribution, the angle related term can be further expressed as

$$\begin{aligned}
&\mathbb{E}[\sum_{i=0}^{N_{clu}-1}\sum_{l=0}^{N_{ray}^{i}-1}|G_t(\phi_{il}^t,\theta_{il}^t)G_r(\phi_{il}^r,\theta_{il}^r)A_r^{eq}(\phi_{il}^r,\theta_{il}^r)A_t^{eq}(\phi_{il}^t,\theta_{il}^t)|^2] \\
=\ &\mathbb{E}[Q_r]\mathbb{E}[|G_t(\phi_{il}^t,\theta_{il}^t)G_r(\phi_{il}^r,\theta_{il}^r)A_r^{eq}(\phi_{il}^r,\theta_{il}^r)A_t^{eq}(\phi_{il}^t,\theta_{il}^t)|^2].
\end{aligned} \tag{4.18}$$

According to Lemma $B.1$ in Appendix B.1, the average number of total ray arrivals in T_s is

$$\mathbb{E}[Q_r]=\int_0^{T_s}(\Lambda+\lambda+\lambda\Lambda t)\,dt=\Lambda T_s+\lambda T_s+\frac{1}{2}\lambda\Lambda T_s^2, \tag{4.19}$$

and the remaining term in (4.18) can be obtained as in Appendix B.3.

Therefore, the ergodic capacity of the indoor mmWave and THz system is upper bounded by

$$\bar{C}(f,d)\le B\log_2\left[1+\frac{KPM_tM_rN_tN_r}{N_0}\beta(f,d)\right], \tag{4.20}$$

where the frequency and distance dependent variable, β, is defined as

$$\begin{aligned}\beta &= \frac{G_{t0}G_{r0}}{4\pi^4}(\Lambda T_s + \lambda T_s + \frac{1}{2}\lambda\Lambda T_s^2) \\ &\times[w_{1,\varphi}^t \mathcal{G}(\sigma_{1,\varphi}^t, \phi_{min}^t, \phi_{max}^t, \pi) + w_{2,\varphi}^t \mathcal{G}(\sigma_{2,\varphi}^t, \phi_{min}^t, \phi_{max}^t, \pi)] \\ &\times[w_{1,\vartheta}^t \mathcal{G}(\sigma_{1,\vartheta}^t, \theta_{min}^t, \theta_{max}^t, \frac{\pi}{2}) + w_{2,\vartheta}^t \mathcal{G}(\sigma_{2,\vartheta}^t, \theta_{min}^t, \theta_{max}^t, \frac{\pi}{2})] \\ &\times[w_{1,\varphi}^r \mathcal{G}(\sigma_{1,\varphi}^r, \phi_{min}^r, \phi_{max}^r, \pi) + w_{2,\varphi}^r \mathcal{G}(\sigma_{2,\varphi}^r, \phi_{min}^r, \phi_{max}^r, \pi)] \\ &\times[w_{1,\vartheta}^r \mathcal{G}(\sigma_{1,\vartheta}^r, \theta_{min}^r, \theta_{max}^r, \frac{\pi}{2}) + w_{2,\vartheta}^r \mathcal{G}(\sigma_{2,\vartheta}^r, \theta_{min}^r, \theta_{max}^r, \frac{\pi}{2})] \\ &\times[\Psi_0 + \Psi_0\Lambda\Gamma(1 - e^{-\frac{T_s}{\Gamma}}) + \Psi_0\lambda\gamma(1 - e^{-\frac{T_s}{\gamma}}) + \Psi_0\Lambda\lambda\Gamma\gamma + \frac{\Psi_0\Lambda\lambda\Gamma\gamma}{\Gamma - \gamma}(\gamma e^{-\frac{T_s}{\gamma}} - \Gamma e^{-\frac{T_s}{\Gamma}})],\end{aligned} \tag{4.21}$$

in which

$$\begin{aligned}\mathcal{G}(\sigma, x, y, z) \triangleq\ & \frac{x-z}{2}\,\mathrm{erf}\left(\frac{x-z}{\sqrt{2}\sigma}\right) - \frac{x+z}{2}\,\mathrm{erf}\left(\frac{x+z}{\sqrt{2}\sigma}\right) + \frac{\sigma}{\sqrt{2\pi}}\left[e^{-\frac{(x-z)^2}{2\sigma^2}} - e^{-\frac{(x+z)^2}{2\sigma^2}}\right] \\ & + \frac{y+z}{2}\,\mathrm{erf}\left(\frac{y+z}{\sqrt{2}\sigma}\right) - \frac{y-z}{2}\,\mathrm{erf}\left(\frac{y-z}{\sqrt{2}\sigma}\right) + \frac{\sigma}{\sqrt{2\pi}}\left[e^{-\frac{(y+z)^2}{2\sigma^2}} - e^{-\frac{(y-z)^2}{2\sigma^2}}\right]\end{aligned} \tag{4.22}$$

with

$$\mathrm{erf}(x) = \frac{2}{\sqrt{\pi}}\int_0^x e^{-y^2} dy. \tag{4.23}$$

From (4.20) we know that, the ergodic capacity upper bound for the mmWave and THz system is jointly determined by the channel parameters, the subarray number, K, and the antenna element number of each subarray, M_t, N_t, M_r, N_r.

4.3 Effects of Uncertainty in Phase Shifter

Phase uncertainty and impairment is an inevitable practical issue in the mmWave and THz bands. In this section, we will investigate the effect of random errors in the phase shifters and analyze the impact on the ergodic capacity for the mmWave and THz system.

4.3.1 Phase Uncertainty in Phase Shifter

The analog beamformers are based on the wideband phase shifters. However, the shifted phases are subject to variations due to the imperfectness of the graphene/liquid crystal

materials [23, 25], especially at such high frequencies. These uncertainties will result in beam pointing errors, which could degrade the system performance.

Denote $\Delta\psi_{m_t,n_t}(f)$ and $\Delta\psi_{m_r,n_r}(f)$ as the random phase errors at the transmitter and receiver respectively, which are usually frequency dependent in the mmWave and THz band. Thus, the resulting shifted phases become

$$\widetilde{\psi}_{m_t,n_t}(f) = \psi_{m_t,n_t} + \Delta\psi_{m_t,n_t}(f), \tag{4.24}$$

$$\widetilde{\psi}_{m_r,n_r}(f) = \psi_{m_r,n_r} + \Delta\psi_{m_r,n_r}(f), \tag{4.25}$$

where ψ_{m_t,n_t} and ψ_{m_r,n_r} are the corresponding phases of the analog beamformer. Then, the associated array factors will be

$$\begin{aligned}\widetilde{A}_t^{eq}(\phi,\theta,f) &= \frac{1}{\sqrt{M_tN_t}}\sum_{m_t=0}^{M_t-1}\sum_{n_t=0}^{N_t-1} e^{j\frac{2\pi r}{\lambda_c}[m_t\cos\phi\sin\theta+n_t\sin\phi\sin\theta]-\widetilde{\psi}_{m_t,n_t}(f)} \\ &= \frac{1}{\sqrt{M_tN_t}}\sum_{m_t=0}^{M_t-1}\sum_{n_t=0}^{N_t-1} e^{j\frac{2\pi r}{\lambda_c}[m_t\cos\phi\sin\theta+n_t\sin\phi\sin\theta]-\psi_{m_t,n_t}} e^{j\Delta\psi_{m_t,n_t}(f)},\end{aligned} \tag{4.26}$$

and

$$\begin{aligned}\widetilde{A}_r^{eq}(\phi,\theta,f) &= \frac{1}{\sqrt{M_rN_r}}\sum_{m_r=0}^{M_r-1}\sum_{n_r=0}^{N_r-1} e^{j\frac{2\pi r}{\lambda_c}[m_r\cos\phi\sin\theta+n_r\sin\phi\sin\theta]-\widetilde{\psi}_{m_r,n_r}(f)} \\ &= \frac{1}{\sqrt{M_rN_r}}\sum_{m_r=0}^{M_r-1}\sum_{n_r=0}^{N_r-1} e^{j\frac{2\pi r}{\lambda_c}[m_r\cos\phi\sin\theta+n_r\sin\phi\sin\theta]-\psi_{m_r,n_r}} e^{j\Delta\psi_{m_r,n_r}(f)}.\end{aligned} \tag{4.27}$$

Accordingly, the radiation pattern of one antenna subarray for the AP is

$$\begin{aligned}|\widetilde{A}_t^{eq}(\phi,\theta,f)|^2 &= \widetilde{A}_t^{eq}(\phi,\theta,f)\widetilde{A}_t^{eq^\dagger}(\phi,\theta,f) \\ &= \frac{1}{M_tN_t}\sum_{m_t=0}^{M_t-1}\sum_{n_t=0}^{N_t-1}\sum_{m_t'=0}^{M_t-1}\sum_{n_t'=0}^{N_t-1} e^{j\left(\Delta\psi_{m_t,n_t}(f)-\Delta\psi_{m_t',n_t'}(f)\right)} \\ &\quad\times e^{j\frac{2\pi r}{\lambda_c}[(m_t-m_t')\cos\phi\sin\theta+(n_r-n_r')\sin\phi\sin\theta]+(\psi_{m_t,n_t}-\psi_{m_t',n_t'})}.\end{aligned} \tag{4.28}$$

Since $\Delta\psi_{m_t,n_t}(f) - \Delta\psi_{m_t',n_t'}(f)$ is small, we have

$$e^{j\left(\Delta\psi_{m_t,n_t}(f)-\Delta\psi_{m_t',n_t'}(f)\right)} \simeq 1 + j(\Delta\psi_{m_t,n_t}(f) - \Delta\psi_{m_t',n_t'}(f)) - \frac{1}{2}(\Delta\psi_{m_t,n_t}(f) - \Delta\psi_{m_t',n_t'}(f))^2. \tag{4.29}$$

If $\Delta\psi_{m_t,n_t}(f)$ and $\Delta\psi_{m_r,n_r}(f)$ are assumed to follow Gaussian distribution $\mathcal{N}(0,\delta_t^2(f))$ and $\mathcal{N}(0,\delta_r^2(f))$, respectively, the average radiation pattern of one antenna subarray at the transmitter can be obtained by extending the method in [73] as

$$|\bar{A}_t^{eq}(\phi,\theta,f)|^2 \triangleq \mathbb{E}[|\widetilde{A}_t^{eq}(\phi,\theta,f)|^2] = |A_t^{eq}(\phi,\theta)|^2 - |A_t^{eq}(\phi,\theta)|^2\delta_t^2(f) + \delta_t^2(f). \tag{4.30}$$

Similarly, the average radiation pattern at the receiver is given by

$$|\bar{A}_r^{eq}(\phi,\theta,f)|^2 \triangleq \mathbb{E}[|\widetilde{A}_r^{eq}(\phi,\theta,f)|^2] = |A_r^{eq}(\phi,\theta)|^2 - |A_r^{eq}(\phi,\theta)|^2\delta_r^2(f) + \delta_r^2(f). \tag{4.31}$$

We can perceive from (4.30) and (4.31) that there is a degradation in the radiation pattern due to the random phase errors.

4.3.2 Impact on the Ergodic Capacity

According to the average radiation patterns in (4.30) and (4.31), we can get the ergodic capacity upper bound with random shifted phase errors by using the similar analysis as in Section 4.2, which is given by

$$\widetilde{C}(f,d) \le B\log_2\left(1+\frac{KP}{N_0}[M_tN_t-(M_tN_t-1)\delta_t^2(f)][M_rN_r-(M_rN_r-1)\delta_r^2(f)]\beta(f,d)\right). \tag{4.32}$$

Then, the average capacity loss in the upper bound can be calculated as

$$\begin{aligned}
&\Delta\bar{C}_u(f,d) \triangleq \bar{C}_u(f,d) - \widetilde{C}_u(f,d)\\
= \;& B\log_2\left(1+\frac{KPM_tM_rN_tN_r}{N_0}\beta(f,d)\right)\\
&-B\log_2\left(1+\frac{KP}{N_0}[M_tN_t-(M_tN_t-1)\delta_t^2(f)][M_rN_r-(M_rN_r-1)\delta_r^2(f)]\beta(f,d)\right).
\end{aligned} \tag{4.33}$$

When SNR, $\frac{P\beta(f,d)}{N_0}$, and subarray parameters, K, M_t, N_t, M_r, N_r, are small,

$$\begin{aligned}
\Delta\bar{C}_u(f,d) \;\simeq\; & \frac{BKP\beta(f,d)}{N_0}\Big(M_rN_r(M_tN_t-1)\delta_t^2(f)\\
&+M_tN_t(M_rN_r-1)\delta_r^2(f)-(M_tN_t-1)(M_rN_r-1)\delta_t^2(f)\delta_r^2(f)\Big).
\end{aligned} \tag{4.34}$$

But when they become large,

$$\begin{aligned}\Delta\bar{C}_u(f,d) \;\simeq\; & -B\log_2\Big(1+(1-\frac{1}{M_tN_t})(1-\frac{1}{M_rN_r})\delta_t^2(f)\delta_r^2(f)\\ & -(1-\frac{1}{M_tN_t})\delta_t^2(f)-(1-\frac{1}{M_rN_r})\delta_r^2(f)\Big).\end{aligned} \tag{4.35}$$

According to (4.34) and (4.35), when M_t, N_t, M_r, N_r are small, the capacity loss due to the phase uncertainties increases significantly with the increasing subarray size. However, when M_t, N_t, M_r, N_r become large, such increment in degradation becomes small, and finally approaches a degradation bound, $-B\log_2(1+\delta_t^2(f)\delta_r^2(f)-\delta_t^2(f)-\delta_r^2(f))$.

4.3.3 Design of Subarray Size and Number

Relying on the analysis of the capacity loss with random phase errors, we can design the subarray structure accordingly.

Communications over the mmWave and THz band should be reliable under phase uncertainties in any cases. Since there exists a relatively serve capacity loss resulting from the phase uncertainties when the subarray size is small, the number of antenna elements in each subarray should not be too small. On the other hand, the subarray size cannot be too large due to the limitation of the hardware and integrated circuits in the mmWave and THz band. Thus, it is reasonable to choose the subarray size satisfying the condition (4.35).

Therefore, given the capacity degradation threshold ε for the phase uncertainties, we can determine the subarray size M_t, N_t, M_r, N_r based on (4.35). For example, if we assume the antenna subarrays at the AP and the user side have the same structure, i.e., $M_t = M_r$, $N_t = N_r$ and $\delta_t^2(f) = \delta_r^2(f) \triangleq \delta^2(f)$, to ensure the capacity degradation ε, the subarray structure should satisfy

$$M_tN_t = M_rN_r \le \frac{\delta^2(f)}{2^{-\frac{\varepsilon}{2B}}+\delta^2(f)-1}. \tag{4.36}$$

That is to say, the optimal antenna subarray size should be

$$M_tN_t = M_rN_r = \left\lfloor \frac{\delta^2(f)}{2^{-\frac{\varepsilon}{2B}}+\delta^2(f)-1} \right\rfloor. \tag{4.37}$$

Table 4.1 System Parameters

Parameters	Values
Operating frequency f	0.3 THz
Transmit power P	3 dBm
Time duration T_s	50 ns
Cluster arrival rate Λ	0.13 ns^{-1}
Ray arrival rate λ	0.37 ns^{-1}
Cluster decay factor Γ	3.12 ns
Ray decay factor γ	0.91 ns
Absorption coefficient k_{abs}	0.0033 m^{-1}
Antenna gain $G_{t0} = G_{r0}$	20 dBi
Bandwidth B	10 GHz
Noise N_0	−75 dBm

where $\lfloor \cdot \rfloor$ denotes the floor function.

Then, given the subarray size, to guarantee a long-term transmission rate R for certain distance d, the number of antenna subarrays should satisfy

$$K(f,d) \geq \frac{N_0(2^{\frac{R}{B}}-1)}{PM_tM_rN_tN_r\beta(f,d)}, \tag{4.38}$$

namely, the minimum number of antenna subarrays should be

$$K(f,d) = \left\lceil \frac{N_0(2^{\frac{R}{B}}-1)}{PM_tM_rN_tN_r\beta(f,d)} \right\rceil, \tag{4.39}$$

where $\lceil \cdot \rceil$ is the ceiling function.

4.4 Numerical Results

In this section, extensive numerical results are provided to illustrate and verify the performance of the indoor single-user mmWave and THz system.

The operating frequency is set as 0.3 THz, i.e, 300 GHz. We consider the same indoor environment as in [15, 71], where the plaster wall material is used and the indoor humidity is 10%. Furthermore, the space between antenna elements in each subarray is set as $a = \frac{\lambda_c}{8}$, and the sector angle of the antenna is set to be 60°-wide in the azimuth domain and 30°-wide in elevation. The detailed simulation parameters are listed in Table I, which are obtained

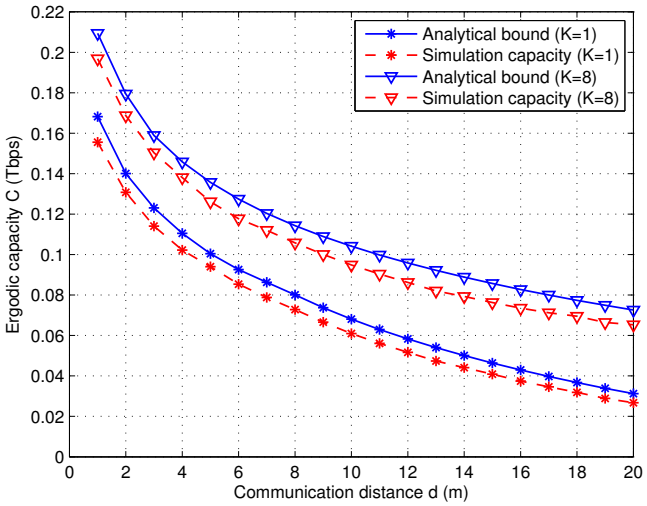

Fig. 4.2 Illustration of the tightness of the analytical upper bound for the ergodic capacity.

from measurements in [15, 18, 71]. The parameters concerning AoD/AoA can be found in Table III in [71].

Fig. 4.2 shows the tightness of the upper bound on the ergodic capacity as a function of the distance for different subarray numbers. Note that the simulated capacity is obtained from the average over 5,000 channel realizations. The subarray antenna element number is set as $M_t \times N_t = M_r \times N_r = 8 \times 8$. As shown in Fig. 4.2, the mmWave and THz system can support Tbps communications, and the analytical bound matches the simulation capacity across the distance for different antenna numbers. This indicates the approximation is valid and well justified. Specifically, the gap between the bound and the capacity is caused by using inequalities (4.15) and (4.16). Also, there exists an envelop approximation loss as described in Appendix B.3. Such loss may increase slightly with the subarray antenna element number. Furthermore, we can see from the figure that the ergodic capacity generally decreases with the increase of the distance as we can imagine. Using a larger number of subarrays can compensate for the path loss brought by the distance.

Fig. 4.3 plots the average capacity degradation with random phase errors versus the antenna subarray size with $d = 10$ m. Particularly, Fig. 4.3(a) demonstrated the absolute capacity loss, while Fig. 4.3(b) shows the relative capacity, namely, the ratio of the ergodic

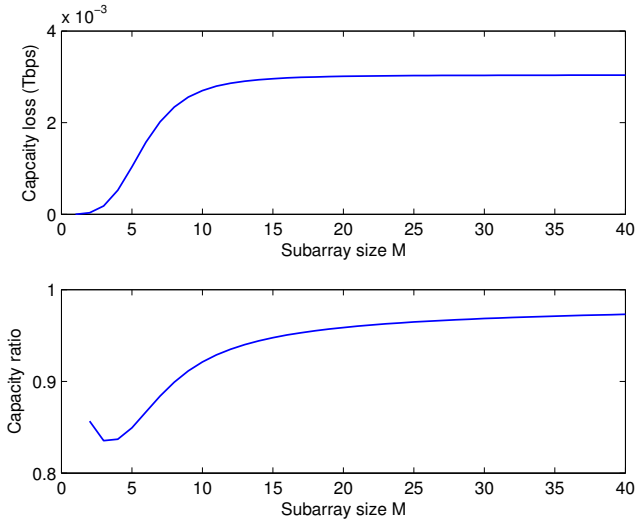

Fig. 4.3 The average capacity degradation versus the antenna subarray size with $d = 10$ m.

capacity with and without phase errors. Here, the low SNR condition with a smaller transmit power, $P = 0$ dBm, is considered. And, we set the transmit and receive antenna element number in each subarray as $M_t = N_t = M_r = N_r \triangleq M$, and the subarray number as $K = 8$, and the variance of phase uncertainty as $\delta_t^2 = \delta_r^2 = 0.1$. As illustrated in Fig. 4.3(a) that the capacity degradation increases with the antenna subarray size and finally approaches the limits. Furthermore, it can be observed from Fig. 4.3(b) that the phase uncertainties can cause about 3-15% loss. Specifically, the relative capacity loss increases with the subarray size when the size is small, while it decreases when the size becomes large. The reason is that the degradation from phase errors is much less than the gain brought by the subarray with large antennas. Therefore, according to Fig. 4.3, the subarray size should not be too small considering for the performance degradation resulting from the phase uncertainties. For instance, to ensure a 10% average capacity loss with phase uncertainties, it should be appropriate to choose the subarray size as $M_t = N_t = M_r = N_r = 8$.

We compare the ergodic capacity of different subarray structures for different distances in Fig. 4.4. Specifically, the four 8×8 subarrays and one 16×16 subarray at the transmitter are considered, where the antenna element numbers are same. Taking a close look at Fig. 4.4, we can see that the ergodic capacity of the four 8×8 subarray system outperforms

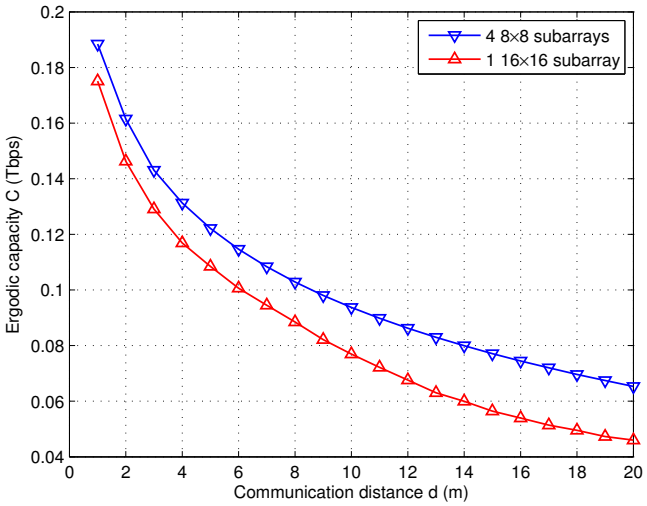

Fig. 4.4 The ergodic capacity of different subarray structures for different distances.

that of one 16×16 subarray, especially when the communication distance is large. This is because that the mmWave and THz system with subarrays can provide directional antenna gains as well as spatial diversity gains.

In Fig. 4.5, we plot the ergodic capacity upper bound as a function of the antenna subarry number with 10 m distance. The subarray antenna element number is set as $M_t \times N_t = M_r \times N_r = 8 \times 8$. From Fig. 4.5, the ergodic capacity increases with the antenna subarray number, while the capacity gain becomes small when subarray number becomes large. This is expected as, the system has diversity gain and SNR gain with multiple subarrays, but the diversity gain will saturate when the subarrays reach certain number. Therefore, increasing the number of subarray is not an efficient methods to obtain more performance gain when the array number is large enough.

At last, Fig. 4.6 demonstrates the required antenna subarray numbers for different distances to ensure a 0.1 Tbps transmission rate. The subarray antenna element number is also $M_t \times N_t = M_r \times N_r = 8 \times 8$. As shown in Fig. 4.6 that, the farther the distance, the more antenna subarray number is needed to compensate the increasing path loss. However, the subarray number is also limited by the practical antenna aperture size. Therefore, from Fig. 4.3, Fig. 4.5 and Fig. 4.6, we can conclude that, for the mmWave and THz system,

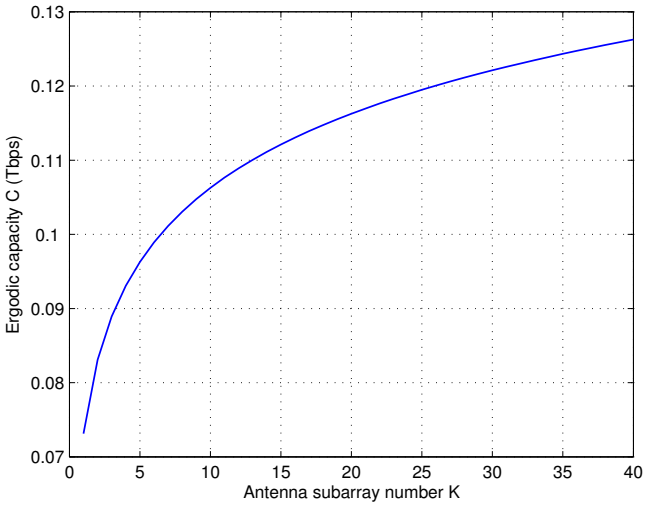

Fig. 4.5 The ergodic capacity versus the antenna subarray number with d = 10 m.

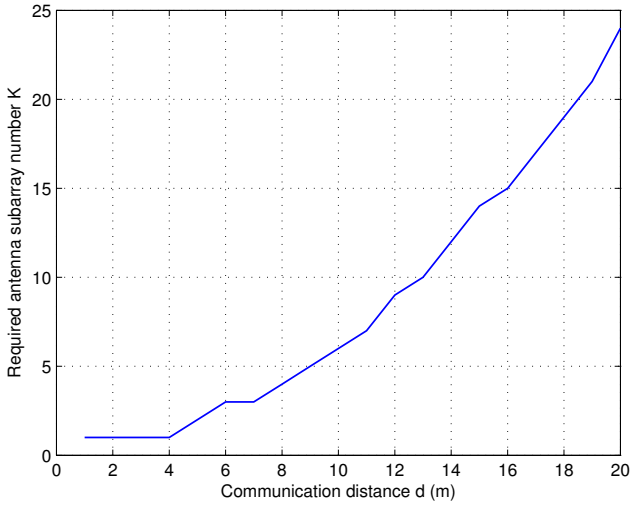

Fig. 4.6 The required antenna subarray numbers for different distances to guarantee 0.1 Tbps data rate.

it is better to properly increase the subarray size within the acceptable range of the phase-uncertainty degradation, and use appropriate subarray number to achieve transmission rate for certain distance.

4.5 Conclusions

This chapter has studied an indoor single-user mmWave and THz communication system with antenna subarrays. An upper bound of the ergodic capacity with hybrid beamforming is investigated. Furthermore, we analyze the impact of random phase shifter errors on the ergodic capacity of the system. Finally, we provide a guideline on designing the subarray size and number to guarantee a certain long-term data rate at different communication distances. A few important conclusions have been made along with the numerical results. First, the proposed indoor mmWave and THz system can effectively support Tbps communications and outperforms the conventional systems with only one array by providing the array gain as well as the spatial diversity gain. Secondly, the analytical ergodic capacity upper bound is valid for approximating the single-user mmWave and THz system performance limits. Thirdly, the mmWave and THz system would suffer performance degradation due to the uncertainties in the phase shifters. Such degradation generally increases with the antenna subarray size and finally approaches a limit. Last but not least, it is better not to choose a small subarray size because of the relatively large performance loss brought by the random phase errors. With proper design of antenna subarray size and number, the mmWave and THz system can achieve target long-term transmission rates at different distances.

CHAPTER 5

DISTANCE-AWARE MULTIUSER WIDEBAND COMMUNICATIONS

To fully exploit the large bandwidth in the higher-mmWave and THz bands, in this chapter, we will further explore the array-of-subarrays structure for multiuser wideband communications. With respect to the distinguished characteristics of the THz channels, we will only consider the design for the THz band here. Similar system models in Chapter 3 with omni-directional antennas are considered for multiuser situations.[10] By taking advantage of the distance-frequency dependent characteristic in the THz band, we develop a distance-aware multi-carrier transmission policy for multiuser communications. Then, we propose a hybrid beamforming scheme for distance-aware multi-carrier transmissions. Specifically, a two-step beamsteering searching and user grouping strategy in the analog domain and an antenna subarray selection and adaptive power allocation policy in the digital domain are developed.

The rest of this chapter is organized as follows. In Section 5.1, we develop a distance-aware multi-carrier transmission strategy for THz communications. Hybrid beamforming schemes with user grouping and antenna subarray selection are proposed in Section 5.2. Simulation results are provided in Section 5.3 to verify the effectiveness of the proposed scheme and algorithms. Finally, we conclude the chapter in Section 5.4.

5.1 Distance-Aware Multi-Carrier Transmission

In light of the transmission windows in Fig. 1.2, the available bandwidth for long-distance users is part of the available bandwidth for short-distance users. Therefore, to alleviate the impact brought by the path loss, long-distance users can only use the central part of the bandwidth while short-distance users can use both the central part and the sides for

[10] We also assume the distance between adjacent subarrays is much larger than the antenna-element spacing and UPAs are used.

transmission. For instance, with regard to the transmission window, 0.55-0.75 THz, in Fig. 1.2, only 0.6-0.7 THz can be used for 10 m transmission while the whole band can be used for 1 m transmission. Accordingly, a distance-aware scheme [93] has been developed to optimize the wideband system performance, which would accommodate long-distance communications first.

Meanwhile, the bandwidth is no longer scarce in the THz band. Thus, orthogonal frequency division multiplexing (OFDM) is not necessary anymore due to its high complexity in processing ultra-broadband and ultra-fast data at THz frequencies.[11] Instead, multi-carrier transmission, allowing non-overlapping and equally-spaced parallel single-carrier sub-windows, appears to be a promising alternative, which has been demonstrated in many photonics-based THz experiments using wavelength-division-multiplexing (WDM) [94–97]. Although multi-carrier is not so spectrum-efficient as OFDM, it has much lower complexity in handling individual carrier.

In summary, for the distance-aware multi-carrier transmission in the THz system, users at different distances will use different parts of the THz spectrum, which is further divided into several non-overlapping sub-windows for multi-carrier transmission.

5.2 Hybrid Beamforming with User Grouping and Antenna Subarray Selection

In this section, based on the distance-aware multi-carrier transmission, we will focus on the hybrid beamforming design with user grouping and antenna subarray selection.

An example of home implementation for multiuser THz WPAN is shown in Fig. 5.1(a). As mentioned before, time-delay components will be used for wideband communications. According to (3.3), since the true time delays are same for all the frequencies, the associated shifted phases will vary over frequencies but lead to a same steering direction [12]. As a result, the time-delay-based beamsteering codebook can also be adopted for wideband

[11] The peak-average-power-ratio (PAPR) issues and hardware impairments, such as PA nonlinearity, carrier frequency offset (CFO), and phase noise, will be more severe for OFDM in higher frequency bands, which require more complex processing.

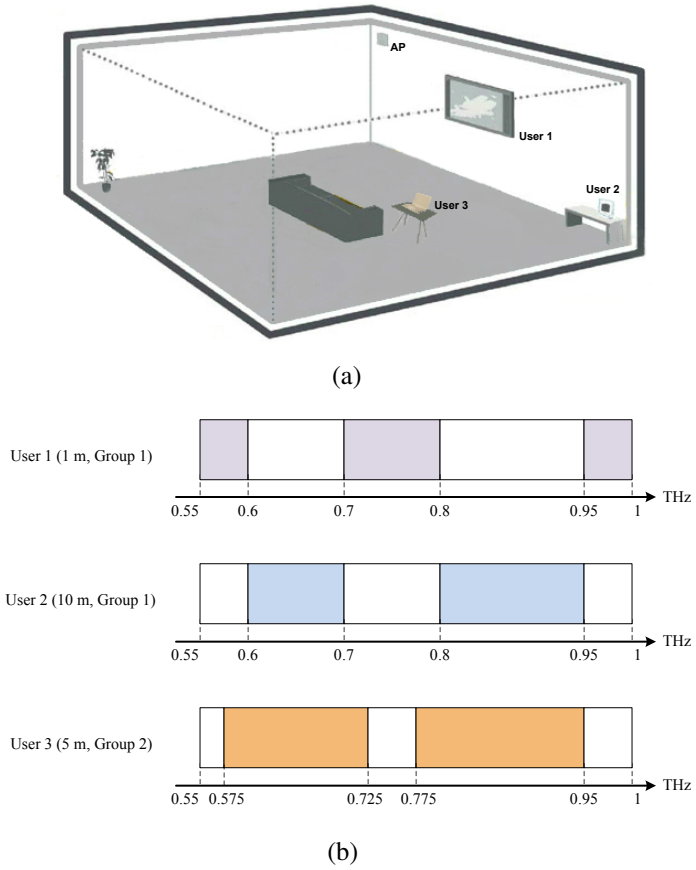

Fig. 5.1 Multiuser wideband THz communications: (a) a home implementation scenario for THz WPAN; (b) group-based distance-aware multi-carrier transmission.

analog beamforming. Furthermore, as angular spread is limited at THz frequencies, the spatial information can be utilized for user grouping to achieve the gain of frequency reuse [98]. In the following, we will develop two-step analog beamforming with user grouping and the corresponding digital beamforming with subarray selection.

5.2.1 Two-Step Analog Beamforming

The analog beamforming for the multiuser THz system is divided into two stages, i.e., pre-scanning with user grouping and precise beamforming.

5.2.1.1 Pre-scanning and user grouping

In the first step, subarrays activate a subset of antennas to perform a fast, wide and rough beam pre-scanning together. Particularly, the angular separation of the pre-scanning sectors

is determined by the angular spread in the THz band.[12] As a result, users can be partitioned according to their AoDs. Users belonging to the same angle section are assigned into the same user group; otherwise, they are in different user groups.

Since users in different groups are out of the angular spread range, they can be regarded as spatially-separated with completely different AoDs for all the paths. As proved in [42, 43] that, at large antenna regime, the beemsteering vectors parameterized by angles with large separation are nearly orthogonal, i.e.,

$$\mathbf{a}^{*}_{UPA}(M, N, \phi_i, \theta_i)\mathbf{a}_{UPA}(M, N, \phi_l, \theta_l) \simeq 0, \qquad \phi_i \neq \phi_l, \theta_i \neq \theta_l. \tag{5.1}$$

Thus, these vectors in the codebook within the corresponding angle section can be used by a user group for both beamforming and inter-group interference cancellation. As a result, different user groups can share the same THz frequency resources without interference.

On the other hand, users in the same group may experience common scatterers from the same subarray and present similar AoD of some paths, upon which beamsteering will lead to interference among those users. By exploiting the distance-frequency dependent channel characteristics and the disjoint structure of subarrays, we can adopt distance-aware frequency division to manage the interference in a user group. Specifically, long-distance users will be assigned the central part of the band first and short-distance users will use the sides. For example, considering the transmission window, 0.55-1 THz, for a user group in Fig. 5.1(b), 0.6-0.7 THz and 0.8-0.95 THz can be used by the 10 m user while 0.55-0.6 THz, 0.7-0.75 THz, and 0.95-1 THz can only be assigned to the user with 1 m. It should be noted that we do not consider joint frequency allocation here because the long-distance user has much more severe path loss so that it should be assigned first to guarantee QoS.

With the pre-scanning and user grouping, the same THz frequency resource can be reused among different user groups, which could greatly improve the system efficiency. Also, the antenna subarrays are shared by users in the same group, which could in turn

[12] According to the maximal angular spread, 40°, in the THz channels [15, 20], the angular separation can be designed as 45°.

reduce the power consumption of active RF circuits as well as the complexity of the THz system.

5.2.1.2 Precise beamforming

After the pre-scanning and user grouping in the first step, each subarray carries out precise beamforming searching for each user group using the codebook in the pre-scanned sector. Specifically, we denote the user set in group q as $\mathcal{J}_q$, and group index set as $\mathcal{Q}$. The selected window for user $j \in \mathcal{J}_q$ is denoted as $\mathcal{W}_j$, where each sub-window $w \in \mathcal{W}_j$ has a smaller bandwidth B with central frequency f_j^w.

Since there is a unique beamforming direction for each subarray, the precise beamforming angle for user group q should be selected from the codebook in the pre-scanned sectors so that the overall normalized received signal power of the user group over all subcarriers is maximized, which can be expressed as[13]

$$\{\Phi_q, \Theta_q\} = \underset{\substack{\Phi_q \in \Phi, \\ \Theta_q \in \Theta}}{\arg\max} \sum_{j \in \mathcal{J}_q} \sum_{w \in \mathcal{W}_j} \frac{\left\| \mathbf{h}^{eq}(f_j^w, d_j) \right\|^2}{L_{PL}(f_j^w, d_j)}, \tag{5.2}$$

where Φ_q and Θ_q are the sets of selected transmit beamforming vectors for different subarrays and receive beamforming vectors for different users in group $\mathcal{J}_q$, respectively, Φ and Θ are the transmit and receive beamsteering codebooks in the pre-scanned sectors, respectively, $\mathbf{h}^{eq}(f_j^w, d_j)$ is the effective channel at baseband as in (4.14), and the normalized factor, $L_{PL}(f_j^w, d_j)$, is defined in (2.6). It should be noted that the effective channel gains are normalized here based on distance to ensure the fairness among users. As a result, the analog beamforming direction is jointly determined by the LOS paths and the strongest NLOS paths of all the users in one group. Furthermore, we denote the effective channel with the analog beamforming obtained from (5.2) as $\tilde{\mathbf{h}}^{eq}(f_j^w, d_j)$.

[13] As the subarrays are disjoint, the selection process can be performed by fixing the receive beamforming direction first and then searching the transmit beamforming angles for each subarray individually. Orthogonal training sequences can be adopted. Since the indoor environments are mostly static with limited users, the beamsteering angles do not need to updated frequently. Thus, the cost is tolerable for the THz system.

5.2.2 Digital Beamforming

Given the analog beamforming, a digital beamformer is performed on each subcarrier at baseband by a routing part for antenna subarray selection and a controlling part for phase and amplitude regulation. Here, we assume that the effective channel information of subarrays with analog beamforming in (5.2), $\tilde{\mathbf{h}}^{eq}(f_j^w, d_j)$, is available at AP through feedback, where the explicit CSI of specific antenna elements, $\mathbf{H}(f_j^w, d_j)$, is not needed. Since the subarray number is much less than the antenna number, the information overhead will be notably reduced. We further denote the selected subarray set for user group q as $\mathcal{K}_q$. It is worth mentioning that, since each subarray in the THz system can only choose one unique analog beamforming direction, it should be exclusively assigned to one user group as a result of spatial separation.

Since there is no interference among users by performing analog beamforming for inter-group interference cancellation and adopting orthogonal frequency resources within a user group, users can design the digital beamforming individually. Accordingly, MRT can be carried out for users in the same group to transmit signals through a specific set of subarrays. Thus, the digital beamforming vector, $\tilde{\mathbf{v}}(f_j^w, d_j)$, for user $j \in \mathcal{J}_q$ with selected antenna subarray $\mathcal{K}_q$ as

$$\tilde{v}_k^*(f_j^w, d_j) = \begin{cases} \tilde{h}_k^{eq}(f_j^w, d_j), & k \in \mathcal{K}_q, \\ 0, & \text{otherwise.} \end{cases} \tag{5.3}$$

Thus, the normalized digital beamformer for user j in the THz system is

$$\mathbf{v}(f_j^w, d_j) = \frac{\tilde{\mathbf{v}}(f_j^w, d_j)}{\|\tilde{\mathbf{v}}(f_j^w, d_j)\|}. \tag{5.4}$$

In particular, compared with the conventional block diagonalization based multiuser MIMO antenna selection [99], where the baseband precoding of all the users' data streams is performed across the entire selected antenna subset, the antenna subarrays selected for a user group in this paper are disjoint from the antenna subset for other groups. Thus, the data streams of a user group are only be routed to selected subarrays other than the whole

antennas, which could simplify the RF processing and reduce the hardware cost.

Therefore, for a flat-fading THz channel with bandwidth B, centered around the frequency f_j^w, and transmit power p_j^w, the transmission rate for user $j \in \mathcal{J}_q$, with selected subarray set $\mathcal{K}_q$ and the hybrid beamforming in (5.2) and (5.4), is given by

$$\begin{aligned} R_j(\mathcal{W}_j, d_j) &= \sum_{w \in \mathcal{W}_j} B \log_2 \left(1 + \frac{p_j^w}{N_0} \|\tilde{\mathbf{v}}(f_j^w, d_j)\|^2\right) \\ &= \sum_{w \in \mathcal{W}_j} B \log_2 \left(1 + \frac{p_j^w}{N_0} \sum_{k \in \mathcal{K}_q} |\tilde{h}_k^{eq}(f_j^w, d_j)|^2\right), \qquad j \in \mathcal{J}_q, \end{aligned} \tag{5.5}$$

where N_0 is the noise power at the receiver.

5.2.3 Antenna Subarray Selection and Power Allocation

By adopting hybrid beamforming with distance-aware multi-carrier transmission, users in the THz system can enjoy antenna gains as well as spatial and selection diversity gains. In this subsection, we will investigate the antenna subarray selection strategy with power adaptation for the beamforming.

5.2.3.1 Problem Formulation

For the THz system, with antenna subarray selection, users can dynamically use appropriate number of beams to accommodate different needs at different distances, which could reduce the hardware complexity as well as the circuit power consumption. Denote $\rho_{q,k}$ as the binary antenna subarray selection indicator for user group $\mathcal{J}_q$ with subarray k, the rate in (5.5) for user $j \in \mathcal{J}_q$ can be rewritten as

$$R_j = \sum_{w \in \mathcal{W}_j} B \log_2 \left(1 + \frac{p_j^w}{N_0} \sum_{k \in \mathcal{K}} \rho_{q,k} |\tilde{h}_k^{eq}(f_j^w, d_j)|^2\right), \quad \forall j \in \mathcal{J}_q. \tag{5.6}$$

Since each subarray could only be assigned to one user group, it is important to determine how many and which subarrays should be selected for transmission to guarantee a certain QoS.

With the effective channel information of subarrays at baseband, we aim to find an adaptive antenna subarray selection and power allocation strategy for the distance-aware

multiuser hybrid beamforming so as to use as few active RF components as possible while ensuring different data transmission rates for different users. Then, the problem can be formulated as

$$\min_{\boldsymbol{p},\boldsymbol{\rho}} \quad \sum_{q\in\mathcal{Q}}\sum_{k\in\mathcal{K}}\rho_{q,k}, \tag{5.7}$$

$$s.t. \quad R_j \geq \tilde{R}_j, \qquad \forall j \in \mathcal{J}, \tag{5.7a}$$

$$\sum_{j\in\mathcal{J}}\sum_{w\in\mathcal{W}_j} p_j^w \leq P, \quad \forall j \in \mathcal{J}, \tag{5.7b}$$

$$\sum_{q\in\mathcal{Q}}\rho_{q,k} \leq 1, \qquad \forall k \in \mathcal{K}, \tag{5.7c}$$

$$\rho_{q,k} \in \{0,1\}, \qquad \forall q \in \mathcal{Q}, \forall k \in \mathcal{K}, \tag{5.7d}$$

$$p_j^w \geq 0, \qquad \forall j \in \mathcal{J}, \forall w \in \mathcal{W}_j, \tag{5.7e}$$

where $\tilde{R}_j$ is the minimum rate requirement[14] for user j and P is the total transmit power constraint at AP. We denote $\boldsymbol{p} = \{p_j^w | j \in \mathcal{J}, w \in \mathcal{W}_j\}$ as the set of users' powers and $\boldsymbol{\rho} = \{\rho_{q,k} | q \in \mathcal{Q}, k \in \mathcal{K}\}$ as the set of antenna subarray selection indicators.

As we know, problem (5.7) is a mixed integer programming problem [100], where constraints (5.7a), (5.7b) are convex and other constraints are affine. Finding the optimal solution needs exhaustive search with exponential complexity, which is prohibitive due to the large number of users and antenna subarrays. Therefore, we need to develop an approach, which not only offers a good solution (not necessarily the optimal) but also keeps low complexity for the THz system.

[14]The rate requirements should be well selected to ensure there exists a solution for the optimization problem.

5.2.3.2 *Optimal Power Allocation*

We first analyze the optimal power allocation for given subarray assignment $\boldsymbol{\rho}$. Thus, problem (5.7) can be rewritten as

$$\min_{\boldsymbol{p}} \quad \sum_{q\in\mathcal{Q}}\sum_{k\in\mathcal{K}}\rho_{q,k} \tag{5.8}$$

$$s.t. \quad (5.7a), (5.7b), (5.7e)$$

It is easy to show that problem (5.8) is a convex optimization problem. We define the Lagrangian of (5.8) as

$$\mathcal{L}(\boldsymbol{p},\boldsymbol{\rho},\boldsymbol{\lambda},\boldsymbol{\mu}) = \sum_{q\in\mathcal{Q}}\sum_{k\in\mathcal{K}}\rho_{q,k} + \sum_{j\in\mathcal{J}}\mu_j(R_j - r_j^q) + \lambda(\sum_{j\in\mathcal{J}}\sum_{w\in\mathcal{W}_j} p_j^w - P), \tag{5.9}$$

where λ is the Lagrangian multiplier related to the total power constraint (5.7b), and $\boldsymbol{\mu} = \{\mu_j | j \in \mathcal{J}\}$ are the Lagrangian multipliers associated with the QoS constraint (5.7c). Then, the dual problem of (5.8) can be stated as

$$\max_{\lambda,\boldsymbol{\mu}} \ \min_{\boldsymbol{p}\geq 0} \ \mathcal{L}(\boldsymbol{p},\boldsymbol{\rho},\lambda,\boldsymbol{\mu}). \tag{5.10}$$

Note that the subgradient-based methods, e.g., ellipsoid method [100], can be employed to update $\{\lambda,\boldsymbol{\mu}\}$ towards the optimal $\{\lambda^*,\boldsymbol{\mu}^*\}$ with the subgradients as

$$\Delta\lambda = \sum_{j\in\mathcal{J}}\sum_{w\in\mathcal{W}_j} p_j^w - P, \tag{5.11}$$

$$\Delta\mu_j = R_j - r_j. \qquad \forall j \in \mathcal{J}. \tag{5.12}$$

Then, by applying the Karush-Kuhn-Tucker (KKT) conditions [100], the optimal power allocation is given by

$$p_j^w = \left(\frac{\mu_j B}{\lambda \ln 2} - \frac{N_0}{\sum\limits_{k\in\mathcal{K}}\rho_{q,k}|\tilde{h}_k^{eq}(f_j^w, d_j)|^2}\right)^+, \qquad \forall j \in \mathcal{J}_q, \forall w \in \mathcal{W}_j, \tag{5.13}$$

where $(x)^+ \triangleq \max\{x, 0\}$. (5.13) shows that the optimal power allocation is achieved by multi-level water-filling. Specifically, the water level of each user depends explicitly on its QoS requirement and the subarray assignment, which can differ from one another.

Table 5.1 Utility-based greedy algorithm for antenna subarray selection in the THz system

Algorithm 5.1 Utility-based greedy algorithm

Initialize user group set $\mathcal{J}_q$ and $\mathcal{Q}$, antenna subarray set $\mathcal{K}$, subarray assignment set $\mathcal{S}_q = \varnothing$, $\Omega_j^w = 0$, and $r_j = 0$, where $j \in \mathcal{J}, w \in \mathcal{W}_j, q \in \mathcal{Q}$.
Initialize $\mathcal{J}_q' = \mathcal{J}_q, \forall q \in \mathcal{Q}$.
repeat
  Obtain $(q^*, k^*) = \arg \max_{q \in \mathcal{Q}, k \in \mathcal{K}} \sum_{j \in \mathcal{J}_q'} \left[\sum_{w \in \mathcal{W}_j} B \log_2 \left[1 + \frac{p_j^w}{N_0} (\Omega_j^w + |\tilde{h}_k^{eq}(f_j^w, d_j)|^2)\right] - r_j \right]$.
  Update $\mathcal{S}_{q^*} = \mathcal{S}_{q^*} \bigcup \{k^*\}$, and $\Omega_j^w = \Omega_j^w + |\tilde{h}_{k^*}^{eq}(f_j^w, d_j)|^2, \forall j \in \mathcal{J}_{q^*}$.
  Update $R_j = \sum_{w \in \mathcal{W}_j} B \log_2 (1 + \frac{p_j^w}{N_0} \Omega_j^w), \forall j \in \mathcal{J}_{q^*}$.
  Update $\mathcal{K} = \mathcal{K} - \{k^*\}$.
  if $R_j \geq \tilde{R}_j$ for some $j \in \mathcal{J}_q'$ **then**
    Update $\mathcal{J}_q' = \mathcal{J}_q' - \{j\}$.
    if $\mathcal{J}_q' = \varnothing$ **then**
      Update $\mathcal{Q} = \mathcal{Q} - \{q\}$.
    end if
  end if
until set $\mathcal{Q}$ becomes empty.

5.2.3.3 Adaptive Antenna Subarray Selection

Given the optimal power allocation (5.13), the antenna subarray selection problem can be stated as

$$\min_{\boldsymbol{\rho}} \quad \sum_{q \in \mathcal{Q}} \sum_{k \in \mathcal{K}} \rho_{q,k} \tag{5.14}$$

$$s.t. \quad (5.7a), (5.7c), (5.7d).$$

Problem (5.14) is NP-hard and is difficult to find an elegant optimal solution. To ensure low complexity for the THz system, next we will seek for effective sub-optimal antenna subarray selection policies to solve this problem.

The greedy algorithm has been proven to be efficient with relatively low complexity for antenna selection [99, 101]. Thus, a utility-based greedy algorithm is proposed as Algorithm 5.1 in Table 5.1. The main idea of the algorithm is to select one antenna subarray to one

Table 5.2 Group-based greedy algorithm for antenna subarray selection in the THz system

Algorithm 5.2 Group-based greedy algorithm

Initialize user set $\mathcal{J}_q$ and $\mathcal{Q}$, antenna subarray set $\mathcal{K}$, subarray assignment set $\mathcal{S}_q = \varnothing$, and $\Omega_j^w = 0$, where $j \in \mathcal{J}, w \in \mathcal{W}_j, q \in \mathcal{Q}$.
Initialize $\mathcal{J}_q' = \mathcal{J}_q, \forall q \in \mathcal{Q}$.
repeat
  Construct group rate profit matrix with (q,k)-element as $\hat{R}_{q,k} = \sum_{j \in \mathcal{J}_q'} \left[\sum_{w \in \mathcal{W}_j} B \log_2 \left[1 + \frac{p_j^w}{N_0}(\Omega_j^w + |\tilde{h}_k^{eq}(f_j^w, d_j)|^2)\right]\right]$.
  Use the Hungarian method to find the assignments $\rho_{q,k}$.
  if $\rho_{q,k} = 1$ **then**
    Update $\mathcal{S}_q = \mathcal{S}_q \bigcup \{k\}$, $\Omega_j^w = \Omega_j^w + |\tilde{h}_k^{eq}(f_j^w, d_j)|^2$, and $R_j = \sum_{w \in \mathcal{W}_j} B \log_2 (1 + \frac{p_j^w}{N_0}\Omega_j^w), \forall j \in \mathcal{J}_q$.
    Update $\mathcal{K} = \mathcal{K} - \{k\}$.
  end if
  if $R_j \geq \tilde{R}_j$ for some $j \in \mathcal{J}_q'$ **then**
    Update $\mathcal{J}_q' = \mathcal{J}_q' - \{j\}$.
    if $\mathcal{J}_q' = \varnothing$ **then**
      Update $\mathcal{Q} = \mathcal{Q} - \{q\}$.
    end if
  end if
until set $\mathcal{Q}$ becomes empty.

user group in each step, leading to the highest increase in the user group's total transmission rate. The user is removed from the group in the algorithm once its QoS requirement is met, until all users are selected, i.e., the QoS requirements of all the users are satisfied. Note that the complexity of the algorithm is $O(|\mathcal{Q}|^2|\mathcal{K}|)$.

It should be noted that Algorithm 5.1 does not take the fairness among user groups into consideration, namely, subarrays with good channel resources may be assigned to the same user group. To overcome this disadvantage, we develop a group-based greedy algorithm as Algorithm 5.2 in Table 5.2, where in each step each user group is assigned an antenna subarray such that the group rate profit is as large as possible. Clearly, this selection process in each step is a standard linear assignment problem and can be efficiently solved by the Hungarian method [102]. The complexity of this algorithm is $O(|\mathcal{K}|^3)$, which is a little

Table 5.3 Overall algorithm for power allocation and antenna subarray selection in the THz system

Algorithm 5.3 Overall algorithm

1: **Initialize** $p_j^w = \frac{P}{JW_j}$, where $j \in \mathcal{J}, w \in \mathcal{W}_j$, and $W_j = |\mathcal{W}_j|$.
2: **Initialize** λ, and μ_j for $j \in \mathcal{J}$.
3: **repeat**
4: Obtain the antenna subarray selection using Algorithm 1 or Algorithm 2.
5: Obtain the optimal power allocation and transmission rate in (5.13) and (5.6), respectively.
6: Update λ and μ_j with subgradients in (5.11) and (5.12), respectively.
7: **until** λ and μ_j converge.

higher than the utility-based algorithm.

Based on the above subarray selection algorithms, the overall adaptive power allocation and antenna subarray selection algorithm is stated as Algorithm 5.3 in Table 5.3.

Finally, the adaptive beamforming strategy with antenna subarray selection and power allocation for distance-aware multi-carrier multiuser indoor THz system is summarized in Fig. 5.2. It should be noted that the optimal strategy for the THz system should be obtained by joint optimization with carrier assignment, power allocation, and beamforming design across all the users, which is hard to achieve due to the high complexity. Therefore, a low-complexity suboptimal transmission strategy is proposed in this paper based on the THz channel characteristics.

5.3 Simulation Results

In this section, simulation results are provided to evaluate the performance of distance-aware adaptive beamforming with user grouping and antenna subarray selection for multiuser indoor THz communications.

Consider the indoor environment as [16, 19] with four users, who experience different propagation environments with different communication distances and QoS requirements. For illustration purpose, the transmission window is selected from 0.55 THz to 1 THz as shown in Fig. 1.2, and the sub-window bandwidth is set as $B = 5$ GHz. The detail

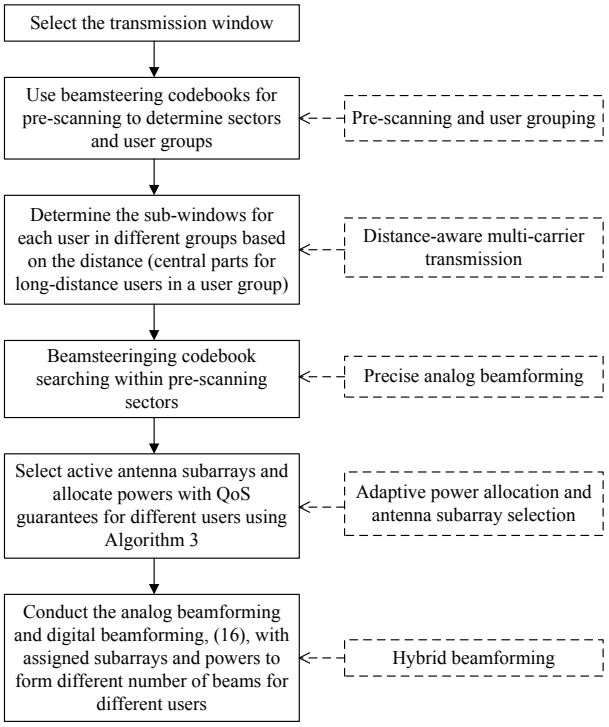

Fig. 5.2 The adaptive beamforming with antenna subarray selection and power allocation for distance-aware multi-carrier multiuser indoor THz system.

simulation parameters are listed in Table 5.4. Note that, the pre-scanning and user grouping is performed and given in Table 5.4, which we skip in the following simulation to simplify the simulation process. According to the pre-scanning in Table 5.4, user 1 and user 4 are in the same group. Thus, considering the distance-aware multi-carrier THz transmission, user 4, with longer distance, uses the central part of the transmission window as shown in Table 5.4, user 1 is then assigned the sides. For simplicity, we assume there exists three first-order reflected clusters and four second-order-reflection components in our simulation as [48]. Specifically, for the THz system, the antenna elements in each subarray are set as $M_t \times N_t = M_r \times N_r = 8 \times 8$, the antenna gains are set as $G_t = G_r = 20$ dBi, and the noise power, N_0, is set as -75 dBm.

As a benchmark, the antenna subarray selection with exhaustive search is studied.[15]

[15]The exhaustive search is based on the greedy subarray selection results, which searches all possible subarray combinations around the selected subarray number obtained from the greedy algorithm.

Table 5.4 Simulation Parameters

	User 1	User 2	User 3	User 4
Distance d (m)	1	5	5	10
Propagation environment	LOS	NLOS	LOS	LOS
User groups	Group 1	Group 2	Group 3	Group 1
Sub-windows $\mathcal{W}$ (THz)	0.6-0.7, 0.8-0.95	0.575-0.725 0.775-0.95	0.575-0.725 0.775-0.95	0.55-0.6 0.7-0.8 0.95-1

Adaptive beamforming with equal power allocation and random antenna subarray assignment are also investigated, respectively. Moreover, the non-distance-aware transmission with subarray selection and power allocation is considered as well, where the sub-windows, with the same number in Table 5.4, are randomly assigned to different users. Note that all the results are averaged over $5,000$ channel realizations.

In Fig. 5.3, we plot the average number of selected subarrays for the adaptive distance-aware multi-carrier transmission versus the available antenna subarray number. Here, the total transmit power constraints are set as $P = 8$ dBm, and the QoS requirements are $\tilde{R}_1 = \tilde{R}_2 = \tilde{R}_3 = \tilde{R}_4 = 0.15$ Tbps. As shown in Fig. 5.3, the adaptive beamforming policy can efficiently support Tbps transmission. Especially, the average number of selected subarrays decreases with the available subarray number first, and then converges. The reason is that, as the available subarray number increases, the selection degree of freedom increases at first and then saturates gradually. Additionally, the proposed antenna subarray selection algorithms could obtain almost the same performance as the optimal exhaustive search method with significantly reduced complexity. Particularly, the group-based algorithm outperforms the utility-based algorithm at the cost of slightly increased complexity. We can see from Fig. 5.3 that, the adaptive beamforming could achieve about 10% gain compared with the equal power allocation scheme, while this gain decreases with the available subarray number. Moreover, the adaptive beamforming could bring about 15%-20% improvement compared with the random antenna subarray assignment and the non-distance-aware

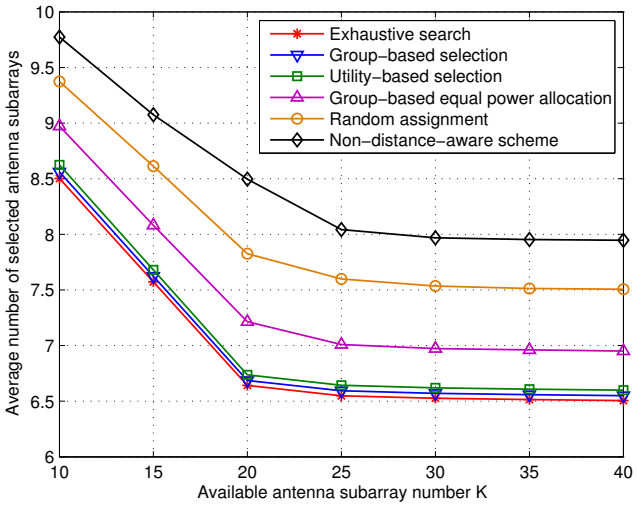

Fig. 5.3 Performance of the adaptive beamforming versus the available antenna subarray number.

scheme, respectively. Specifically, the non-distance-aware scheme achieves the worst performance, which indicates that the distance-aware carrier arrangement is of great importance in THz communications.

Fig. 5.4 demonstrates the performance of the adaptive policy for power allocation and antenna subarray selection as a function of the total transmit power constraints. Here, the available antenna subarray number is 15, and the QoS requirements are set as $\tilde{R}_1 = \tilde{R}_2 = \tilde{R}_3 = \tilde{R}_4 = 0.15$ Tbps. We can observe from Fig. 5.4 that, the required antenna subarray number generally decreases with the transmit power as we can imagine. The proposed adaptive algorithm can achieve near-optimal performance. Moreover, the adaptive beamforming can obtain about 10%-15% performance gains with low complexity compared with the equal power allocation and random assignment scheme. Particularly, these gains increase with the transmit power. Similar to Fig. 5.3, the non-distance-aware scheme uses the largest number of subarrays for QoS guarantee.

In Fig. 5.5, we compare the performance of the adaptive beamforming under different users' QoS demands, where $\tilde{R} = \tilde{R}_1 = \tilde{R}_2 = \tilde{R}_3 = \tilde{R}_4$. Here, the available antenna subarray number is 15, and the transmit power constraints are set as $P = 8$ dBm. We can observe from Fig. 5.5 that, the selected antenna subarray number increases with the

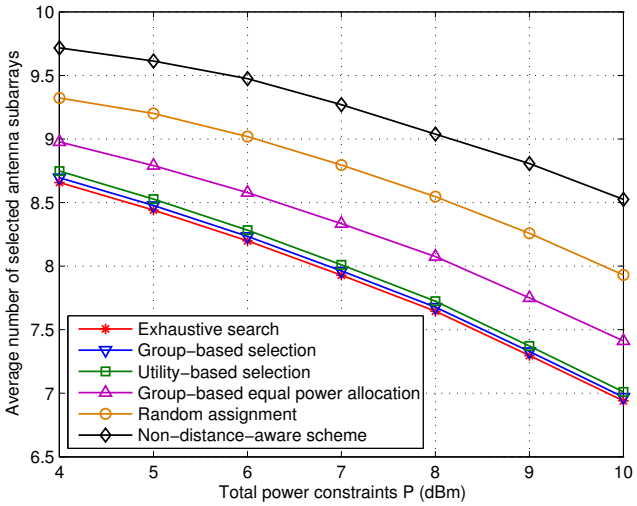

Fig. 5.4 Performance of the adaptive beamforming versus the transmit power constraints.

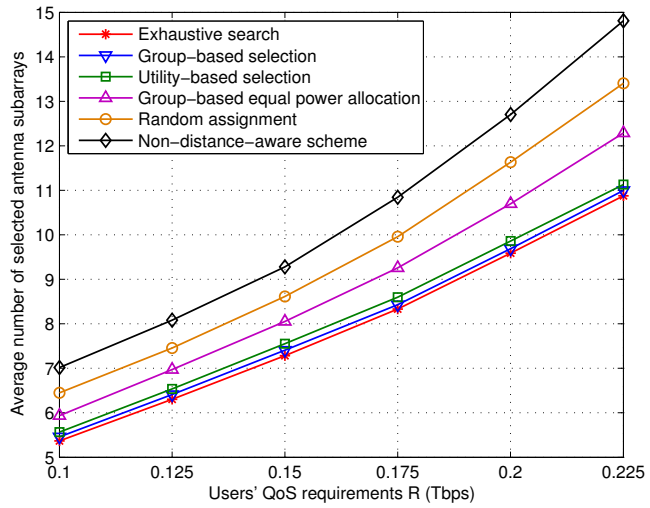

Fig. 5.5 Performance of the adaptive beamforming versus the QoS requirements.

QoS requirement. Furthermore, as the minimum rate constraint increases, the advantage of our proposed adaptive beamforming becomes larger. Specifically, the non-distance-aware scheme turns out to be more inferior for higher QoS demands.

5.4 Conclusions

This chapter has investigated multiuser wideband THz communications with multiple antenna subarrays. By exploiting the peculiarities of THz channels, we have designed a

hybrid beamforming scheme with distance-aware multi-carrier transmission for the system. Specifically, a two-step beamsteering searching and user grouping method has been proposed in the analog domain. Furthermore, an adaptive power allocation and antenna subarray selection policy for digital beamforming has been developed to reduce the cost of active RF circuits while ensuring users' QoS needs. Particularly, a utility-based and a group-based greedy antenna subarray selection algorithms with low complexity have been proposed. Simulation results show that the proposed adaptive beamforming can efficiently support THz transmission and provide QoS guarantees. In addition, the antenna subarray selection algorithms can obtain near-optimal performance with gains over other non-adaptive and non-distance-aware schemes.

CHAPTER 6

CONCLUSIONS

This thesis has provided a design guide on signal transmission and processing for mmWave and THz communications. Specifically, the higher-mmWave and THz bands, i.e., over 60 GHz, have been investigated. Several physical-layer solutions have been designed to capture the distinguished mmWave and THz characteristics.

In Chapter 2, we have compared the circuit configurations of the fully-connected and array-of-subarrays structures. Specifically, the Doherty PA has been adopted and the associated nonlinear system power consumption models with insertion loss has been developed. By capturing the characteristics of the mmWave and THz channels, we have designed different low-complexity hybrid beamforming schemes for the two structures. We have further compared the achievable rates of the two structures and shown that, with the insertion loss, the achievable rate of the array-of-subarrays structure is generally larger than that of the fully-connected structure. Moreover, we have proposed the optimal power control strategies for both structures to maximize the energy efficiency of the system and demonstrated that the energy efficiency of the array-of-subarrays structure outperforms that of the fully-connected structure.

In Chapter 3, we have investigated beamforming training for the array-of-subarrays structure to extract the dominant channel information. The impact of time-delay phase shifters has been captured. In particular, codebooks based on time-delay phase shifters have been defined and structured. Then, two multi-resolution time-delay codebooks have been designed through subarray coordination. One is built on adaptation of physical beam directions, and the other relies on dynamic approximation of beam patterns. Also, a low-complexity system implementation with modifications on the time-delay codebooks has been studied. Furthermore, based on the proposed codebooks, a hierarchical beamforming training strategy with reduced overhead has been developed to enable simultaneous training

for multiple users.

In Chapter 4, we have studied the performance limits and optimized array design for single-user indoor mmWave and THz communications with the array-of-subarrays structure. The S-V model has been modified to characterize the mmWave and THz channels. Then, we have analyzed the ergodic capacity with the hybrid beamforming for the system and obtain an upper bound. Furthermore, with the analysis of performance degradation due to uncertainty in phase shifters, we have provided a guideline on the design of antenna subarray size and number to support certain long-term data rate requirements at different distances.

At last, we have extended the study of the array-of-subarrays structure to wideband communications in Chapter 5. To capture the distance-frequency dependent characteristics of the THz channels, we have designed a hybrid beamforming scheme with distance-aware multi-carrier transmission, including analog beamforming for user grouping and interference cancellation and digital beamforming for antenna subarray selection and adaptive power allocation. In particular, two greedy subarray selection algorithms have been proposed.

This thesis has mainly focused on the transmission design for mmWave and THz communications. It can be further extended to the receiver design in future work. Also, other communication scenarios, such as relay systems, can be studied in the future.

APPENDIX A

PROOF FOR CHAPTER 2

A.1 Proof of Proposition 2.1

Using the virtual channel model [69, 103], the mmWave and THz channel of user j can be rewritten as

$$\mathbf{H}_j = \tilde{\mathbf{A}}_r \mathbf{H}_j^{\mathrm{v}} \tilde{\mathbf{A}}_t^*, \tag{A.1}$$

where $\tilde{\mathbf{A}}_t = [\mathbf{a}_t(KN, \tilde{\phi}_1), \mathbf{a}_t(KN, \tilde{\phi}_2), ..., \mathbf{a}_t(KN, \tilde{\phi}_{KN})]$ is the $KN \times KN$ matrix of the transmit array steering vectors in the virtual directions $\tilde{\phi}_q, q = 1, 2, ..., KN$ satisfying $\frac{2\pi r}{\lambda_c} \sin \tilde{\phi}_q = \frac{2\pi q}{KN}$, and $\tilde{\mathbf{A}}_r = [\mathbf{a}_r(M, \tilde{\theta}_1), \mathbf{a}_r(M, \tilde{\theta}_2), ..., \mathbf{a}_r(M, \tilde{\theta}_M)]$ is the $M \times M$ matrix of the receive array steering vectors in the virtual directions $\tilde{\theta}_m, m = 1, 2, ..., M$ satisfying $\frac{2\pi r}{\lambda_c} \sin \tilde{\theta}_m = \frac{2\pi m}{M}$. Specifically, $\tilde{\mathbf{A}}_t$ and $\tilde{\mathbf{A}}_r$ are both unitary discrete Fourier transform (DFT) matrices. And, $\mathbf{H}_j^{\mathrm{v}}$ is the virtual representation of the channel matrix associated with the virtual directions. Thus, the channel in (A.1) can be expressed as

$$\mathbf{H}_j = \sum_{i=1}^{KMN} \tilde{\alpha}_{j,i} \mathbf{a}_r(M, \tilde{\theta}_{j,i}) \mathbf{a}_t^*(KN, \tilde{\phi}_{j,i}), \tag{A.2}$$

where $|\tilde{\alpha}_{j,1}| \geq |\tilde{\alpha}_{j,2}| \geq ... \geq |\tilde{\alpha}_{j,KMN}|$ with $\tilde{\alpha}_{j,i}$ being the i-th largest virtual channel element of $\mathbf{H}_j^{\mathrm{v}}$ in magnitude, and $\tilde{\phi}_{j,i}$ and $\tilde{\theta}_{j,i}$ are the corresponding transmit and receive virtual directions, respectively. Due to the sparsity of the mmWave and THz channels, most of the virtual channel elements, $\tilde{\alpha}_{j,i}$, are equal to zero.

When $K = J$, from Algorithm 2.1, we can obtain the analog beamforming vectors for the fully-connected structure as $\mathbf{W}_a = [\frac{1}{\sqrt{KN}} \mathbf{a}_t(KN, \tilde{\phi}_{1,1}), \frac{1}{\sqrt{KN}} \mathbf{a}_t(KN, \tilde{\phi}_{2,1}), ..., \frac{1}{\sqrt{KN}} \mathbf{a}_t(KN, \tilde{\phi}_{K,1})]$ and $\mathbf{v}_{j,a} = \frac{1}{\sqrt{M}} \mathbf{a}_r(M, \tilde{\theta}_{j,1})$. Then, the effective channel of user j for the fully-connected structure is given by

$$\hat{\mathbf{h}}_{j,a}^T = \mathbf{v}_{j,a}^* \mathbf{H}_j \mathbf{W}_a = \sqrt{KMN} [\zeta_{j,1}^a, \zeta_{j,2}^a, ..., \zeta_{j,K}^a]. \tag{A.3}$$

On the other hand, from Algorithm 2.2, we can obtain the analog beamforming vectors for the array-of-subarrays structure as

$$\mathbf{W}_b = \begin{bmatrix} \frac{1}{\sqrt{N}}\mathbf{a}_t(N,\tilde{\phi}_{1,1}) & \mathbf{0} & \cdots & \mathbf{0} \\ \mathbf{0} & \frac{1}{\sqrt{N}}\mathbf{a}_t(N,\tilde{\phi}_{2,1}) & \cdots & \mathbf{0} \\ \vdots & \vdots & \vdots & \vdots \\ \mathbf{0} & \mathbf{0} & \cdots & \frac{1}{\sqrt{N}}\mathbf{a}_t(N,\tilde{\phi}_{K,1}) \end{bmatrix}, \tag{A.4}$$

and $\mathbf{v}_{j,b} = \frac{1}{\sqrt{M}}\mathbf{a}_r(M,\tilde{\theta}_{j,1})$. Notably, $\mathbf{W}_b^*\mathbf{W}_b = \mathbf{I}$. Thus, the effective channel of user j for the array-of-subarrays structure is

$$\hat{\mathbf{h}}_{j,b}^T = \mathbf{v}_{j,b}^*\mathbf{H}_j\mathbf{W}_b = \sqrt{MN}[\zeta_{j,1}^b, \zeta_{j,2}^b, ..., \zeta_{j,K}^b], \tag{A.5}$$

where $\zeta_{j,k}^b = \zeta_{j,k}^a + \frac{1}{N}\sum_{i=2}^{KMN}\tilde{\alpha}_{j,i}\mathbb{1}(\tilde{\theta}_{j,i} = \tilde{\theta}_{j,1})\mathbb{1}(\tilde{\phi}_{j,i} \neq \tilde{\phi}_{k,1})\Omega(\frac{r}{\lambda_c}\sin\tilde{\phi}_{k,1} - \frac{r}{\lambda_c}\sin\tilde{\phi}_{j,i})$, with $\mathbb{1}(\cdot)$ as the indicator function and $\Omega(x) = \frac{1-e^{j2\pi Nx}}{1-e^{j2\pi x}} = \frac{\sin\pi Nx}{\sin\pi x}e^{j\pi(N-1)x}$. Thus, $|\zeta_{j,k}^b|^2 \geq |\zeta_{j,k}^a|^2$, for $j \in \mathcal{J}, k \in \mathcal{K}$. Then, according to [46], the difference between the achievable rates of the two structures with the insertion loss can be calculated as

$$\begin{aligned} R_j^a - R_j^b &= B\log_2\left(1 + \frac{\frac{P_t^a}{J\sigma_j^2}KMN}{\left((\hat{\mathbf{D}}_a\hat{\mathbf{D}}_a^*)^{-1}\hat{\mathbf{D}}_a\mathbf{W}_a^*\mathbf{W}_a\hat{\mathbf{D}}_a^*(\hat{\mathbf{D}}_a\hat{\mathbf{D}}_a^*)^{-1}\right)_{j,j}}\right) \\ &\quad - B\log_2\left(1 + \frac{\frac{P_t^b}{J\sigma_j^2}MN}{\left((\hat{\mathbf{D}}_b\hat{\mathbf{D}}_b^*)^{-1}\hat{\mathbf{D}}_b\mathbf{W}_b^*\mathbf{W}_b\hat{\mathbf{D}}_b^*(\hat{\mathbf{D}}_b\hat{\mathbf{D}}_b^*)^{-1}\right)_{j,j}}\right) \\ &= B\log_2\left(1 + \frac{\frac{\tilde{P}_s}{K^2NJ\sigma_j^2}KMN}{\left((\hat{\mathbf{D}}_a\hat{\mathbf{D}}_a^*)^{-1}\hat{\mathbf{D}}_a\mathbf{W}_a^*\mathbf{W}_a\hat{\mathbf{D}}_a^*(\hat{\mathbf{D}}_a\hat{\mathbf{D}}_a^*)^{-1}\right)_{j,j}}\right) \\ &\quad - B\log_2\left(1 + \frac{\frac{\tilde{P}_s}{NJ\sigma_j^2}MN}{(\hat{\mathbf{D}}_b\hat{\mathbf{D}}_b^*)_{j,j}^{-1}}\right) \qquad (A.6) \\ &\leq B\log_2\left(1 + \frac{\frac{\tilde{P}_s}{J\sigma_j^2}\frac{M}{K}}{(\hat{\mathbf{D}}_a\hat{\mathbf{D}}_a^*)_{j,j}^{-1}}\right) - B\log_2\left(1 + \frac{\frac{\tilde{P}_s}{J\sigma_j^2}M}{(\hat{\mathbf{D}}_a\hat{\mathbf{D}}_a^*)_{j,j}^{-1}}\right) \qquad (A.7) \\ &\leq 0, \end{aligned}$$

where $(\hat{\mathbf{D}}_a)_{j,k} = \zeta^a_{j,k}$, $(\hat{\mathbf{D}}_b)_{j,k} = \zeta^b_{j,k}$, and $\tilde{P}_s \triangleq P_s - L_{PS} + G_{PA}$. Specifically, (A.6) is resulting from the insertion loss in (2.20), (2.22), and (2.21). Since

$$\begin{aligned}\left((\hat{\mathbf{D}}_a\hat{\mathbf{D}}_a^*)^{-1}\hat{\mathbf{D}}_a\mathbf{W}_a^*\mathbf{W}_a\hat{\mathbf{D}}_a^*(\hat{\mathbf{D}}_a\hat{\mathbf{D}}_a^*)^{-1}\right)_{j,j} &\geq \left((\hat{\mathbf{D}}_a\hat{\mathbf{D}}_a^*)^{-1}\hat{\mathbf{D}}_a\mathbf{I}\hat{\mathbf{D}}_a^*(\hat{\mathbf{D}}_a\hat{\mathbf{D}}_a^*)^{-1}\right)_{j,j} \\ &= (\hat{\mathbf{D}}_a\hat{\mathbf{D}}_a^*)^{-1}_{j,j}, \end{aligned} \tag{A.8}$$

(A.7) then could be obtained from the relation between $\zeta^a_{j,k}$ and $\zeta^b_{j,k}$ as in (A.5). In addition, when high SNR condition is considered, i.e., $\frac{\tilde{P}_s}{J\sigma_j^2} \gg 1$, we can obtain from (A.7) that,

$$R_j^b - R_j^a \geq B\log_2\left(\frac{\frac{\tilde{P}_s}{J\sigma_j^2}M}{(\hat{\mathbf{D}}_a\hat{\mathbf{D}}_a^*)^{-1}_{j,j}}\right) - B\log_2\left(\frac{\frac{\tilde{P}_s}{J\sigma_j^2}\frac{M}{K}}{(\hat{\mathbf{D}}_a\hat{\mathbf{D}}_a^*)^{-1}_{j,j}}\right) = B\log_2 K = B\log_2 J. \tag{A.9}$$

A.2 Proof of Lemma 2.1

First, assume c_1 and c_2 are fixed for $P_t > 0$. The partial derivative of ξ_{EE} in (2.43) with respect to P_t is given by

$$\begin{aligned}\frac{\partial \xi_{EE}}{\partial P_t} &= \frac{B}{2\sqrt{P_t}(c_1\sqrt{P_t}+c_2)^2}\left[\frac{2}{\ln 2}(c_1P_t + c_2\sqrt{P_t})\sum_{j=1}^{J}\frac{\beta_j}{1+\beta_jP_t} - c_1\sum_{j=1}^{J}\log_2(1+\beta_jP_t)\right] \\ &= \frac{B\sum_{j=1}^{J}\frac{\beta_j}{1+\beta_jP_t}}{2\sqrt{P_t}(c_1\sqrt{P_t}+c_2)^2}\left[\frac{2}{\ln 2}(c_1P_t + c_2\sqrt{P_t}) - \frac{c_1\sum_{j=1}^{J}\log_2(1+\beta_jP_t)}{\sum_{j=1}^{J}\frac{\beta_j}{1+\beta_jP_t}}\right], \end{aligned} \tag{A.10}$$

where $\sum_{j=1}^{J}\frac{\beta_j}{1+\beta_jP_t} > 0$ for $P_t > 0$. Define

$$\Xi(P_t) \triangleq \frac{2}{\ln 2}(c_1P_t + c_2\sqrt{P_t}) - \frac{c_1\sum_{j=1}^{J}\log_2(1+\beta_jP_t)}{\sum_{j=1}^{J}\frac{\beta_j}{1+\beta_jP_t}}. \tag{A.11}$$

Specifically,

$$\lim_{P_t\to 0}\Xi(P_t) \simeq \frac{2}{\ln 2}(c_1P_t + c_2\sqrt{P_t}) - \frac{c_1\sum_{j=1}^{J}\beta_jP_t}{\sum_{j=1}^{J}\beta_j} = \frac{2}{\ln 2}(c_1P_t + c_2\sqrt{P_t}) - c_1P_t > 0, \tag{A.12}$$

and

$$\lim_{P_t \to +\infty} \Xi(P_t) \simeq \frac{2}{\ln 2}(c_1 P_t + c_2 \sqrt{P_t}) - \frac{c_1 P_t \sum_{j=1}^{J} \log_2(\beta_j P_t)}{J} = -\infty < 0. \tag{A.13}$$

Hence, $\Xi(P_t)$ has at lease one zero point for $P_t > 0$. Moreover, $\frac{2}{\ln 2}(c_1 P_t + c_2 \sqrt{P_t})$ and $\frac{c_1 \sum_{j=1}^{J} \log_2\left(1+\beta_j P_t\right)}{\sum_{j=1}^{J} \frac{\beta_j}{1+\beta_j P_t}}$ as well as their derivatives are smooth and monotonically increasing for $P_t > 0$, and

$$\frac{2}{\ln 2}(c_1 P_t + c_2 \sqrt{P_t})\Big|_{P_t=0} = \frac{c_1 \sum_{j=1}^{J} \log_2\left(1+\beta_j P_t\right)}{\sum_{j=1}^{J} \frac{\beta_j}{1+\beta_j P_t}}\Big|_{P_t=0} = 0. \tag{A.14}$$

Thus, there exists at most one zero point for $\Xi(P_t)$ with $P_t > 0$. Consequently, there is exactly one zero point of $\Xi(P_t)$, which means ξ_{EE} has one exclusive stationary point, $\hat{P}_t$, obtained at $\frac{\partial \xi_{EE}}{\partial P_t} = 0$. In particular, $\frac{\partial \xi_{EE}}{\partial P_t} > 0$ when $0 < P_t < \hat{P}_t$, and $\frac{\partial \xi_{EE}}{\partial P_t} < 0$ when $P_t > \hat{P}_t$. Therefore, ξ_{EE} is a quasi-concave function for fixed c_1 and c_2. In fact, c_1 and c_2 are constant with different values under different conditions as in (2.29), thus, ξ_{EE} is a piecewise quasi-concave function of P_t for $P_t > 0$.

A.3 Proof of Theorem 2.1

Theorem 2.1 is a direct deduction from Lemma 2.1. For example, for the fully-connected structure, when $a_1 < P_t \leq a_2$, if $\hat{P}_t < a_1$, the optimal transmit power is given by $P_t^\star = a_1$ because ξ_{EE} is monotonically decreasing for $P_t \in (a_1, a_2]$ according to Lemma 2.1. If $\hat{P}_t > a_2$, the optimal transmit power is given by $P_t^\star = a_2$ because ξ_{EE} is monotonically increasing for $P_t \in (a_1, a_2]$. Otherwise, if $a_1 < \hat{P}_t \leq a_2$, the optimal transmit power is exactly $P_t^\star = \hat{P}_t$. Similarly, the optimal transmit power for other conditions can be obtained using the same method.

APPENDIX B

PROOF FOR CHAPTER 4

B.1 Useful Lemmas

Lemma B.1 (Campbell's theorem [104]) *Let V be a point process on a real space $S \subseteq \mathbb{R}$ with rate ϱ_V. Then, for a real-valued measurable function $u : S \to \mathbb{R}$, the expectation of the random variable $\sum_{v \in V} u(v)$ satisfies*

$$\mathbb{E}[\sum_{v \in V} u(v)] = \int_S u(v)\varrho_v(v)dv. \tag{B.1}$$

Lemma B.2 ([104]) *The S-V channel model consists of a sequence of Poisson processes. The total rate for the entire process is given by*

$$\rho(t) = \Lambda + \lambda + \Lambda\lambda t, \tag{B.2}$$

where Λ and λ are the rates of cluster arrivals and ray arrivals in each cluster, respectively. Note that this rate is a function of the propagation time.

B.2 The Calculation of the Expectation of Total Multi-path Power Gain

As stated before, the multi-path arrivals contain three parts. For the first ray of the first cluster at T_0, by definition in (4.6), we have

$$\mathbb{E}[|\alpha_{00}|^2] = \Psi_0. \tag{B.3}$$

As for the cluster arrivals, the arriving rate is Λ. By using the *Campbell's* theorem in Appendix B.1, the expectation of the power gain is

$$\mathbb{E}[\sum_{i=1}^{N_{clu}-1} |\alpha_{i0}|^2] = \mathbb{E}\Big[\sum_{i=1}^{N_{clu}-1} \mathbb{E}[|\alpha_{i0}|^2|T_i]\Big] = \int_0^{T_s} \Psi_0 e^{-\frac{t}{\Gamma}} \Lambda \, dt = \Psi_0 \Lambda\Gamma(1 - e^{-\frac{T_s}{\Gamma}}). \tag{B.4}$$

Furthermore, the ray arrivals in all the clusters can be written as the sum of the rays in the first cluster with rate λ and the rays of the other clusters. As we know, the latter one is a

combination of cluster arrival process with rate Λ and ray arrival process with rate λ. Thus, by applying the *Campbell's* theorem, the expectation of the power gain can be calculated as

$$\begin{aligned}
\mathbb{E}[\sum_{i=0}^{N_{clu}-1}\sum_{l=1}^{N_{ray}^i-1}|\alpha_{il}|^2] &= \mathbb{E}[\sum_{l=1}^{N_{ray}^0-1}|\alpha_{0l}|^2] + \mathbb{E}[\sum_{i=1}^{N_{clu}-1}\sum_{l=1}^{N_{ray}^i-1}|\alpha_{il}|^2] \\
&= \mathbb{E}\Big[\sum_{l=1}^{N_{ray}^0-1}\mathbb{E}[|\alpha_{0l}|^2|\tau_{0l}]\Big] + \mathbb{E}\Big[\sum_{i=1}^{N_{clu}-1}\mathbb{E}\Big[\sum_{l=1}^{N_{ray}^i-1}\mathbb{E}[|\alpha_{il}|^2|T_i,\tau_{il}]\Big]\Big] \\
&= \int_0^{T_s}\Psi_0 e^{-\frac{\tau}{\gamma}}\lambda\, d\tau + \int_0^{T_s}\int_t^{T_s}\Psi_0 e^{-\frac{t}{\Gamma}}e^{-\frac{\tilde{\tau}-t}{\gamma}}\lambda\Lambda\, d\tilde{\tau}dt \\
&= \Psi_0\lambda\gamma(1-e^{-\frac{T_s}{\gamma}}) + \Psi_0\Lambda\lambda\Gamma\gamma + \frac{\Psi_0\Lambda\lambda\Gamma\gamma}{\Gamma-\gamma}(\gamma e^{-\frac{T_s}{\gamma}} - \Gamma e^{-\frac{T_s}{\Gamma}}). \quad \text{(B.5)}
\end{aligned}$$

B.3 The Calculation of the Angle Related Term (4.18)

Since the antenna sectors are small, the associated radiation pattern of the subarray mainly falls in the central part of the main lobe. Considering $\left|\frac{\sin Vx}{\sin x}\right| \le V$ for small x, we can further obtain from (4.12) and (4.13) that $|A_t^{eq}(\phi,\theta)|^2 \le M_tN_t$ and $|A_r^{eq}(\phi,\theta)|^2 \le M_rN_r$. Hence, for the angle related term (4.18), due to the independence between the distribution of AoD and AoA, we have

$$\begin{aligned}
&\mathbb{E}[|G_t(\phi_{il}^t,\theta_{li}^t)G_r(\phi_{il}^r,\theta_{il}^r)A_r^{eq}(\phi_{il}^r,\theta_{il}^r)A_t^{eq}(\phi_{il}^t,\theta_{il}^t)|^2] \\
=\ &\mathbb{E}[|G_t(\phi_{il}^t,\theta_{li}^t)|^2|G_r(\phi_{il}^r,\theta_{il}^r)|^2|A_r^{eq}(\phi_{il}^r,\theta_{il}^r)|^2|A_t^{eq}(\phi_{il}^t,\theta_{il}^t)|^2] \\
=\ &\mathbb{E}[|G_t(\phi_{il}^t,\theta_{li}^t)|^2|A_t^{eq}(\phi_{il}^t,\theta_{il}^t)|^2]\mathbb{E}[|G_r(\phi_{il}^r,\theta_{il}^r)|^2|A_r^{eq}(\phi_{il}^r,\theta_{il}^r)|^2] \\
\le\ &M_tM_rN_tN_r\mathbb{E}[|G_t(\phi_{il}^t,\theta_{il}^t)|^2]\mathbb{E}[|G_r(\phi_{il}^r,\theta_{il}^r)|^2]. \quad \text{(B.6)}
\end{aligned}$$

Taking into account the angle distribution in (4.7) and (4.8), we can obtain the antenna gain at AP as

$$\begin{aligned}
\mathbb{E}[|G_t(\phi_{il}^t,\theta_{il}^t)|^2] &= \int_{-\frac{\pi}{2}}^{\frac{\pi}{2}}\int_{\theta_{min}^t-\Theta^t}^{\theta_{max}^t-\Theta^t}\frac{GMM_t(\vartheta^t)}{\pi}\int_{-\pi}^{\pi}\int_{\phi_{min}^t-\Phi^t}^{\phi_{max}^t-\Phi^t}\frac{G_{t0}GMM_t(\varphi^t)}{2\pi}d\varphi^t d\Phi^t d\vartheta^t d\Theta^t \\
&= \frac{G_{t0}}{2\pi^2}[w_{1,\varphi}^t\mathcal{G}(\sigma_{1,\varphi}^t,\phi_{min}^t,\phi_{max}^t,\pi) + w_{2,\varphi}^t\mathcal{G}(\sigma_{2,\varphi}^t,\phi_{min}^t,\phi_{max}^t,\pi)] \\
&\quad \times[w_{1,\vartheta}^t\mathcal{G}(\sigma_{1,\vartheta}^t,\theta_{min}^t,\theta_{max}^t,\frac{\pi}{2}) + w_{2,\vartheta}^t\mathcal{G}(\sigma_{2,\vartheta}^t,\theta_{min}^t,\theta_{max}^t,\frac{\pi}{2})], \quad \text{(B.7)}
\end{aligned}$$

where $\mathcal{G}(\sigma, x, y, z)$ is defined in (4.22).

Similarly, the antenna gain at the receive side can be expressed as

$$\begin{aligned}\mathbb{E}[|G_r(\phi^r_{il}, \theta^r_{il})|^2] &= \frac{G_{r0}}{2\pi^2}[w^r_{1,\varphi}\mathcal{G}(\sigma^r_{1,\varphi}, \phi^r_{min}, \phi^r_{max}, \pi) + w^r_{2,\varphi}\mathcal{G}(\sigma^r_{2,\varphi}, \phi^r_{min}, \phi^r_{max}, \pi)] \\ &\quad \times[w^r_{1,\vartheta}\mathcal{G}(\sigma^r_{1,\vartheta}, \theta^r_{min}, \theta^r_{max}, \frac{\pi}{2}) + w^r_{2,\vartheta}\mathcal{G}(\sigma^r_{2,\vartheta}, \theta^r_{min}, \theta^r_{max}, \frac{\pi}{2})]. \quad \text{(B.8)}\end{aligned}$$

REFERENCES

[1] S. Cherry, "Edholm's law of bandwidth," *IEEE Spectrum*, vol. 41, no. 7, pp. 58–60, Jul. 2004.

[2] Z. Pi and F. Khan, "An introduction to millimeter-wave mobile broadband systems," *IEEE Commun. Mag.*, vol. 49, no. 6, pp. 101–107, Jun. 2011.

[3] T. S. Rappaport, S. Sun, R. Mayzus, H. Zhao, Y. Azar, K. Wang, G. N. Wong, J. K. Schulz, M. Samimi, and F. Gutierrez, "Millimeter wave mobile communications for 5G cellular: It will work!" *IEEE Access*, vol. 1, pp. 335–349, May 2013.

[4] S. Rangan, T. S. Rappaport, and E. Erkip, "Millimeter wave cellular wireless networks: Potentials and challenges," *Proc. IEEE*, vol. 102, no. 3, pp. 366–385, Feb. 2014.

[5] S. Sun, T. S. Rappaport, R. W. Heath, A. Nix, and S. Rangan, "MIMO for millimeter wave wireless communications: Beamforming, spatial multiplexing, or both?" *IEEE Commun. Mag.*, vol. 52, no. 12, pp. 110–121, Dec. 2014.

[6] L. Wei, R. Q. Hu, Y. Qian, and G. Wu, "Key elements to enable millimeter wave communications for 5G wireless systems," *IEEE Wireless Commun.*, vol. 21, no. 6, pp. 136–143, Dec. 2014.

[7] R. Piesiewicz, T. Kleine-Ostmann, N. Krumbholz, D. Mittleman, M. Koch, J. Schoebel, and T. Kürner, "Short-range ultra-broadband Terahertz communications: Concepts and perspectives," *IEEE Antennas and Propag. Mag.*, vol. 49, no. 6, pp. 24–39, Dec. 2007.

[8] H. Song and T. Nagatsuma, "Present and future of Terahertz communications," *IEEE Trans. Terahertz Sci. and Tech.*, vol. 1, no. 1, pp. 256–263, Sep. 2011.

[9] K.-C. Huang and Z. Wang, "Terahertz Terabit wireless communication," *IEEE Microwave Mag.*, vol. 12, no. 4, pp. 108–116, Jun. 2011.

[10] J. Federici and L. Moeller, "Review of Terahertz and subterahertz wireless communication," *J. Appl. Phys.*, vol. 107, no. 1, p. 111101, Jun. 2010.

[11] I. F. Akyildiz, J. M. Jornet, and C. Han, "Terahertz band: Next frontier for wireless communications," *Physical Commun.*, vol. 12, no. 2, pp. 16–32, Sep. 2014.

[12] C. Lin and G. Y. Li, "Terahertz communications: An array-of-subarrays solution," *IEEE Commun. Mag.*, vol. 54, no. 12, pp. 124–131, Dec. 2016.

[13] H. Xu, V. Kukshya, and T. S. Rappaport, "Spatial and temporal characteristics of 60-GHz indoor channels," *IEEE J. Sel. Areas Commun.*, vol. 20, no. 3, pp. 620–630, Apr. 2002.

[14] M. R. Akdeniz, Y. Liu, M. K. Samimi, S. Sun, S. Rangan, T. S. Rappaport, and E. Erkip, "Millimeter wave channel modeling and cellular capacity evaluation," *IEEE J. Sel. Areas Commun.*, vol. 32, no. 6, pp. 1164–1179, Jun. 2014.

[15] S. Priebe and T. Kürner, "Stochastic modeling of THz indoor radio channels," *IEEE Trans. Wireless Commun.*, vol. 12, no. 9, pp. 4445–4455, Sep. 2013.

[16] S. Priebe, M. Kannicht, M. Jacob, and T. Kürner, "Ultra broadband indoor channel measurements and calibrated ray tracing propagation modeling at THz frequencies," *J. Commu. Netw.*, vol. 15, no. 6, pp. 547–558, Dec. 2013.

[17] C. Jansen, S. Priebe, C. Moller, M. Jacob, H. Dierke, M. Koch, and T. Kürner, "Diffuse scattering from rough surfaces in THz communication channels," *IEEE Trans. Terahertz Sci. and Tech.*, vol. 1, no. 2, pp. 462–472, Nov. 2011.

[18] J. M. Jornet and I. F. Akyildiz, "Channel modeling and capacity analysis for electromagnetic wireless nanonetworks in the Terahertz band," *IEEE Trans. Wireless Commun.*, vol. 10, no. 10, pp. 3211–3221, Oct. 2011.

[19] C. Han, A. O. Bicen, and I. F. Akyildiz, "Multi-ray channel modeling and wideband characterization for wireless communications in the THz band," *IEEE Trans. Wireless Commun.*, vol. 14, no. 10, pp. 2402–2412, May 2015.

[20] S. Priebe, M. Jacob, and T. Kürner, "Angular and RMS delay spread modeling in view of THz indoor communication systems," *Radio Sci.*, vol. 49, no. 3, pp. 242–251, Mar. 2014.

[21] T. S. Rappaport, J. N. Murdock, and F. Gutierrez, "State of the art in 60-GHz integrated circuits and systems for wireless communications," *Proc. IEEE*, vol. 99, no. 8, pp. 1390–1436, Aug. 2011.

[22] S. J. B. Yoo, R. P. Scott, D. J. Geisler, N. K. Fontaine, and F. M. Soares, "Terahertz information and signal processing by RF-photonics," *IEEE Trans. Terahertz Sci. and Tech.*, vol. 2, no. 2, pp. 167–176, Mar. 2012.

[23] P. Y. Chen, C. Argyropoulos, and A. Alù, "Terahertz antenna phase shifters using integrally-gated graphene transmission-lines," *IEEE Trans. Antennas Propag.*, vol. 61, no. 4, pp. 1528–1537, 2013.

[24] C.-Y. Chen, C.-F. Hsieh, Y.-F. Lin, R.-P. Pan, and C.-L. Pan, "Magnetically tunable room-temperature 2π liquid crystal Terahertz phase shifter," *Opt. Exp.*, vol. 12, no. 12, pp. 2625–2630, Jun. 2004.

[25] Y. Wu, X. Ruan, C. H. Chen, Y. J. Shin, Y. Lee, J. Niu, J. Liu, Y. Chen, K. L. Yang, X. Zhang, J. H. Ahn, and H. Yang, "Graphene/liquid crystal based Terahertz phase shifters," *Opt. Exp.*, vol. 21, no. 18, pp. 21 395–21 402, Sep. 2013.

[26] J. M. Jornet and I. F. Akyildiz, "Graphene-based plasmonic nano-antenna for Terahertz band communication in nanonetworks," *IEEE J. Sel. Areas Commun.*, vol. 31, no. 12, pp. 685–694, Dec. 2013.

[27] W. Roh, J.-Y. Seol, J. Park, B. Lee, J. Lee, Y. Kim, J. Cho, K. Cheun, and F. Aryanfar, "Millimeter-wave beamforming as an enabling technology for 5G cellular communications: Theoretical feasibility and prototype results," *IEEE Commun. Mag.*, vol. 52, no. 2, pp. 106–113, Feb. 2014.

[28] A. Alkhateeb, J. Mo, N. Gonzlez-Prelcic, and J. R. W. Heath, "MIMO precoding and combining solutions for millimeter-wave systems," *IEEE Commun. Mag.*, vol. 52, no. 12, pp. 122–131, Dec. 2014.

[29] S. Kutty and D. Sen, "Beamforming for millimeter wave communications: An inclusive survey," *IEEE Commun. Surv. Tutor.*, vol. 18, no. 2, pp. 949–973, Second Quarter 2016.

[30] J. R. W. Heath, N. González-Prelcic, S. Rangan, W. Roh, and A. Sayeed, "An overview of signal processing techniques for millimeter wave MIMO systems," *IEEE J. Sel. Signal Process.*, vol. 10, no. 3, pp. 436–453, Apr. 2016.

[31] J. H. Brady and A. M. Sayeed, "Wideband communication with high-dimensional arrays: New results and transceiver architectures," in *Proc. IEEE ICC Workshop*, London, UK, Jun. 2015, pp. 1042–1047.

[32] H. Hashemi, T.-S. Chu, and J. Roderick, "Integrated true-time-delay based ultrawideband array processing," *IEEE Commun. Mag.*, vol. 46, no. 9, pp. 162–172, Sep. 2008.

[33] T.-S. Chu and H. Hashem, "True-time-delay-based multi-beam arrays," *IEEE Trans. Microw. Theory Tech.*, vol. 61, no. 8, pp. 3072–3082, Aug. 2013.

[34] Z. Cao, Q. Ma, A. B. Smolders, Y. Jiao, M. J. Wale, H. W. C. W. Oh, and A. M. J. Koonen, "Advanced integration techniques on broadband millimeter-wave beam steering for 5G wireless networks and beyond," *IEEE J. Quant. Electron.*, vol. 52, no. 1, p. 0600620, Jan. 2016.

[35] S. Park and S. Jeon, "A 15-40 GHz CMOS true-time delay circuit for UWB multi-antenna systems," *IEEE Microw. Compon. Lett*, vol. 23, no. 3, pp. 149–157, Mar. 2013.

[36] Q. Ma, D. M. W. Leenaerts, and P. G. M. Baltus, "Silicon-based true-time-delay phased-array front-ends at Ka-band," *IEEE Trans. Microw. Theory Tech.*, vol. 63, no. 9, pp. 2942–2952, Sep. 2015.

[37] T. Nitsche, C. Cordeiro, A. B. Flores, E. W. Knightly, E. Perahia, and J. C. Widmer, "IEEE 802.11ad: Directional 60 GHz communication for multi-Gigabit-per-second Wi-Fi," *IEEE Commun. Mag.*, vol. 52, no. 12, pp. 132–141, Dec. 2014.

[38] T. Baykas, C.-S. Sum, Z. Lan, J. Wang, M. A. Rahman, H. Harada, and S. Kato, "IEEE 802.15.3c: The first IEEE wireless standard for data rates over 1 Gb/s," *IEEE Commun. Mag.*, vol. 49, no. 7, pp. 114–121, Jul. 2011.

[39] J. Wang, Z. Lan, C. Pyo, T. Baykas, C. Sum, M. Rahman, J. Gao, R. Funada, F. Kojima, H. Harada, and S. Kato, "Beam codebook based beamforming protocol for multi-gbps millimeter-wave WPAN systems," *IEEE J. Sel. Areas Commun.*, vol. 27, no. 8, pp. 1390–1399, Oct. 2009.

[40] Y. M. Tsang, A. S. Y. Poon, and S. Addepalli, "Coding the beams: Improving beamforming training in mmWave communication system," in *Proc. IEEE Globecom*, Houston, TX, USA, Dec. 2011, pp. 1–6.

[41] S. Hur, T. Kim, D. J. Love, J. V. Krogmeier, T. A. Thomas, and A. Ghosh, "Millimeter wave beamforming for wireless backhaul and access in small cell networks," *IEEE Trans. Commun.*, vol. 61, no. 10, pp. 4391–4403, Sep. 2013.

[42] V. Raghavan, J. Cezanne, S. Subramanian, A. Sampath, and O. Koymen, "Beamforming tradeoffs for initial UE discovery in millimeter-wave MIMO systems," *IEEE J. Sel. Signal Process.*, vol. 10, no. 3, pp. 543–559, Apr. 2016.

[43] O. E. Ayach, S. Rajagopal, S. Abu-Surra, Z. Pi, and R. W. Heath, "Spatially sparse precoding in millimeter wave MIMO systems," *IEEE Trans. Wireless Commun.*, vol. 13, no. 3, pp. 1499–1513, Mar. 2014.

[44] A. Alkhateeb, O. E. Ayach, and J. R. W. Heath, "Channel estimation and hybrid precoding for millimeter wave cellular systems," *IEEE J. Sel. Signal Process.*, vol. 8, no. 5, pp. 831–846, Oct. 2014.

[45] F. Sohrabi and W. Yu, "Hybrid digital and analog beamforming design for large-scale antenna arrays," *IEEE J. Sel. Signal Process.*, vol. 10, no. 3, pp. 501–513, Apr. 2016.

[46] A. Alkhateeb, G. Leus, and J. R. W. Heath, "Limited feedback hybrid precoding for multi-user millimeter wave systems," *IEEE Trans. Wireless Commun.*, vol. 14, no. 11, pp. 6481–6494, Nov. 2015.

[47] A. Alkhateeb, G. Leus, and R. W. H. Jr, "Compressed-sensing based multi-user millimeter wave systems: How many measurements are needed?" in *Proc. IEEE ICASSP*, Brisbane, Australia, Apr. 2015, pp. 2909–2913.

[48] E. Torkildson, U. Madhow, and M. Rodwell, "Indoor millimeter wave MIMO: Feasibility and performance," *IEEE Trans. Wireless Commun.*, vol. 10, no. 12, pp. 4150–4160, Dec. 2011.

[49] O. E. Ayach, R. W. H. Jr., S. Rajagopal, and Z. Pi, "Multimode precoding in millimeter wave mimo transmitters with multiple antenna sub-arryas," in *Proc. IEEE Globecom*, Atlanta, GA, USA, Dec. 2013, pp. 3476–3480.

[50] R. A. Stirling-Gallacher and M. S. Rahman, "Linear MU-MIMO pre-coding algorithms for a millimeter wave communication system using hybrid beam-forming," in *Proc. IEEE ICC*, Sydney, NSW, Australia, Jun. 2014, pp. 5449–5454.

[51] S.-H. Wu, L.-K. Chiu, K.-Y. Lin, and T.-H. Chang, "Robust hybrid beamforming with phased antenna arrays for downlink SDMA in indoor 60GHz channels," *IEEE Trans. Wireless Commun.*, vol. 12, no. 9, pp. 4542–4557, Sep. 2013.

[52] J. Singh and S. Ramakrishna, "On the feasibility of beamforming in millimeter wave communication systems with multiple antenna subarrays," *IEEE Trans. Wireless Commun.*, vol. 14, no. 5, pp. 2670–2683, May 2015.

[53] X. Huang, Y. J. Guo, and J. D. Bunton, "A hybrid adaptive antenna array," *IEEE Trans. Wireless Commun.*, vol. 9, no. 5, pp. 1770–1779, May 2010.

[54] X. Huang and Y. J. Guo, "Frequency-domain AoA estimation and beamforming with wideband hybrid arrays," *IEEE Trans. Wireless Commun.*, vol. 10, no. 8, pp. 2543–2553, Jun. 2011.

[55] J. Zhang, X. Huang, V. Dyadyuk, and Y. J. Guo, "Massive hybrid antenna array for millimeter-wave cellular communications," *IEEE Wireless Commun.*, vol. 22, no. 1, pp. 79–87, Feb. 2015.

[56] M. S. Rahman and K. Josiam, "Low complexity RF beam search algorithms for millimeter-wave systems," in *Proc. IEEE Globecom*, Austin, TX, USA, Dec. 2014, pp. 3815–3820.

[57] S. Han, C.-L. I, Z. Xu, and C. Rowell, "Large-scale antenna systems with hybrid analog and digital beamforming for millimeter wave 5G," *IEEE Commun. Mag.*, vol. 53, no. 1, pp. 186–194, Jan. 2015.

[58] D. L. Donoho, "Compressed sensing," *IEEE Trans. Inf. Theory*, vol. 52, no. 4, pp. 1289–1306, Apr. 2006.

[59] W. Bajwa, J. Haupt, A. Sayeed, and R. Nowak, "Compressed channel sensing: A new approach to estimating sparse multipath channels," *Proc. IEEE*, vol. 98, no. 6, pp. 1058–1076, Jun. 2010.

[60] A. Maltsev, A. Sadri, A. Pudeyev, and I. Bolotin, "Highly directional steerable antennas: High-gain antennas supporting user mobility or beam switching for reconfigurable backhauling," *IEEE Veh. Tech. Mag.*, vol. 11, no. 1, pp. 32–39, Feb. 2016.

[61] C. Lin and G. Y. Li, "Energy-efficient design of indoor mmwave and sub-THz systems with antenna arrays," *IEEE Trans. Wireless Commun.*, vol. 15, no. 7, pp. 4660–4672, Jul. 2016.

[62] ——, "Antenna subarray partitioning with interference cancellation for multi-user indoor Terahertz communications," in *Proc. IEEE Globecom*, San Diego, CA, USA, Dec. 2015, pp. 1–6.

[63] ——, "Subarray-based coordinated beamforming training for mmWave and sub-THz communications," submitted to *IEEE J. Sel. Areas Commun.*, Nov. 2016.

[64] ——, "Coordinated beamforming training for mmwave and sub-THz systems with antenna subarrays," in *Proc. IEEE WCNC*, San Francisco, CA, USA, Mar. 2017.

[65] ——, "Indoor Terahertz communications: How many antenna arrays are needed?" *IEEE Trans. Wireless Commun.*, vol. 14, no. 6, pp. 3097–3107, Jun. 2015.

[66] ——, "Indoor Terahertz communications with antenna subarrays," in *Proc. IEEE Globecom*, Austin, TX, USA, Dec. 2014, pp. 3790–3795.

[67] ——, "Adaptive beamforming with resource allocation for distance-aware multi-user indoor Terahertz communications," *IEEE Trans. Commun.*, vol. 63, no. 8, pp. 2985–2995, Aug. 2015.

[68] ——, "Distance-aware multi-carrier indoor Terahertz communications with antenna array selection," in *Proc. IEEE PIMRC*, Washington, DC, USA, Sep. 2014, pp. 595–599.

[69] A. Sayeed, "Deconstructing multiantenna fading channels," *IEEE Trans. Signal Process.*, vol. 50, no. 10, pp. 2563–2579, Oct. 2002.

[70] R. Piesiewicz, C. Jansen, D. Mittleman, T. Kleine-Ostmann, M. Koch, and T. Kürner, "Scattering analysis for the modeling of THz communication systems," *IEEE Trans. Antennas and Propag.*, vol. 55, no. 11, pp. 3002–3009, Nov. 2007.

[71] S. Priebe, M. Jacob, and T. Kürner, "AoA, AoD and ToA characteristics of scattered multipath clusters for THz indoor channel modeling," in *Proc. Eur. Conf. Antennas Propag.*, Rome, Italy, Apr. 2011, pp. 188–196.

[72] H. L. V. Trees, *Optimum Array Processing: Part IV of Detection, Estimation, and Modulation Theory*. New York, NY, USA: Wiley, 2002.

[73] R. L. Haupt, *Antenna Arrays: A Computational Approach*. New York, NY, USA: Wiley, 2010.

[74] C. A. Balanis, *Antenna Theory: Analysis and Design*. New York, NY, USA: Wiley, 2005.

[75] L. A. Belov, S. M. Smolskiy, and V. N. Kochemasov, *Handbook of RF, Microwave, and Millimeter-Wave Components*. Norwood, MA, USA: Artech House, 2012.

[76] S. C. Cripps, *RF Power Amplifiers for Wireless Communications*. Norwood, MA, USA: Artech House, 2006.

[77] J. Joung, C. K. Ho, and S. Sun, "Spectral efficiency and energy efficiency of OFDM systems: Impact of power amplifiers and countermeasures," *IEEE J. Sel. Areas Commun.*, vol. 32, no. 2, pp. 208–220, Feb. 2014.

[78] E. Kaymaksut, D. Zhao, and P. Reynaert, "Transformer-based Doherty power amplifiers for mm-Wave applications in 40-nm CMOS," *IEEE Trans. Microw. Theory Tech.*, vol. 63, no. 4, pp. 1186–1192, Apr. 2015.

[79] S. Horst, R. Bairavasubramanian, M. M. Tentzeris, and J. Papapolymerou, "Modified Wilkinson power dividers for millimeter-wave integrated circuits," *IEEE Trans. Microw. Theory Tech.*, vol. 55, no. 11, pp. 2439–2446, Nov. 2007.

[80] D. M. Pozar, *Microwave Engineering*. New York, NY, USA: Wiley, 2009.

[81] G. Y. Li, Z. Xu, C. Xiong, C. Yang, S. Zhang, Y. Chen, and S. Xu, "Energy-efficient wireless communications: Tutorial, survey, and open issues," *IEEE Wireless Commun.*, vol. 18, no. 6, pp. 28–35, Dec. 2011.

[82] D. Feng, C. Jiang, G. Lim, J. L. J. Cimini, G. Feng, and G. Y. Li, "A survey of energy efficient wireless communications," *IEEE Commun. Surv. Tutor.*, vol. 15, no. 1, pp. 167–178, First Quarter 2013.

[83] N. Deferm and P. Reynaert, *CMOS Front Ends for Millimeter Wave Wireless Communication Systems*. New York, NY, USA: Springer, 2015.

[84] K. Okada and *et al*, "Full four-channel 6.3-Gb/s 60-GHz CMOS transceiver with low-power analog and digital baseband circuitry," *IEEE J. Solid-St. Circuits*, vol. 48, no. 1, pp. 46–64, Jan. 2013.

[85] W. Shin, B.-H. Ku, O. Inac, Y.-C. Ou, and G. M. Rebeiz, "A 108-114 GHz 4×4 wafer-scale phased array transmitter with high-efficiency on-chip antennas," *IEEE J. Solid-St. Circuits*, vol. 48, no. 9, pp. 2041–2055, May 2013.

[86] Q. H. Spencer, A. L. Swindlehurst, and M. Haardt, "Zero-forcing methods for downlink spatial multiplexing in multiuser MIMO channels," *IEEE Trans. Signal Process.*, vol. 52, no. 2, pp. 461–471, Feb. 2004.

[87] Z. Xiao, T. He, P. Xia, and X.-G. Xia, "Hierarchical codebook design for beamforming training in millimeter-wave communications," *IEEE Trans. Wireless Commun.*, vol. 15, no. 5, pp. 3380–3392, May 2016.

[88] S. J. Orfanidis, *Electromagnetic Waves and Antennas*. Piscataway, NJ, USA: Rutgers Univ. Press, 2008.

[89] A. Saleh and R. Valenzuela, "A statistical model for indoor multipath propagation," *IEEE J. Sel. Areas Commun.*, vol. 5, no. 2, pp. 128–137, May 1987.

[90] Q. Spencer, B. Jeffs, M. Jensen, and A. Swindlehurst, "Modeling the statistical time and angle of arrival characteristics of an indoor multipath channel," *IEEE J. Sel. Areas Commun.*, vol. 18, no. 3, pp. 347–360, Mar. 2000.

[91] R. Piesiewicz, T. Kleine-Ostmann, N. Krumbholz, D. Mittleman, M. Koch, and T. Kürner, "Terahertz characterisation of building materials," *IET Electron. Lett.*, vol. 41, no. 18, pp. 1002–1004, Sep. 2005.

[92] M. Vu, "MISO capacity with per-antenna power constraint," *IEEE Trans. Commun.*, vol. 59, no. 5, pp. 1268–1274, May 2011.

[93] C. Han and I. F. Akyildiz, "Distance-aware multi-carrier (DAMC) modulation in Terahertz band communication," in *Proc. IEEE ICC*, Sydney, NSW, Australia, Jun. 2014, pp. 5461–5467.

[94] H. Shams, M. J. Fice, K. Balakier, C. C. Renaud, F. V. Dijk, and A. J. Seeds, "Photonic generation for multichannel THz wireless communication," *Opt. Exp.*, vol. 22, no. 19, pp. 23 465–23 472, Sep. 2014.

[95] J. Yu, X. Li, and N. Chi, "Faster than fiber: Over 100-Gb/s signal delivery in fiber wireless integration system," *Opt. Exp.*, vol. 21, no. 19, pp. 22 885–22 904, Sep. 2013.

[96] A. J. Seeds, H. Shams, M. J. Fice, and C. C. Renaud, "Terahertz photonics for wireless communications," *J. Lightwave Tech.*, vol. 33, no. 3, pp. 579–587, Feb. 2015.

[97] T. Nagatsuma, G. Ducournau, and C. C. Renaud, "Advances in Terahertz communications accelerated by photonics," *Nat. Photonics*, vol. 10, pp. 371–379, May 2016.

[98] A. Adhikary, J. Nam, J.-Y. Ahn, and G. Caire, "Joint spatial division and multiplexing: The large-scale array regime," *IEEE Trans. Inf. Theory*, vol. 59, no. 10, pp. 6441–6463, Oct. 2013.

[99] R. Chen, J. G. Andrews, and J. R. W. Heath, "Efficient transmit antenna selection for multiuer MIMO systems with block diagonalization," in *Proc. IEEE Globecom*, Washington, DC, USA, Nov. 2007, pp. 3499–3503.

[100] S. Boyd and L. Vandenberghe, *Convex Optimization*. Cambridge, U.K.: Cambridge Univ. Press, 2004.

[101] M. Gharavi-Alkhansari and A. Gershman, "Fast antenna subset selection in mimo systems," *IEEE Trans. Signal Process.*, vol. 52, no. 2, pp. 339–347, Feb. 2004.

[102] H. W. Khun, "The Hungarian method for the assignment problems," *Naval Research Logistics Quarterly*, vol. 2, no. 1, pp. 83–97, Mar. 1955.

[103] J. Brady, N. Behdad, and A. Sayeed, "Beamspace MIMO for millimeter-wave communications: System architecture, modeling, analysis, and measurements," *IEEE Trans. Antennas Propag.*, vol. 61, no. 7, pp. 3814–3827, Jul. 2013.

[104] M. L. Jakobsen, T. Pedersen, and B. H. Fleury, "Analysis of the stochastic channel model by Saleh & Valenzuela via the theory of point processes," in *Proc. Int. Zurich Seminar on Commun.*, Zurich, Switzerland, Feb. 2012, pp. 218–225.